Miter Bend Loss and Higher Order Mode Content Measurements in Overmoded Millimeter-Wave Transmission Lines

by

Elizabeth J. Kowalski

B.S. Electrical Engineering, Pennsylvania State University (2008)

Submitted to the
Department of Electrical Engineering and Computer Science
in partial fulfillment of the requirements for the degree of

Master of Science

at the

MASSACHUSETTS INSTITUTE OF TECHNOLOGY

September 2010

Author ....
Department of Electrical Engineering and Computer Science
August 4, 2010

Certified by ....
Richard J. Temkin
Senior Research Scientist, Department of Physics
Thesis Supervisor

Accepted by ....
Professor Terry P. Orlando
Chairman, Committee on Graduate Students
Department of Electrical Engineering and Computer Science

Miter Bend Loss and Higher Order Mode Content Measurements in Overmoded Millimeter-Wave Transmission Lines

by

Elizabeth J. Kowalski

Submitted to the Department of Electrical Engineering and Computer Science
on August 4, 2010, in partial fulfillment of the
requirements for the degree of
Master of Science

Abstract

High power applications require an accurate calculation of the losses on overmoded corrugated cylindrical transmission lines. Previous assessments of power loss on these lines have not considered beam polarization or higher order mode effects. This thesis will develop a theory of transmission that includes the effect of linearly polarized higher order modes on power loss in overmoded corrugated transmission line systems.

This thesis derives the linearly polarized basis set of modes for corrugated cylindrical waveguides. These modes are used to quantify the loss in in overmoded transmission line components, such as a gap in waveguide or a 90° miter bend. The dependence of the loss in the fundamental mode on the phase of higher order modes (HOMs) was investigated. In addition, the propagation of a multi-mode beam after the waveguide was quantified, and it was shown that if two modes with azimuthal (m) indices that differ by one propagate in the waveguide, the resultant centroid and the tilt angle of radiation at the guide end are related through a constant of the motion. These theoretical calculations are useful for high-power applications, such as the electron cyclotron heating in plasma fusion reactors.

In addition, this thesis develops a low-power S-Parameter Response (SPR) technique to accurately measure the loss in ultra-low loss overmoded waveguide components. This technique is used to measure the loss of components manufactured to ITER (an experimental fusion reactor) specifications, operated at 170 GHz with a diameter of 63.5 mm and quarter-wavelength corrugations. The loss in a miter bend was found to be 0.022±0.08 dB. This measurement is in good agreement with theory, which predicts 0.027 dB loss per miter bend, and past measurements [18]. The SPR was used to measure the loss in a gap of waveguide and the results were in good agreement with the well-established theoretical loss due to gap, which demonstrates the accuracy of the SPR technique. For both of these measurements, a baseline analysis determined the effects of a small percentage (1–2%) of higher order modes in the system.

Thesis Supervisor: Richard J. Temkin
Title: Senior Research Scientist, Department of Physics

Acknowledgments

I must thank everyone who had a part in helping this research and with the completion of my thesis. All of the members of the Waves and Beams group helped me with this research. My advisor, Dr. Richard Temkin mentored and guided me through the bulk of the project. Michael Shapiro was a large help in the theoretical derivations presented here. Emilio Nanni and Brian Munroe were instrumental in developing the experimental techniques and in helping me acquire large amounts of experimental data. Emilio is also responsible for introducing me to Pozar and is a wonderful person to share an office with. David Tax implemented the experiments which began this research and passed along the project to me. In addition, Antonio Torrezan, Roark Marsh, Alan Cook and Ivan Mastovsky offered invaluable expertise. While, Hae Jin Kim and Paul Thomas have helped me to begin a new project. I must also thank Tim Bigelow from ORNL, his visit and the resulting discussion of miter bend loss in July 2009 jump-started the experiments discussed in this thesis.

My friends and family offered endless encouragement and motivation. I can only hope to one day return the favor to them.

Elizabeth Kowalski
Cambridge, MA
August 4, 2010

to my mother,

Joan Kowalski.

Next year will be easier. Really.

Contents

List of Figures

List of Tables

Chapter 1

Introduction

Transmission lines are used to transport power in electromagnetic waves from one point to another. Though this may seem a simple task, high power experiments require particular considerations for the attenuation characteristics of their transmission lines to preserve the integrity of the system. Simple smooth wall cylindrical waveguides are useful for low-power experiments, but, when considering the transmission of power on the order of megawatts for meter-length distances, traditional methods will be insufficient due to large attenuation, mode conversion, the possibility of electromagnetic breakdowns, and high heating which can lead to failures in the transmission system. Overmoded metallic circumferentially corrugated cylindrical waveguides have been shown to have low attenuation over long distances, but may result in high amounts of mode conversion and large losses due to misalignment or manufacturing errors. Decreasing the attenuation and mode conversion in high power experiments is necessary for the integrity of the transmission system as well as the success of the experiment, particularly when transmission over long distances is necessary.

1.1 Motivation

Recently, continuous high-power sources have been developed for high frequencies. Specifically, developments in gyrotons have made the devices capable of producing power in the range of megawatts for frequencies up to 170 GHz. For use in experiments such as plasma heating, this radiation must often be transported long distances, many tens of meters. To satisfy experiment requirements and transport the power safely, oversized corrugated metallic waveguides are used for the transmission line system. In addition to plasma heating, oversized corrugated waveguides are useful for plasma diagnostics, radar, materials heating, and spectroscopy.

High power, high frequency experiments offer a unique problem for transmission lines. In contrast, low power, high frequency experiments may be satisfied with small fundamental single-mode waveguides because there is no possibility of breakdown and losses, though high, result in low ohmic heating on the line. Also high power, low frequency experiments can also be satisfied with fundamental mode waveguides because the size of the waveguide increases inversely with frequency, allowing for larger losses without a failure of the system. However, with the combination of high power and high frequency, fundamental waveguides are simply too small to handle the power at hand and are not adequate for experimental uses due to significant power losses leading to failure in the transmission line system and dangerous operation conditions prone to breakdown and damaged equipment. To operate in high power conditions, overmoded waveguides are used for their low attenuation characteristics. For oversized smooth-wall circular waveguide, the lowest loss mode is TE_{01}, which is not the fundamental mode. This property leads to the danger of mode conversion to lower order modes that are hard to filter out. Also, the TE_{01} mode is degenerate with the TM_{11} mode, increasing the possibility of mode conversion to an undesirable mode. On the other hand, corrugated cylindrical waveguides have the lowest loss in the fundamental HE_{11} mode, reducing the concerns for mode conversion to degenerate and lower order modes. In addition, corrugated cylindrical walls with a quarter-wavelength depth of circumferential corrugations offer less attenuation than smooth-wall waveguides due to the boundary conditions imposed by the corrugations. The geometry of corrugated cylindrical waveguides are shown in Figure 1-1, for reference. In general, the inner notches, defined by d, w_1, and w_2, are on the order of λ. To avoid Bragg reflector characteristics the periodicity, w_1, is approximately $\lambda/3$. The

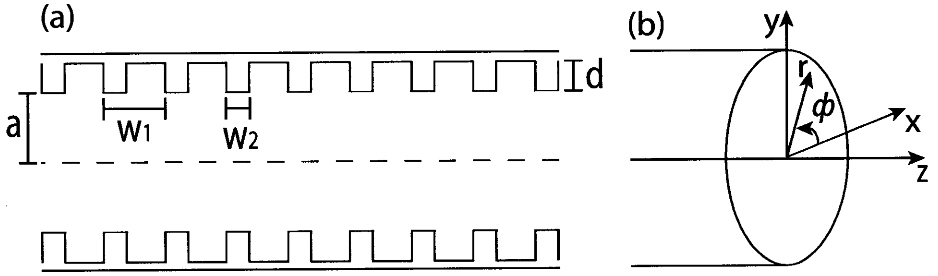

Figure 1-1: (a) A cylindrical circumferentially corrugated waveguide with a radius of a. The corrugations are defined by w_1, w_2, and d. For low loss characteristics the corrugation depth is $d = \lambda/4$. (b) An illustration of the variables in the cylindrical geometry.

radius, a, is much greater than λ for an overmoded waveguide.

Due to the high power experiments that they will be used for, the losses in overmoded corrugated waveguides must be sufficiently calculated and experimentally analyzed. First introduced in 1970 for communication applications, overmoded corrugated cylindrical waveguides for high power, high frequency experiments offer low losses in the fundamental and lower order modes that propagate in the waveguide. Analytical and experimental calculations have estimated the straight-length attenuation in corrugated waveguides to be smaller than equivalent smooth wall waveguides and, even, negligibly small for most applications if the waveguide corrugations are properly configured for the desired transmission frequency. In analyzing the loss associated with corrugated waveguides, it is useful to interpret the modes present in a waveguide and the field patterns which result. In addition, certain waveguide components and configurations offer more insight into the losses that will result in practical transmission line systems. Particularly the loss associated with 90° miter bends and gaps in the waveguide will be used in this thesis to quantify the loss characteristics of overmoded corrugated circular transmission lines.

1.2 Review of Corrugated Cylindrical Waveguides

This review of the literature will discuss the development of corrugated cylindrical waveguides and their attenuation characteristics. The literature is split into three sections which discuss the characteristics of overmoded corrugated cylindrical waveguides: the initial development and straight-length attenuation analysis, the development of modes and their field patterns in waveguides, and the theoretical calculations and experimental measurements of loss in 90° miter bends.

1.2.1 Straight Waveguide Attenuation

Overmoded corrugated waveguides were first introduced for millimeter wave transmission because of their low attenuation for the fundamental mode. This attenuation was seen to be lower than the smooth-wall fundamental modes [8]. Clarricoats patented the design [2] and experimentally measure the loss in straight sections of corrugated waveguide [4], [28]. Later designs specified overmoded transmission lines as being necessary for high power transmission due to wall heating and smaller attenuation parameters and further refined the waveguide design parameters for low attenuation.

In a discussion on flared corrugated feeds for antennas, [8] reported that the attenuation in corrugated circular transmission lines was theoretically smaller than the fundamental mode in smooth-wall transmission lines. Previously, fundamental mode propagation in smooth wall transmission lines had been the standard for low attenuation. This small transmission in corrugated waveguides was due to the wall effects in hybrid modes and was significantly less than the lowest loss smooth-wall waveguides modes. This is likely due to the fact that the HE_{11} mode, the fundamental mode for corrugated waveguides, has power concentrated in the center and small fields at the walls of the waveguide, whereas TE_{01} and TM_{11}, the lowest loss modes for smooth wall waveguides, have power that is off-center and more susceptible to losses due to fields present at the walls. For $d = \lambda/4$ (see Figure 1-1), the wall requires balanced hybrid modes and the azimuthal magnetic fields vanish at the walls. These conditions result in about 0.0004–0.001 dB/m theoretical attenuation in the 10–20 GHz range for waveguides operating in the fundamental mode with $d \approx \lambda$.

Expanding on the results from [8], [4] reports 30% lower attenuation in the fundamental HE_{11} mode for corrugated waveguides than TE_{01} and TM_{11} modes for smooth wall waveguides. These results were shown for 20–80 mm diameter waveguides for

4–20 GHz waves. In addition, overmoded, or oversized, corrugated cylindrical waveguides (i.e. waveguides with the ability to propagate at least three modes) were shown to have less attenuation per meter than overmoded smooth wall circular, single-mode smooth wall circular, and single mode rectangular waveguides. This result indicates that overmoded corrugated waveguides are significantly better for high power applications than any alternative methods available. The design for low attenuation corrugated waveguides was also patented by Clarricoats with similar losses reported [2].

Experimental validation of [4] was offered by [28]. Over a range from 8–11 GHz, the HE_{11} mode in a corrugated waveguide is shown to have about 4–5 dB/km attenuation, with good agreement between experimental and theoretical results. Similar fundamental smooth-wall waveguide modes have attenuation from 4–14 dB/km with single-mode propagation. However direct comparison between these two waveguides is unfavorable to the corrugated waveguide because it is overmoded. Overmoded smooth wall waveguides perform worse than their corrugated counterparts, indicating another significant advantage of the overmoded corrugated waveguide design.

A more complete discussion of the modes and attenuation in corrugated waveguides is discussed in theory and with experimental conclusions in [6] and [7]. The modes are described as being standing waves in the corrugations which impose boundary conditions on the modes propagating in the waveguide. Theoretically derived and experimentally shown, the depth of the waveguide is specified to be $d = \lambda/4$ for low attenuation values because this depth results in zero field conditions on the propagating HE_{11} mode at the boundary. Since most loss occurs at the walls, small fields at the wall are theorized and experimentally shown to lead to smaller attenuations. In addition, the attenuation is shown experimentally to be insensitive to small changes in the widths of corrugations, so long as the corrugations occur periodically at values close to λ.

To compare attenuation characteristics, [15] discusses the characteristics of the HE_{11} mode in different types of waveguide. He discusses two points for characterizing the HE_{11} mode: that the field is polarized in one direction and that the electric and magnetic field at the boundary is essentially zero. For corrugated waveguides, the corrugations act in the same way as a dielectric surface, imposing a boundary condition on the propagating HE_{11} mode. Again, in the case of quarter-wavelength corrugations, the wall effects cause the HE_{11} mode to reduce to zero at the corrugation wall. Approximate field expressions for the HE_{11} mode in a corrugated waveguide (as well as other waveguides) are derived, taking into account the wall effects due to corrugations (or other waveguide characteristics).

The propagation and mode coupling in corrugated waveguides is discussed completely by [11], which is often cited as the definitive source for corrugated waveguides. This article states that overmoded waveguides are used to reduce loss and prevent breakdown in high power applications. It formulates the hybrid, HE and EH, modes for corrugated guides, and discusses the low attenuation found in the HE_{11} mode, as well as other HE_{mn}, EH_{mn}, TE_{0n} and TM_{0n} modes in corrugated waveguides. An expression for the coupling coefficients between modes is also analytically expressed, this relates how the modes are generated and their relations. This chapter by Doane, [11], has become a common reference for the theory behind corrugated waveguide modes and their attenuation parameters due to its completeness.

To validate analytical analysis, [1] discusses experimental loss measurements of corrugated waveguides. A waveguide system consisting of 30 m of 63.5 mm diameter (31.75 mm radius) corrugated waveguide and 7 miter bends was installed on an electron cyclotron emission measurement system. The system operated with multimode transmission and frequencies from 75–575 GHz. Negligible Ohmic loss was recorded for single and multimode transmission at 140 and 250 GHz, respectively. However, large losses were seen to occur due to mode conversion in completely overmoded waveguide systems, this conversion was mostly due to miter bends in the system.

In a discussion on high power microwave components, [34] emphasizes the importance of overmoded corrugated waveguides and miter bends to high power, high frequency systems. Once again, the propagation of the HE_{11} mode is discussed and approximations are made to derive an expression for the attenuation in straight sections of waveguide. In particular, approximations are made to define the HE_{11} mode as

$$E_y = E_0 J_0(X_{01} r/a) \tag{1.1}$$

$$E_x \approx 0 \tag{1.2}$$

$$E_z \approx 0, \tag{1.3}$$

where J_0 is the zeroth order Bessel function of the first kind and X_{01} is the first root of the zeroth Bessel Function. The details apparent in this expression for electric field have already been discussed in previous works, however the simple approximation of the field pattern is useful for a quick analysis of the HE_{11} mode. Quasi-optical miter bends are also discussed quickly as having a low-attenuation 90° miter bend, these will be discussed later. In addition, the loss due to gaps in a waveguide is discussed with an approximate analytical expression given for the power loss.

1.2.2 Modes in Corrugated Cylindrical Waveguide

An important secondary aspect of overmoded waveguides, in general, is the description of the modes that are contained within the waveguide. These modes help to define the attenuation. Previously, it was thought that all modes functioned independently of each other [24]. However, it has since been understood that the beating between modes causes fluctuations in attenuation, particularly in quasi-optical transmission line components like miter bends and polarizers. In the previous section, only loss in the fundamental HE_{11} mode was discussed, but overmoded waveguides inherently propagate higher order modes, which can amount to a large source of attenuation for the fundamental mode, and, therefore, a large loss of power when calculating the transmission efficiency of a corrugated circular overmoded waveguide.

The propagation and radiation characteristics of cylindrical corrugated waveguides was first developed in [5]. This book chapter defines the HE_{1n} modes with all of the corresponding field patterns for corrugated guides and the cut off frequencies of the modes. It also reinforces the low-attenuation calculations for straight waveguide propagation, expanding the argument for higher order modes. Though this is similar

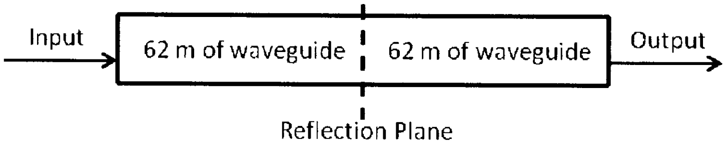

Figure 1-2: The experimental approach for [26] to measure the loss in 124 m of straight overmoded corrugated waveguide.

to the previous work describing attenuation in circular corrugated waveguides, the definition of higher order mode field patterns and attenuation characteristics expands the theoretical understanding of overmoded waveguides.

The field patterns of hybrid modes, HE_{mn}, and wall functions of corrugated cylindrical waveguides are fully defined in [9]. The formulation of the hybrid modes will be discussed further in Chapter 2. Only slight approximations are taken, and the model of the corrugations in the waveguide acting as a dielectric which imposes boundary conditions, i.e. wall functions on the propagating modes are enforced. The HE modes for several types of waveguides are discussed, and the similarities in analysis indicate that corrugations result in low losses partly because of the fields approaching zero at the wall boundaries.

Experimental measurements for loss and higher order mode content were performed in [26], which measured the loss due to 62 m of straight overmoded corrugated waveguide. The waveguide was 8.89 cm in diameter and was operated at 140 GHz. Since a reflectometry method was used, they attempted to experimentally measure the loss in a transmission length of 124 m (twice the actual distance), see Figure 1-2. Unfortunately, the loss was too small for measurements and was inferred to be less than 2 dB/km and negligible. Interestingly, the beating between HE_{11} and HE_{21} modes was also observed during measurements, which causes a group velocity delay that sinusoidally varies with transmission distance. This indicates that the modes do not propagate completely independent of each other. Two modes interact when propagating in the same transmission line, and, moreover, there is a dependence between their interaction characteristics and the phase between the modes.

Precise definitions of all modes in a waveguide, with corresponding field patterns appear in [25]. Numerical calculations of the coupling of a tilted Gaussian beam into a waveguide are primarily discussed and indicate the losses due to insertion of a beam into the waveguide. This analysis provides an analytical formula for the power loss due to coupling with an angle. As an example, a waveguide with a diameter of 8.89 cm operating at 168 GHz is shown to need an input with less than 0.1° tilt and 2.9 mm offset to have less than 1% mode conversion. This application indicates the precision necessary when operating in the fundamental mode of overmoded waveguides

In order to generate the HE_{11} mode in a waveguide, Gaussian beams are used as input. [29] discusses the coupling of Gaussian beams produced by a gyrotron into corrugated waveguides operating at 110 GHz. The power that couples into the HE_{11} mode is dependent on the parameters of the Gaussian beam: ellipticity, offset from the center of the guide, distance from the radiation point of the Gaussian beam, angle of beam propagation. Ideally, the beam is circular with no tilt or offset. In addition, there is a certain beam radius, w_0, which leads to an optimum coupling to the HE_{11} mode which is about $w_0 = 0.64a$, where a is the radius of the waveguide, and leads to 97% coupling into the HE_{11} mode for a perfect gaussian beam.

1.2.3 Miter Bends

A common waveguide component in overmoded systems is a miter bend. A miter bend is a quasi-optical passive component in waveguide which is used to change the propagation direction of the wave by 90°. For overmoded corrugated cylindrical waveguide an optical mirror is placed at 45° to the direction of propagation. These components are necessary when practical experiments are considered where high frequency waves must be transferred from one place to another, typically over a distance of tens of meters, and certain obstacles must be avoided during the propagation. Though the loss in these components has been experimentally and theoretically recorded to be low, less than 0.1 dB (depending on signal and waveguide parameters), the loss is relatively high when compared to other losses on the transmission line and the high power nature of the systems under test. For this reason, it is necessary to accurately quantify the losses in a miter bend.

A simplified theoretical calculation to quantify the loss in a miter bend is presented by [23]. The loss in the waveguide may be estimated as a set of two-dimensional problems, by taking advantage of the quasi-optical mirror and electromagnetic boundary conditions. This decomposition process will be described in more detail in Chapter 3. The theoretical loss calculated through technique corresponded well to experiments with $\lambda/a = 0.5$ (considered large at the time).

Marcatili's theory for calculating the loss in a miter bend in smooth wall waveguide [23] was expanded for a corrugated waveguide propagating the HE_{11} mode in [13]. In this case, the miter bend is approximated as a gap in the waveguide. To account for the approximation, the loss due to a miter bend is estimated as half of the loss due to a gap in the waveguide where the gap length is equivalent to the diameter of the waveguide; again, this theory will be discussed in more detail in Chapter 3. The loss due to a miter bend for the HE_{11} mode in a corrugated waveguide is found to be approximately $1.7(\lambda/a)^3/2$, where λ is the wavelength and a is the radius of the guide. The theory was compared with good agreement to experimental measurements of mode mixtures propagating across a gap at 110 GHz in 1.25 inch radius waveguide. In this case, the theoretical loss for the HE_{11} mode was found to be 0.06 dB per miter bend.

Expanding on the gap theory discussed in [13], [35] calculates the transmission losses in overmoded waveguide gaps due to TE, TM, HE, and EH modes through the use of a scattering matrix code. Experimentally, the losses due to a gap in smooth-wall waveguide of radius 1.39 cm at 28 GHz were measured. These measurements were in good agreement with the scattering matrix code and analytical calculations.

In addition, [32] calculates and experimentally measures the losses due to a gap, and maintains that a gap is an approximation of a 90° miter bend. Due to mode combinations, it was recognized that the loss in the gap for HE_{11} can be minimized by the appropriate addition of higher order modes. This analysis led to the creation of an HE_{11} mode filter which takes advantage of mode conversion due to a gap and was tested at low power for a 31.75 mm diameter corrugated waveguide operating at 84 GHz, and resulted in 99.3% mode purity.

In order to calculate the loss due to a miter bend, [33] models a miter bend as a gap with a small modification which takes into account the fact that the miter bend is not exactly open on top and takes away the approximated 2-dimensional symmetry of the problem while still eliminating the 90° bend from the analysis. A mode propagating through the modified gap can be calculated using fast Fourier transform techniques. This method approximates the loss in a miter bend to be about 0.022 dB for the HE_{11} mode, with a waveguide of 63.5 mm diameter at 170 GHz. In addition, the effects of parasitic higher order modes on the system were considered. With a 2-mode input, the loss in the miter bend is dependent on the relative phase between the two modes. However, the average loss all relative phases is still 0.022 dB per bend for the HE_{11} mode.

Experimentally, the loss of a miter bend designed for the ITER project and built by General Atomics was measured in [18]. Through low power testing of 31.75 mm radius waveguide operating at 170 GHz, the loss was measured with a Vector Network Analyzer operating at rectangular fundamental mode. This measurement requires an up-taper and mode-converter from WR-05 rectangular waveguide to the overmoded corrugated cylindrical waveguide. The technique resulted in a measurement of a miter bend loss of 0.05±0.02 db per bend. This loss is in agreement with theoretical loss calculations, however the large error in the measurement is due the sensitivity of the measurement, the reproducibility of results, and the higher order modes present in the system. These higher order modes develop in the mode-converter/up-taper. The measurements discussed in this thesis, primarily in Chapter 5 use the same equipment as [18], however a measuring and analysis technique, described in Chapter 4, has been employed to obtain a more accurate measurement and to minimize the error in the measurement due to of higher order modes.

1.3 ITER

With a pressing need politically and scientifically for the large production of energy with a small environmental impact, research into fusion energy is extremely beneficial.

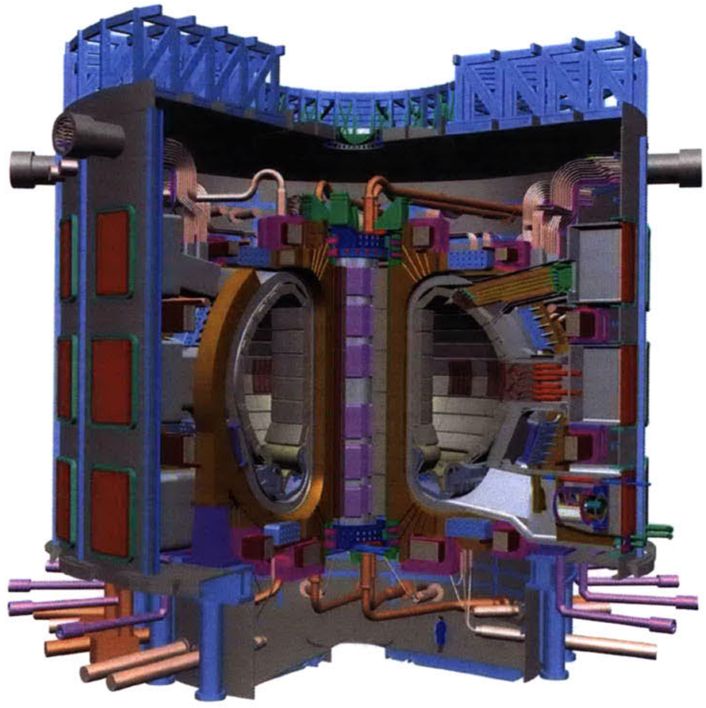

Figure 1-3: A diagram of the proposed ITER fusion reactor.

ITER, Latin for "The Way" and formerly known as the International Thermonuclear Experimental Reactor, is an experimental fusion tokamak that will be a large advancement towards the production of fusion power. A diagram of the tokamak is shown in Figure 1-3. Seven participating countries have agreed to work on this project that will be a large advancement in proving the viability of nuclear fusion energy as a profitable power plant. With first plasma scheduled for 2016, ITER's success would provide the basis for an alternate means of energy in a future beyond the scope of our current energy resources.

In addition to supportive research and collaboration, the United States ITER Project will be delivering the transmission line system for the international ITER team. This system must transport 20 MW of power at 170 GHz to the ignition plasma from the twenty-four 1 MW Gyrotrons that will power the experiment, as depicted in Figure 1-4. The power will be used for electron cyclotron resonance heating (ECRH) and must be in the fundamental HE_{11} mode for proper use and precision accuracy in launching the wave into the plasma. In ECRH, a high frequency electromagnetic

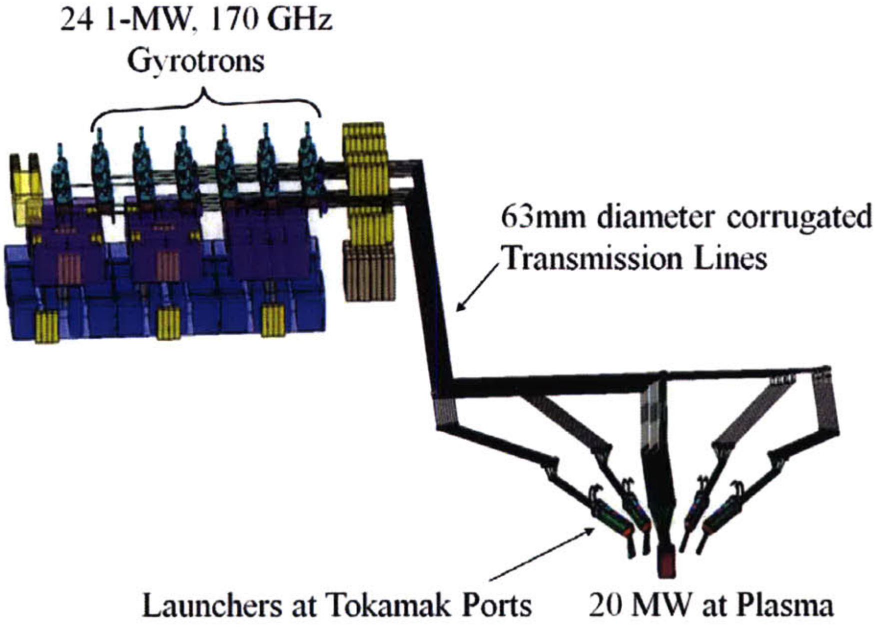

Figure 1-4: A schematic of the ITER electron cyclotron resonance heating (ECRH) system.

wave is injected into the plasma. The frequency of the wave is matched to the electron cyclotron resonance frequency,

$$f_{ce} = \frac{\omega_{ce}}{2\pi} = \frac{eB}{2\pi m_e} \approx 28[GHz/T]B[T] \tag{1.4}$$

Since ITER operates at a magnetic field of 6 Teslas in the center of the plasma, f_{ce} is 170 GHz.

A more specific schematic of the transmission line system between the Gyrotrons and equatorial launcher into the plasma is shown in Figure 1-5. The delivery specification requires at least an 84% efficiency in transmission. Such a strict efficiency for this amount of power necessitates high quality transmission components that will meet these specifications and a complete theoretical and experimental analysis of the loss in all of the components.

To transmit high frequency microwaves over long distances with small power loss, overmoded transmission lines will be used. The transmission line components consist of 63.5 mm diameter circular corrugated waveguide and operate in the fundamental

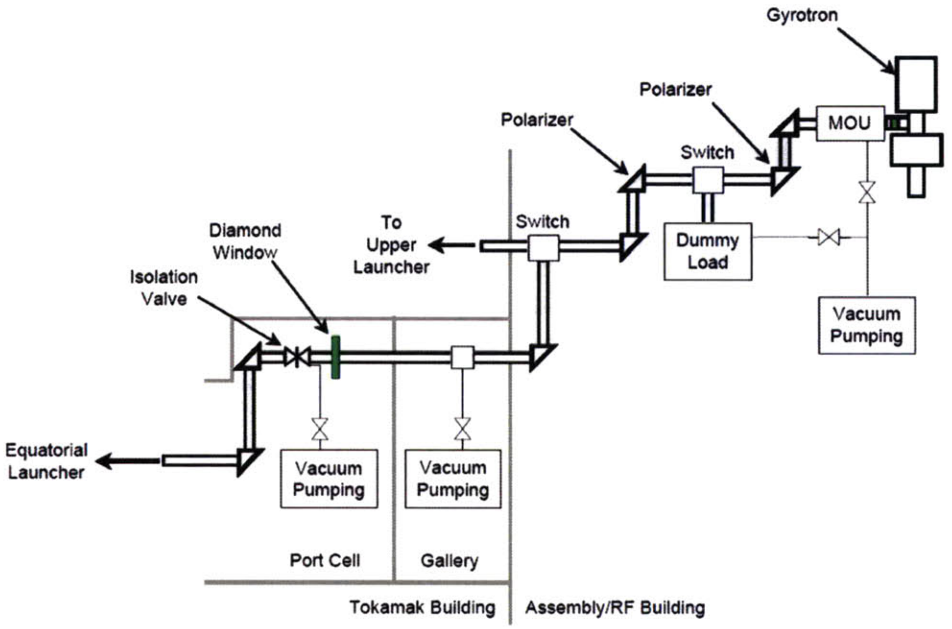

Figure 1-5: A detailed schematic of the ITER transmission line system which will be used for ECRH. The equatorial launcher directs the 170 GHz electromagnetic wave into the plasma.

HE_{11} mode. The corrugated waveguides will minimize losses in the plasma heating experiment. Table 1.1 shows a rough theoretical breakdown of the losses on the transmission line. According to these preliminary calculations, an 86% efficiency in transmission is possible. However, not all components are considered in these loss measurements, resulting in a need for greater efficiency. In addition, the effects due to mode conversion from the HE_{11} mode on mode launching into the plasma and increased loss in the system are largely ignored.

It's clear from Table 1.1 that a large part of the losses are due to the seven miter bends required to transport the power. Therefore, a more accurate assessment of the loss associated with these components will be particularly useful in quantifying the loss of the entire system. Theory has predicted that the loss due to a miter bend is, on average, 0.027 dB. This estimation accounts for diffraction loss, ohmic loss, and loss due to a 0.05° tilt in the mirror of the miter bend (an estimation of manufacturing inconsistencies). This thesis will focus largely on obtaining a precise experimental measurement of the loss in a miter bend for the ITER transmission system.

Losses	ITER DDD 5.2	MIT Estimate
MOU Loss	0.22 dB	–
Injection	0.035 dB	0.116 dB
Miter Bend	0.248 dB	0.19 dB
Polarizers	0.044 dB	0.066 dB
Waveguide Sag	0.078 dB	0.039 dB
Waveguide Tilt/Offset	–	0.036 dB
Other	0.025 dB	0.043 dB
Total	0.65 dB	0.49 dB
Total without MOU	0.43 dB	0.49 dB

Table 1.1: An estimation of the losses in the ITER Transmission line system. [17]

Gyrotrons will be used to power ITER and generate Gaussian-like output beams intended to propagate as the fundamental HE_{11} mode in transmission lines. Gyrotron beams, being linearly polarized, allow for the use of linearly polarized (LP) modes as a basis set for describing the mode patterns in a transmission line. This correlation has been largely overlooked in the present literature. The use of this notation will provide a convenient and consistent method for analysis.

Established miter bend theory provides a basis for the analysis of loss in a miter bend, however the analysis is incomplete. This theory models the miter bend as a gap in the waveguide of length $L = 2a$, and states that this 2-dimensional geometry calculates twice the loss associated with a miter bend, about 0.5% HE_{11} loss for the specified geometry [13]. Half of the power is lost in the gap and half is lost due to mode conversion. However, parasitic higher order modes (HOMs) can greatly influence the power loss [33]. Considering a practical input into the transmission lines requires analysis of HOMs resultant from the imperfect input into the system. These imperfections amount to several percent of HOMs and arise from the limitations of the gyrotron output, offset and angle of the input into the transmission line, and overall impurities in the system [25].

With the greater impact of ITER in mind, this thesis will focus on the loss associated with transmission lines, with an emphasis on miter bends. Using the LP modes as a basis set, the impact of higher order modes on loss in the transmission lines will be analytically calculated and experimentally considered. The mode content present in the experimental set-up will be measured. These mode considerations will allow the loss in a miter bend to be experimentally measured with a larger accuracy and certainty than previous attempts.

The transmission lines used in all experiments and specific theoretical calculations and examples discussed in this thesis have been chosen and designed to meet ITER specifications. The circular corrugated metallic waveguides have a radius of 31.75 mm are operated at 170 GHz, with corrugation depths of $d = \lambda/4$. The components used in experimentation (Chapter 5) are fabricated to ITER standards and specifications by General Atomics.

1.4 Organization of this thesis

This thesis will theoretically and experimentally discuss the miter bend loss and higher order mode content of corrugated cylindrical waveguides. New theoretical analysis and experimental techniques have been developed to quantify higher order mode effects and results in an accurate measurement of miter bend loss.

Chapter 1 has discussed the motivation for the project, as well as giving a preliminary review of the literature and background information for the ITER project. Chapter 2 reviews the modes present in corrugated cylindrical waveguides, particularly the Linearly Polarized (LP) set of modes. Chapter 3 discusses the analytical and theoretical attenuation in corrugated cylindrical waveguides. This analysis will focus on the loss in a gap of waveguide and the loss due to a miter bend with an emphasis on higher order modes. Chapter 4 describes the low-power experimental measurement technique that we have developed to measure the loss in overmoded waveguide components through S-Parameter analysis. Chapter 5 shows the results from the implementation of this technique for both a gap in a straight section of waveguide and a miter bend. Chapter 6 discusses the theoretical radiation of a wave at the end of a waveguide, useful for applications such as injection system for electron cyclotron heating of plasma. Finally, Chapter 7 discusses the impact of our results, the conclusions from this work, and future work.

Chapter 2

Modes in Cylindrical Waveguides

The modes in a corrugated cylindrical waveguide are inherently complex, but can be simplified by taking reasonable approximations, the traditional basis set of hybrid modes (i.e. TE, TM, HE and EH modes) for corrugated cylindrical waveguide are readily defined in the literature (for example [11], [9], and [25]), but the derivation of the hybrid mode formulation is presented in this chapter for completeness of our argument. However, considering that high power experiments often use a linearly polarized gyrotron as input, it is convenient to discuss and derive a Linearly Polarized (LP) basis set of modes. The LP modes are an established basis set for optical waveguides ([37], [27]). The set has been reformulated here to apply to corrugated cylindrical waveguides. The LP set of modes for corrugated cylindrical waveguide is an orthogonal basis set and will be used throughout the rest of this thesis.

2.1 Modes in a Smooth Waveguide

For completeness, the discussion on modes in a corrugated cylindrical waveguide will start with a derivation of the modes in a smooth cylindrical waveguide, with parameters as shown in Figure 2-1 for the Transverse Electric (TE) and Transverse Magnetic (TM) waves.

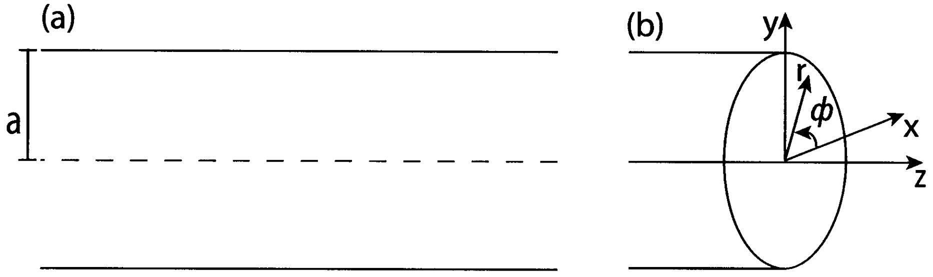

Figure 2-1: (a) The parameters of a smooth-walled cylindrical waveguide with a radius of a. (b) The cylindrical geometry, for reference.

As with all mode derivations, we begin with Maxwell's equations,

$$\nabla \times \vec{E} = \mu \frac{\partial H}{\partial t} \tag{2.1}$$

$$\nabla \times \vec{H} = -\varepsilon \frac{\partial E}{\partial t} + \vec{J} \tag{2.2}$$

$$\nabla \cdot \vec{H} = 0 \tag{2.3}$$

$$\nabla \cdot \vec{E} = \frac{\rho}{\varepsilon}. \tag{2.4}$$

Assuming no sources and solutions of the form $e^{j\omega t}$, the wave equation is derived as

$$\left(\nabla^2 + k^2\right) \left\{ \begin{array}{c} \vec{E} \\ \vec{H} \end{array} \right\} = 0; \tag{2.5}$$

The wavenumber is defined as k, such that $k^2 = w^2 \mu\varepsilon$. For the waveguide considered here, μ and ε are the permeability and permitivity of free space, such that $k^2 = \omega^2/c^2$. In the case of cylindrical waveguides, the wavenumber is also defined as $\vec{k} = k_z\hat{z} + k_\perp\hat{s}$, or $k^2 = k_z^2 + k_\perp^2$, where $\hat{s}$ is perpendicular to the direction of propagation, $\hat{z}$. However, all the modes considered here are non-rotating, such that $k_\phi = 0$ and $k_\perp = k_r$. Therefore, the wavenumber is $\vec{k} = k_z\hat{z} + k_r\hat{r}$ and $k^2 = k_z^2 + k_r^2$ [20].

Due to the geometry of the problem, the waves in the guide will propagate in the positive $\hat{z}$-direction as $e^{-jk_z z}$, so that $\partial/\partial z = -jk_z$. The wave equation for the modes

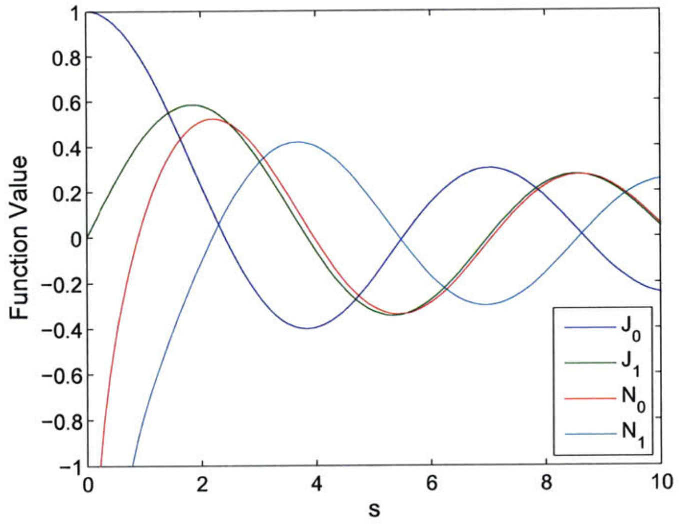

Figure 2-2: The zeroth and first order Bessel and Neumann functions.

in a cylindrical waveguide is

$$\left[\frac{1}{r}\frac{\partial}{\partial r}\left(r\frac{\partial}{\partial r}\right)+\frac{1}{r^2}\frac{\partial^2}{\partial\phi^2}+k_r^2\right]\left\{\begin{array}{c}E_z\\H_z\end{array}\right\}=0 \tag{2.6}$$

At this point, the Bessel function must be discussed. The Bessel Function is defined by the differential equation

$$\left[\frac{1}{s}\frac{\partial}{\partial s}\left(s\frac{\partial}{\partial s}\right)+\left(1-\frac{m^2}{s^2}\right)\right]B_m(s)=0, \tag{2.7}$$

where m is an integer, s is the argument to the function, and B is an mth order Bessel function. This Bessel function derivative has solutions defined by special functions, the Bessel function of the first kind, $J_m(s)$, the Neumann function $N_m(s)$, and the Hankel functions of the first and second kind $H_m^{(1,2)}(s)$. The Hankel function is a combination of the the Bessel function of the first kind and Neumann function in the complex plane. These different functions are discussed in detail in the the literature (e.g. [20]). The different types are defined by how the function deals with respectively large and small values of r. Figure 2-2 depicts the zeroth and first order Bessel and Neumann functions.

The wave equation, (2.6), can be rearranged to fit the form of the Bessel Function differential equation. If E_z and H_z are assumed to have a sinusoidal dependence on ϕ, then $\partial^2/\partial\phi^2 = -m^2$. The wave equation is rewritten as

$$\left[\frac{1}{k_r r}\frac{\partial}{\partial(k_r r)}\left(k_r r\frac{\partial}{\partial(k_r r)}\right) + \left(1 - \frac{m^2}{(k_r r)^2}\right)\right]\left\{\begin{array}{c} E_z \\ H_z \end{array}\right\} = 0. \tag{2.8}$$

By comparison with equation (2.7) for the Bessel function, it's clear that

$$\left\{\begin{array}{c} E_z \\ H_z \end{array}\right\} = B_m(k_r r)\left\{\begin{array}{c} \sin(m\phi) \\ \cos(m\phi) \end{array}\right\} \tag{2.9}$$

where B_m is a generalized mth order Bessel function.

At this point, it is pertinent to discuss which B_m functions are valid solutions for the field equations. In particular, all field components must be finite within the waveguide for a realistic solution. Considering Maxwell's equations, the stipulation for finite fields implies that both the B_m function type and it's derivative must be finite from $r = 0$ to $r = a$ for all values of ϕ. Demonstrated in Figure 2-2, only the Bessel function of the first kind, J_m, fits these conditions.

2.1.1 TM Modes

It is simple to split a wave into the Transverse Magnetic (TM) and Transverse Electric (TE) components. The TM modes of the smooth wall cylindrical metallic waveguide will be discussed first. These modes require that $H_z = 0$, therefore

$$E_z = E_0 J_m(k_r r)\left\{\begin{array}{c} \sin(m\phi) \\ \cos(m\phi) \end{array}\right\} e^{-jk_z z} \tag{2.10}$$

where E_0 in an arbitrary amplitude of the mode. Using Maxwell's equations and the dispersion relation for cylindrical waveguide, it is easy to find the solution for the rest of the fields,

$$E_r = \frac{jk_z k_r E_0}{k^2 - k_z^2} J'_m(k_r r) \left\{ \begin{array}{c} \sin(m\phi) \\ \cos(m\phi) \end{array} \right\} e^{-jk_z z} \tag{2.11}$$

$$E_\phi = \frac{jk_z E_0}{k^2 - k_z^2} \frac{m}{r} J_m(k_r r) \left\{ \begin{array}{c} \cos(m\phi) \\ -\sin(m\phi) \end{array} \right\} e^{-jk_z z} \tag{2.12}$$

$$H_r = \frac{-j\omega\varepsilon E_0}{k^2 - k_z^2} \frac{m}{r} J_m(k_r r) \left\{ \begin{array}{c} \cos(m\phi) \\ -\sin(m\phi) \end{array} \right\} e^{-jk_z z} \tag{2.13}$$

$$H_\phi = \frac{j\omega\varepsilon k_r E_0}{k^2 - k_z^2} J'_m(k_r r) \left\{ \begin{array}{c} \sin(m\phi) \\ \cos(m\phi) \end{array} \right\} e^{-jk_z z}. \tag{2.14}$$

The sinusoidal and cosinusoidal dependence is arbitrary, considering the azimuthal symmetry of a cylindrical waveguide.

The boundary conditions of the smooth wall cylindrical waveguide require the perpendicular components of the electric field and the parallel components of the magnetic field to be zero at the walls of the waveguide. Therefore, at $r = a$, E_z and E_ϕ must be zero. This condition requires that $J_m(k_r a) = 0$, or

$$k_r = \frac{X_{mn}}{a} \tag{2.15}$$

where X_{mn} is the nth root of the mth Bessel function of the first kind, such that $J_m(X_{mn}) = 0$. The dispersion relation can now be written as

$$k_z = \sqrt{\omega^2 \mu\varepsilon - (X_{mn}/a)^2}. \tag{2.16}$$

The cutoff wavenumber for the TM$_{mn}$ mode is $k_{c,mn} = X_{mn}/a$, and the cutoff frequency is $f_{c,mn} = cX_{mn}/2\pi a$.

Thus, the TM$_{mn}$ fields in a waveguide are fully defined by known parameters. The indices indicate variations in the field both radially by m and azimuthally by n. The lowest order TM mode for smooth-walled waveguide is the TM$_{11}$ mode.

Select fields are shown in Figure 2-3. For corrugated cylindrical waveguide, only

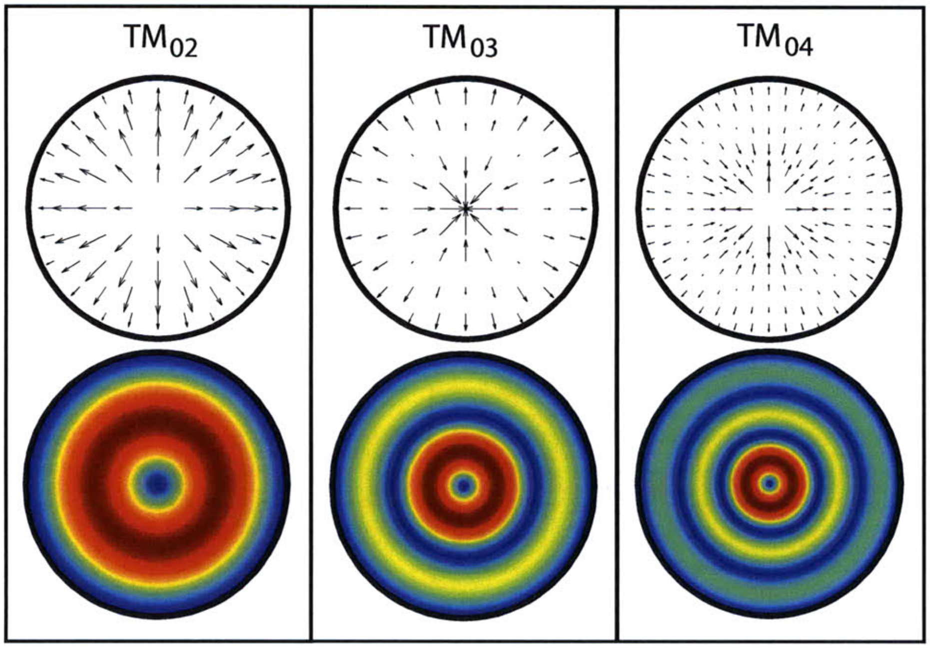

Figure 2-3: The transverse electric field magnitude and vector plots for TM_{0m} modes. These modes also propagate in corrugated waveguide. The black circle indicates the wall of the waveguide.

the $\mathrm{TM}_{0m}(m > 1)$ modes propagate. This is due to the boundary conditions which will be discussed when deriving the hybrid modes. The TM_{01} mode is a surface wave in corrugated waveguide [11].

2.1.2 TE Modes

The same analysis can be performed for Transverse Electric (TE) modes in a smooth wall cylindrical metallic waveguide. These modes require that $E_z = 0$, therefore

$$H_z = J_m(k_r r) \left\{ \begin{array}{c} \sin(m\phi) \\ \cos(m\phi) \end{array} \right\} e^{-jk_z z}. \tag{2.17}$$

Using Maxwell's equations, as in the TM mode case, yields solutions for the transverse fields in the waveguide, such that

$$H_r = \frac{jk_z k_r}{k^2 - k_z^2} J'_m(k_r r) \left\{ \begin{array}{c} \sin(m\phi) \\ \cos(m\phi) \end{array} \right\} e^{-jk_z z} \tag{2.18}$$

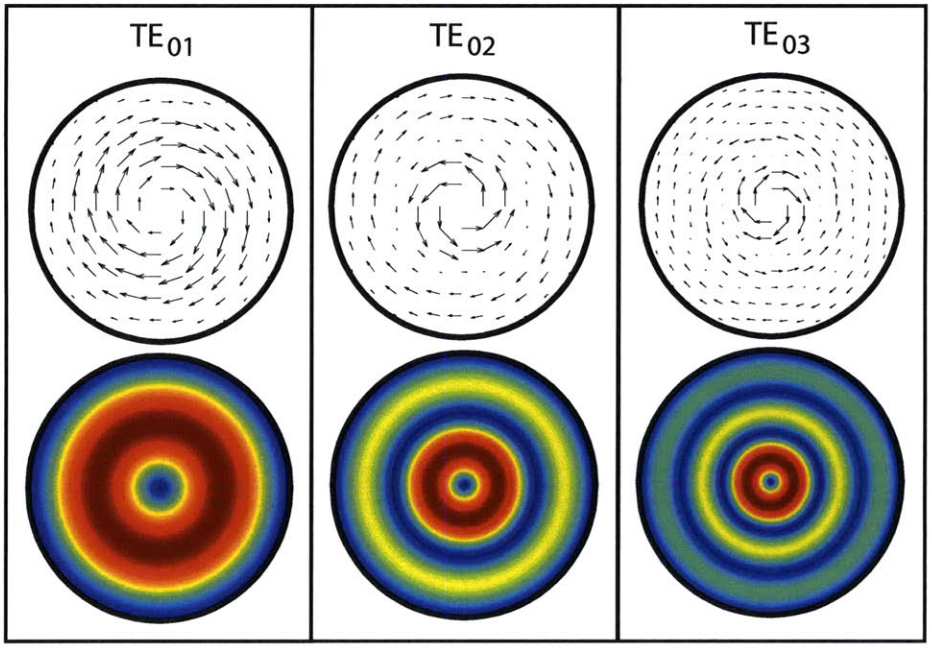

Figure 2-4: The transverse electric field magnitude and vector plots for select TE$_{0m}$ modes which will propagate in a corrugated waveguide. The black circle indicates the waveguide wall.

$$H_\phi = \frac{jk_z}{k^2 - k_z^2}\frac{m}{r}J_m(k_r r)\left\{\begin{array}{c}\cos(m\phi)\\ -\sin(m\phi)\end{array}\right\}e^{-jk_z z} \tag{2.19}$$

$$E_r = \frac{j\omega\mu}{k^2 - k_z^2}\frac{m}{r}J_m(k_r r)\left\{\begin{array}{c}\cos(m\phi)\\ -\sin(m\phi)\end{array}\right\}e^{-jk_z z} \tag{2.20}$$

$$E_\phi = \frac{-j\omega\mu k_r}{k^2 - k_z^2}J'_m(k_r r)\left\{\begin{array}{c}\sin(m\phi)\\ \cos(m\phi)\end{array}\right\}e^{-jk_z z} \tag{2.21}$$

The boundary conditions remain the same as the TM case, however vanishing E_z, E_r, and H_ϕ requires that $J'_m(k_r a) = 0$. Therefore,

$$k_r = \frac{X'_{mn}}{a} \tag{2.22}$$

and the dispersion relation is

$$k_z = \sqrt{\omega^2\mu\varepsilon - (X'_{mn}/a)^2}. \tag{2.23}$$

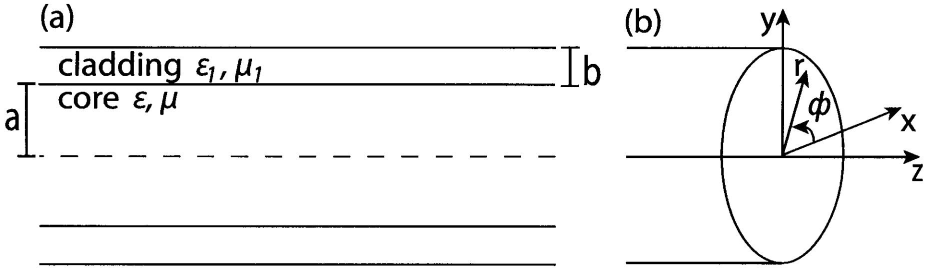

Figure 2-5: (a) The parameters of a dielectric cylindrical waveguide with a radius of a for the core and a width of b for the cladding. (b) The cylindrical geometry, for reference.

The cutoff frequency for the TE_{mn} mode of $f_{c,mn} = cX'_{mn}/2\pi a$.

For completeness, select TE fields are shown in Figure 2-4. The modes shown in this figure and all $\mathrm{TE}_{0n}(n > 0)$ also propagate in corrugated cylindrical waveguide. Other TE modes do not satisfy the boundary conditions for corrugated waveguide, discussed in the next section.

The magnitude plots of the TE modes in Figure 2-4 follow a similar pattern to the TM modes in Figure 2-3, however they are off by 1 radial index. It should be noted that the TE_{0n} and $\mathrm{TM}_{0(n+1)}$ modes have E_ϕ[TE] and H_z[TE] of the same form as H_ϕ[TM] and E_z[TM], respectively. It can also be seen that the TE_{0m} modes are degenerate with the TM_{1m} modes, meaning that they have the same propagation constant.

2.2 Hybrid Modes in Corrugated Waveguides

2.2.1 Modes of a Dielectric Waveguide

The hybrid modes, referred to as the EH and HE modes, of a corrugated waveguide are found by recognizing two conditions. One, a corrugated waveguide is mathematically similar to a dielectric waveguide in the way that maxwell's equations will be solved [21]. Two, instead of dielectric waveguide boundary conditions, the corrugations in the waveguide create wall functions which impose their own boundary conditions on the modes in the waveguide [11].

For a dielectric waveguide, shown in Figure 2-5, the wave equation 2.6 remains the same, and one solution for the E_z and H_z fields inside the waveguide, $r < a$, is

$$E_z = AJ_m(k_r r)\sin(m\phi)e^{-jk_z z} \tag{2.24}$$

$$H_z = BJ_m(k_r r)\cos(m\phi)e^{-jk_z z}, \tag{2.25}$$

as shown in the previous section. Alternatively, E_z and H_z could have a 90 degree phase difference and depend on $\cos(m\phi)$ and $\sin(m\phi)$ (or $e^{jm\phi}$ and $e^{-jm\phi}$) respectively, but that is an arbitrary distinction given the azimuthal symmetry of the waveguide. For simplicity only the first case will be discussed, but that alternative solution will be kept in mind for the discussion of LP modes in the next section, where it will play an important role in defining a complete basis set.

Instead of splitting these two solutions, as was done for the discussion of TE and TM modes, we will consider both fields simultaneously to create the Hybrid Electric modes. Thus, we arrive at the field solutions for a dielectric waveguide for $r < a$

$$E_r = \frac{1}{k_r^2}\left[Ajk_z k_r J_m'(k_r r)\sin(m\phi) - B\frac{j\omega\mu m}{r}J_m(k_r r)\sin(m\phi)\right]e^{-jk_z z} \tag{2.26}$$

$$E_\phi = \frac{1}{k_r^2}\left[A\frac{jk_z m}{r}J_m(k_r r)\cos(m\phi) - Bj\omega\mu k_r J_m'(k_r r)\cos(m\phi)\right]e^{-jk_z z} \tag{2.27}$$

$$H_r = \frac{1}{k_r^2}\left[Bjk_z k_r J_m'(k_r r)\cos(m\phi) - A\frac{j\omega\varepsilon m}{r}J_m(k_r r)\cos(m\phi)\right]e^{-jk_z z} \tag{2.28}$$

$$H_\phi = \frac{1}{k_r^2}\left[-B\frac{jk_z m}{r}J_m(k_r r)\sin(m\phi) - Aj\omega\varepsilon k_r J_m'(k_r r)\sin(m\phi)\right]e^{-jk_z z} \tag{2.29}$$

For $r > a$, the field decays and follows the modified Hankel function, such that the $\hat{z}$-directed fields, as solved by the wave equation, are

$$E_z = CH_m^{(1)}(jk_{rI} r)\sin(m\phi)e^{-jk_z z} \tag{2.30}$$

$$H_z = DH_m^{(1)}(jk_{rI} r)\cos(m\phi)e^{-jk_z z}, \tag{2.31}$$

where k_{rI} is the imaginary component of the $\hat{r}$-directed wavenumber in the cladding

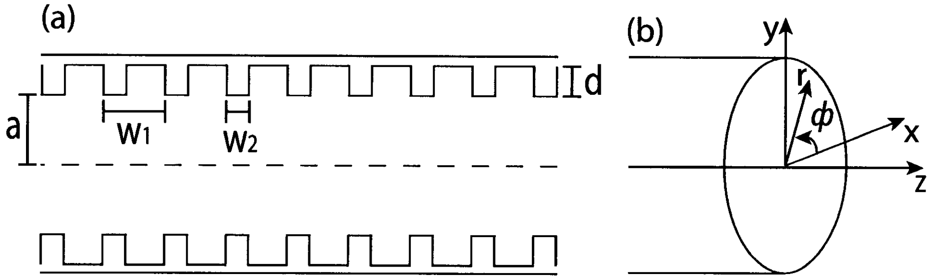

Figure 2-6: (a) The parameters of a corrugated cylindrical waveguide with a radius of a and corrugation of depth, d. The waveguide corrugations are not drawn to scale. (b) The cylindrical geometry, for reference.

of the dielectric waveguide. That is, $k_{1r} = jk_{rI}$, and the dispersion relation in the cladding is $k_1^2 = \omega^2\mu_1\varepsilon_1 = k_z^2 - k_{1r}^2$. The transverse fields for the cladding can be found with the wave equation, as shown in [20].

The differing EH and HE modes arise when considering the rather complicated guidance condition for dielectric waveguides. The further derivation of Hybrid modes in dielectric waveguide is outside of the scope of the thesis, but the reader is referred to [20], [27], and [37] for further discussion and a more complete derivation of the hybrid modes.

2.2.2 Modes of a Corrugated Metallic Waveguide

For a corrugated waveguide, depicted in Figure 2-6 (reproduced from Chapter 1), it is sufficient to say that the wall functions will serve to implement the guidance condition on the waveguide [15]. These functions will determine the standing wave fields in the corrugations for $a < r < a + d$, taking the place of the decaying fields in the cladding of the dielectric waveguide. The standing wave fields in the corrugations will specify the boundary conditions for the fields when $r < a$. It is important to keep in mind that the main difference between these two types of waveguide is that $E \to 0$ at $r = a$ for a corrugated waveguide, whereas E is finite at $r = a$ for a dielectric waveguide.

Within the corrugation at $r = a + d$, $E_z = 0$ and H_ϕ is maximized. These conditions lead to the wall impedance in the z direction as,

$$Z_z = \frac{E_z(r=a)}{H_\phi(r=a)} = Z_0 \tan(kd), \tag{2.32}$$

where k is the wavenumber and Z_0 is defined by the corrugation widths,

$$Z_0 = -j\frac{w_1 - w_2}{w_1}\sqrt{\frac{\mu_0}{\varepsilon_0}} \tag{2.33}$$

(see Figure 1-1 for parameter definitions) [11], [15]. For the case considered in this thesis $d = \lambda/4$, such that $Z_z = \infty$, and $H_\phi(r=a) = 0$. This condition extends to the transverse electric field components, such that $E_\phi(r=a) = 0$ and $E_r(r=a) = 0$.

With these wall impedances, the electric fields for the $\mathrm{HE}_{mn}(m, n > 0)$ modes for a corrugated waveguide can be written as

$$\begin{aligned} E_x &= A\left[J_{m-1}\left(\frac{K_{m-1,n}r}{a}\right)\sin\left([m-1]\phi\right)\right. \\ &\left. +\frac{\Delta X^2_{m-1,n}}{4mka}J_{m+1}\left(\frac{K_{m-1,n}r}{a}\right)\sin\left([m+1]\phi\right)\right] \end{aligned} \tag{2.34}$$

$$\begin{aligned} E_y &= A\left[J_{m-1}\left(\frac{K_{m-1,n}r}{a}\right)\cos\left([m-1]\phi\right)\right. \\ &\left. -\frac{\Delta X^2_{m-1,n}}{4mka}J_{m+1}\left(\frac{K_{m-1,n}r}{a}\right)\cos\left([m+1]\phi\right)\right] \end{aligned} \tag{2.35}$$

$$E_z = -jA\frac{X_{m-1,n}}{ka}J_m\left(\frac{K_{m-1,n}r}{a}\right)\sin\left(m\phi\right) \tag{2.36}$$

where A is the amplitude of the electric field, X_{mn} is the nth root of the mth Bessel function, and η is impedance. In addition, K_{mn} is defined as

$$K_{mn} = X_{mn}\left(1 - \frac{\Sigma}{2ka}\right) \tag{2.37}$$

and Δ is a function defined for corrugated waveguides as

$$\Delta = -\frac{w_1 + w_2}{w_1} \frac{1 + \frac{2\tan kd}{ka}}{\tan kd} \tag{2.38}$$

with $\Sigma = \Delta$ in this case. Σ and Δ are both considered wall functions, meaning that they depend on the impedance of the wall and, if changed, indicate a different type of cylindrical waveguide. Since we are only concerned with quarter-wavelength corrugations, $kd = pi/2$, we can evaluate (2.38) to $\Sigma = \Delta = 0$. Therefore, we can also evaluate $K_{mn} = X_{mn}$. In addition, the value ka is large for oversized waveguide, so the HE$_{mn}$ electric field is simplified as

$$E_x = AJ_{m-1}\left(\frac{X_{m-1,n}r}{a}\right) sin\left([m-1]\phi\right) \tag{2.39}$$

$$E_y = AJ_{m-1}\left(\frac{X_{m-1,n}r}{a}\right) cos\left([m-1]\phi\right) \tag{2.40}$$

$$E_z \approx 0. \tag{2.41}$$

For the EH$_{mn}$ modes the electric field can also be defined using the same parameters

$$\begin{aligned} E_x &= A\left[J_{m+1}\left(\frac{K_{m+1,n}r}{a}\right)\cos\left([m+1]\phi\right)\right. \\ &\left.-\frac{\Delta X_{m+1,n}^2}{4mka}J_{m-1}\left(\frac{K_{m+1,n}r}{a}\right)\cos\left([m-1]\phi\right)\right] \end{aligned} \tag{2.42}$$

$$\begin{aligned} E_y &= A\left[J_{m+1}\left(\frac{K_{m+1,n}r}{a}\right)\sin\left([m+1]\phi\right)\right. \\ &\left.+\frac{\Delta X_{m+1,n}^2}{4mka}J_{m-1}\left(\frac{K_{m+1,n}r}{a}\right)\sin\left([m-1]\phi\right)\right] \end{aligned} \tag{2.43}$$

$$E_z = jA\frac{X_{m+1,n}}{ka}J_m\left(\frac{K_{m+1,n}r}{a}\right)\cos\left(m\phi\right) \tag{2.44}$$

In addition, the same approximations can be made as in the HE$_{mn}$ modes for quarter-wavelength corrugations. Therefore, the EH$_{mn}$ electric field is approximated as

$$E_x = AJ_{m+1}\left(\frac{X_{m+1,n}r}{a}\right)\cos\left([m+1]\phi\right) \tag{2.45}$$

$$E_y = AJ_{m+1}\left(\frac{X_{m+1,n}r}{a}\right)\sin\left([m+1]\phi\right) \tag{2.46}$$

$$E_z \approx 0. \tag{2.47}$$

For both HE and EH modes, the magnetic fields are defined via the electric fields as

$$H_x = -\frac{E_y}{\eta} \tag{2.48}$$

$$H_y = \frac{E_x}{\eta} \tag{2.49}$$

$$H_z = -\frac{E_z}{\eta}\tan\left(m\phi + \theta\right). \tag{2.50}$$

See [9] for further explanation. For the HE$_{1n}$ mode, it is common to approximate the transverse fields as

$$E_y = AJ_0\left(\frac{X_{0n}r}{a}\right) \tag{2.51}$$

$$H_x = -\frac{A}{\eta}J_0\left(\frac{X_{0n}r}{a}\right) \tag{2.52}$$

with E_x, E_z, H_y, and H_z negligibly small [34]. This approximation will be justified for LP modes in the next section.

2.2.3 Descriptions of modes

For a corrugated cylindrical waveguide, the HE$_{11}$ mode is the fundamental mode of the guide. As shown in Figure 2-7, the transverse components of the electric and magnetic field have no azimuthal or radial variations and are polarized in the $\hat{y}$-direction. The $\hat{z}$-directed field is non-zero, but falls by a factor of λ/a comparative to the transverse fields, so it is negligible for the oversized waveguides discussed here. For reference, other HE$_{mn}$ modes are depicted in Figure 2-7 and EH$_{mn}$ modes are shown in Figure 2-8. Note that all HE_{1n} modes are polarized in the $\hat{y}$-direction.

At this point, recall that the assignation of cosine and sine dependence on ϕ to $\hat{x}$ and $\hat{y}$-directed electric fields was arbitrary. Therefore, it would also be possible to have HE_{1n} modes which are polarized in the $\hat{x}$-direction with a transformation of $\phi \rightarrow \phi' + \pi/2$. This concept of polarization will be further explored in the discussion on LP modes.

2.3 Linearly Polarized (LP) Modes

The following section is adapted from Kowalski et al. 2010, in review [21].

In a cylindrical corrugated waveguide, all of the HE and EH modes will propagate. However, this does not form a complete basis set. For the entire hybrid mode basis set, one must also consider the TE_{0n} and TM_{0n} modes for corrugated wavegudie which are the same as the previously derived modes for smooth-wall waveguide [11].

A wave propagating in a corrugated waveguide may be formed through the summation of the hybrid modes. However, for practical characterization of the wave it is not enough to just describe the amplitude of the propagating wave through the hybrid mode basis set; the polarization of the wave must be also considered. In applications, gyrotrons are used to produce Gaussian beam inputs into the transmission line. These inputs are linearly polarized beams, and must propagate as a summation of modes which is linearly polarized. The fundamental mode of corrugated waveguide, the HE_{11} mode is linearly polarized. However, the hybrid modes, in general, do not satisfy the linear polarization condition.

In this section, a set of linearly polarized eigenmodes (LP_{mn}) for corrugated metallic waveguide is derived. Since gyrotron beams are linearly polarized, the LP_{mn} mode set has advantages for describing this radiation.

2.3.1 Derivation of Modes

Linearly polarized modes will be formed in much the same was as the HE modes were formulated. Since we are still using corrugated cylindrical waveguide, the

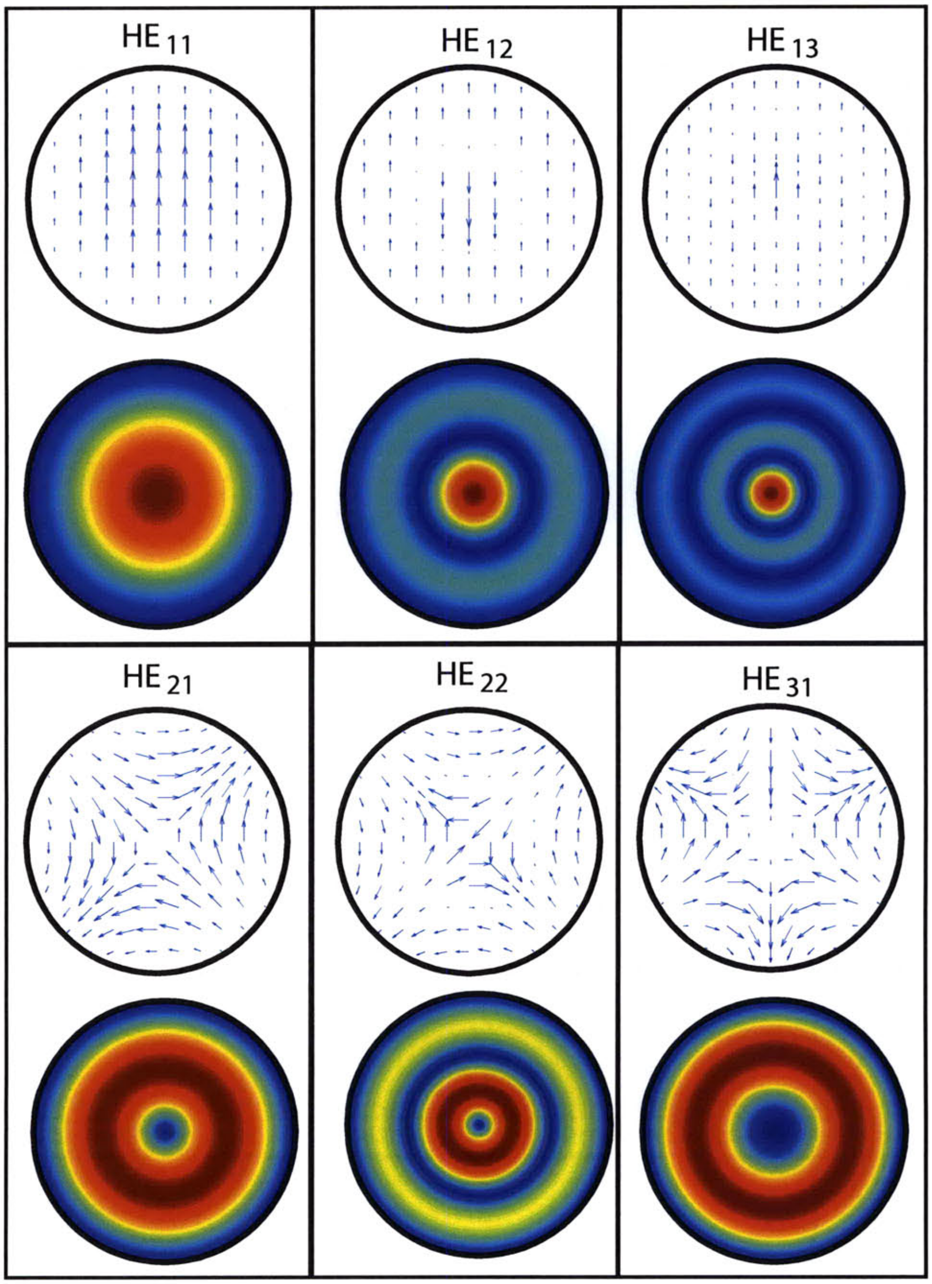

Figure 2-7: The transverse electric field magnitude and vector plots for select HE_{mn} modes which will propagate in a corrugated waveguide. The black circle indicates the waveguide wall.

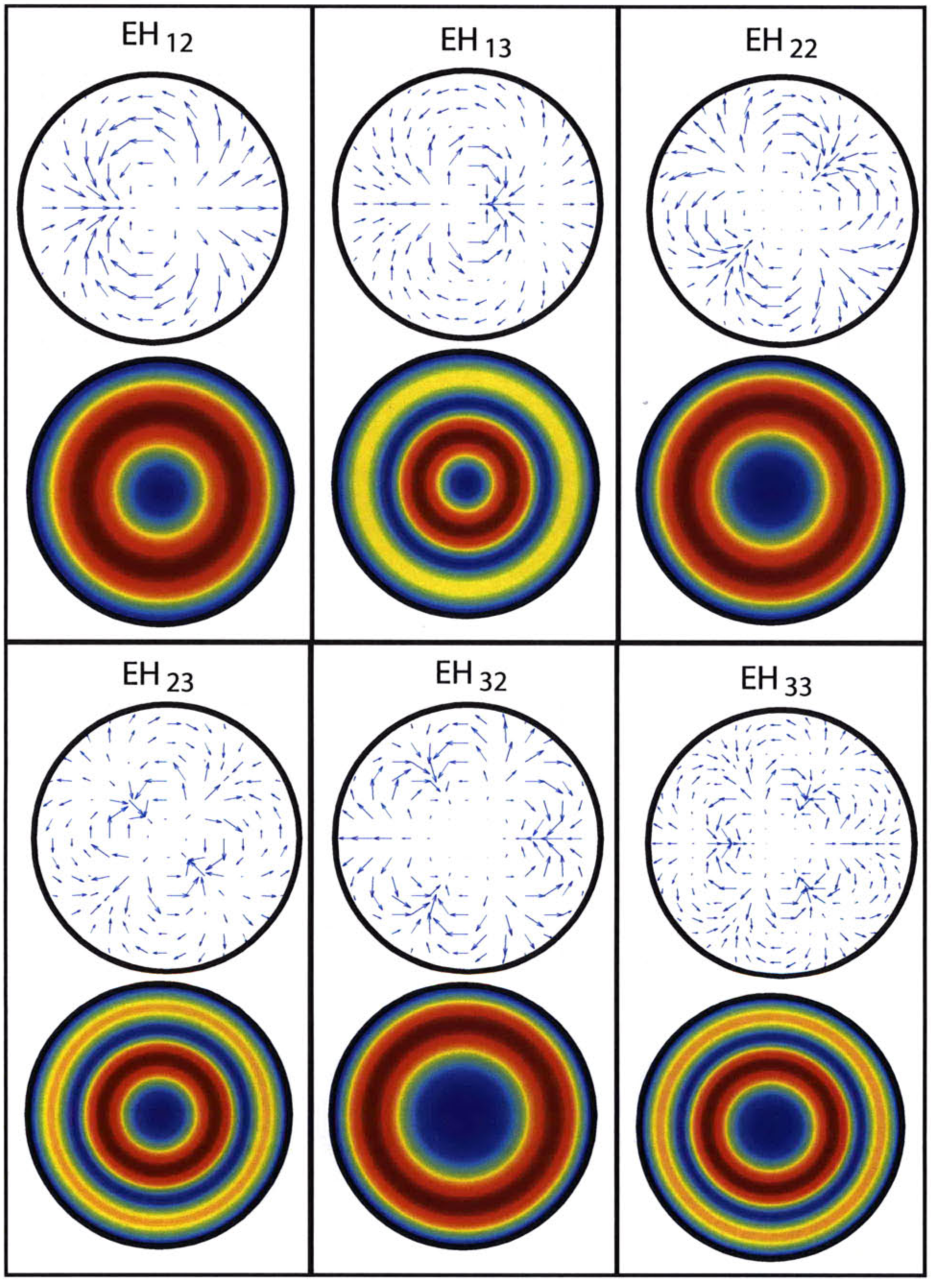

Figure 2-8: The transverse electric field magnitude and vector plots for select EH_{mn} modes which will propagate in a corrugated waveguide. The black circle indicates the waveguide wall.

boundary conditions for the field remain the same as the hybrid mode case. However, in the linearly polarized case it is useful to discuss the fields as being directed in Cartesian coordinates, such that the electric field is defined as $\vec{E}(r,\phi,z) = E_x(r,\phi,z)\hat{x} + E_y(r,\phi,z)\hat{y} + E_z(r,\phi,z)\hat{z}$, where

$$E_y = E_r \sin\phi + E_\phi \cos\phi. \tag{2.53}$$

$$E_x = E_r \cos\phi - E_\phi \sin\phi. \tag{2.54}$$

and the magnetic field is similarly defined. To polarize in the $\hat{y}$ direction, E_x must be zero, which implies that $E_r = f(r,\phi,z)\sin\phi$, and $E_\phi = f(r,\phi,z)\cos\phi$. These forms satisfy the wave equations for cylindrical coordinates and boundary conditions imposed by the corrugations, so long as $f(a,\phi,z) = 0$. Therefore, $E_y = f(r,\phi,z)$ and the boundary condition that must be satisfied for linearly polarized modes is $E_y(r=a,\phi,z) = 0$. This extrapolation of E_y is similar to the definition of LP modes for dielectric waveguides, as in [37]. Once again, the difference between the dielectric and corrugated case is the boundary conditions; whereas dielectric guides have finite fields at the wall, the metallic guides considered here have $E_y = 0$ at the wall of the guide, as shown in the previous section.

Solving for the fields in the waveguide requires E_y to satisfy the wave equation, as well. Though the electric field is discussed in Cartesian coordinates to satisfy the linearly polarized condition, it is more convenient to use cylindrical variables to express the function, such that

$$\frac{\partial^2 E_y}{\partial r^2} + \frac{1}{r}\frac{\partial E_y}{\partial r} + \frac{1}{r^2}\frac{\partial^2 E_y}{\partial \phi^2} + \frac{\partial^2 E_y}{\partial z^2} + \frac{\omega^2}{c^2}E_y = 0. \tag{2.55}$$

Assuming a $\hat{z}$-dependence of $e^{-jk_z z}$ and a $\hat{\phi}$-dependence of $\cos(m\phi)$ or $\sin(m\phi)$ the wave equation is reduced to

$$r^2\frac{\partial^2 E_y}{\partial r^2} + r\frac{\partial E_y}{\partial r} + \left[(k_r r)^2 - m^2\right] E_y = 0. \tag{2.56}$$

which is the Bessel function differential equation, as previously described in Eq. 2.7. Again, the Bessel function of the first kind is chosen to satisfy finite electric field conditions, such that

$$E_y(r, \phi, z) = AJ_m(k_r r) \left\{ \begin{array}{c} \cos(m\phi) \\ \sin(m\phi) \end{array} \right\} e^{-jk_z z}, \tag{2.57}$$

where A is a constant and either sinusoidal dependence on ϕ is possible. Unlike the HE case, we will keep both the sinusoidal and cosinusoidal solutions to keep the full basis set. The boundary condition $E_y(a, \phi, z) = 0$ requires that $k_r = X_{mn}/a$, where X_{mn} is the n^{th} zero of the m^{th} Bessel function. Through Maxwell's equations, the dominant field components for LP$_{mn}$ modes are

$$E_{y,mn}(r, \phi) = AJ_m\left(\frac{X_{mn}r}{a}\right) \left\{ \begin{array}{c} \cos(m\phi) \\ \sin(m\phi) \end{array} \right\} e^{-jk_z z}, \tag{2.58}$$

$$H_{x,mn}(r, \phi) = \frac{-Ak_z}{\omega\mu_0} J_m\left(\frac{X_{mn}r}{a}\right) \left\{ \begin{array}{c} \cos(m\phi) \\ \sin(m\phi) \end{array} \right\} e^{-jk_z z}, \tag{2.59}$$

The longitudinal components, E_z and H_z, and the transverse magnetic field in the $\hat{y}$-direction, H_y, are nonzero, but negligible by a factor of λ/a. The transverse electric field in the $\hat{x}$-direction is defined due to the linear polarization condition as $E_x = 0$.

The odd and even LP$_{mn}$ modes are defined with a perpendicular electric field as

$$\vec{E}^{\perp}_{mn}(r, \phi) = \hat{y}AJ_m\left(\frac{X_{mn}r}{a}\right) \left\{ \begin{array}{ll} \cos(m\phi) & \text{(odd)} \\ \sin(m\phi) & \text{(even).} \end{array} \right. \tag{2.60}$$

To create an orthonormal basis set, a normalization factor is calculated

$$N_{mn} = \int_0^a \int_0^{2\pi} \left[E^{\perp}_{mn}(r, \phi)\right]^2 r \, d\phi dr. \tag{2.61}$$

Mode	X_{mn}	Degenerate modes
LP_{01}	2.405	HE_{11}
$\mathrm{LP}_{11}^{(o)}$	3.832	TE_{01}, HE_{21}
$\mathrm{LP}_{11}^{(e)}$	3.832	TM_{02}, HE_{21}
LP_{21}	5.136	HE_{31}, EH_{12}
LP_{02}	5.520	HE_{12}
LP_{31}	6.380	HE_{41}, EH_{22}
$\mathrm{LP}_{12}^{(o)}$	7.016	TE_{02}, HE_{22}
$\mathrm{LP}_{12}^{(e)}$	7.016	TM_{03}, HE_{22}
LP_{22}	8.417	HE_{32}, EH_{13}
LP_{03}	8.653	HE_{13}
LP_{32}	9.761	HE_{42}, EH_{23}
$\mathrm{LP}_{13}^{(o)}$	10.17	TE_{03}, HE_{23}
$\mathrm{LP}_{13}^{(e)}$	10.17	TM_{04}, HE_{23}

Table 2.1: Select LP modes with corresponding degenerate modes.

For LP_{0n} (HE_{1n}) modes, this normalization evaluates to

$$N_{0n} = A^2 \pi a^2 J_1^2(X_{0n}), \tag{2.62}$$

and for all other LP_{mn} modes, where $m \neq 0$,

$$N_{mn} = A^2 \frac{\pi a^2}{2} J_{m-1}^2(X_{mn}). \tag{2.63}$$

With this factor,

$$u_{mn} = E_{mn}^{\perp} / \sqrt{N_{mn}}, \tag{2.64}$$

such that u_{mn} is a simple way to express the normalized LP_{mn} mode.

2.3.2 Relationship between Hybrid and LP modes

Any wave propagating in the corrugated metallic waveguide can be projected onto an orthonormal basis set of modes. Both the hybrid modes and the LP_{mn} modes form such a basis set. Here, we indicate the relationships between these two basis sets and show how the LP_{mn} modes can be constructed from the hybrid mode basis set.

As can be shown in Figure 2-7, the HE_{1n} modes are also the LP_{01} modes. The

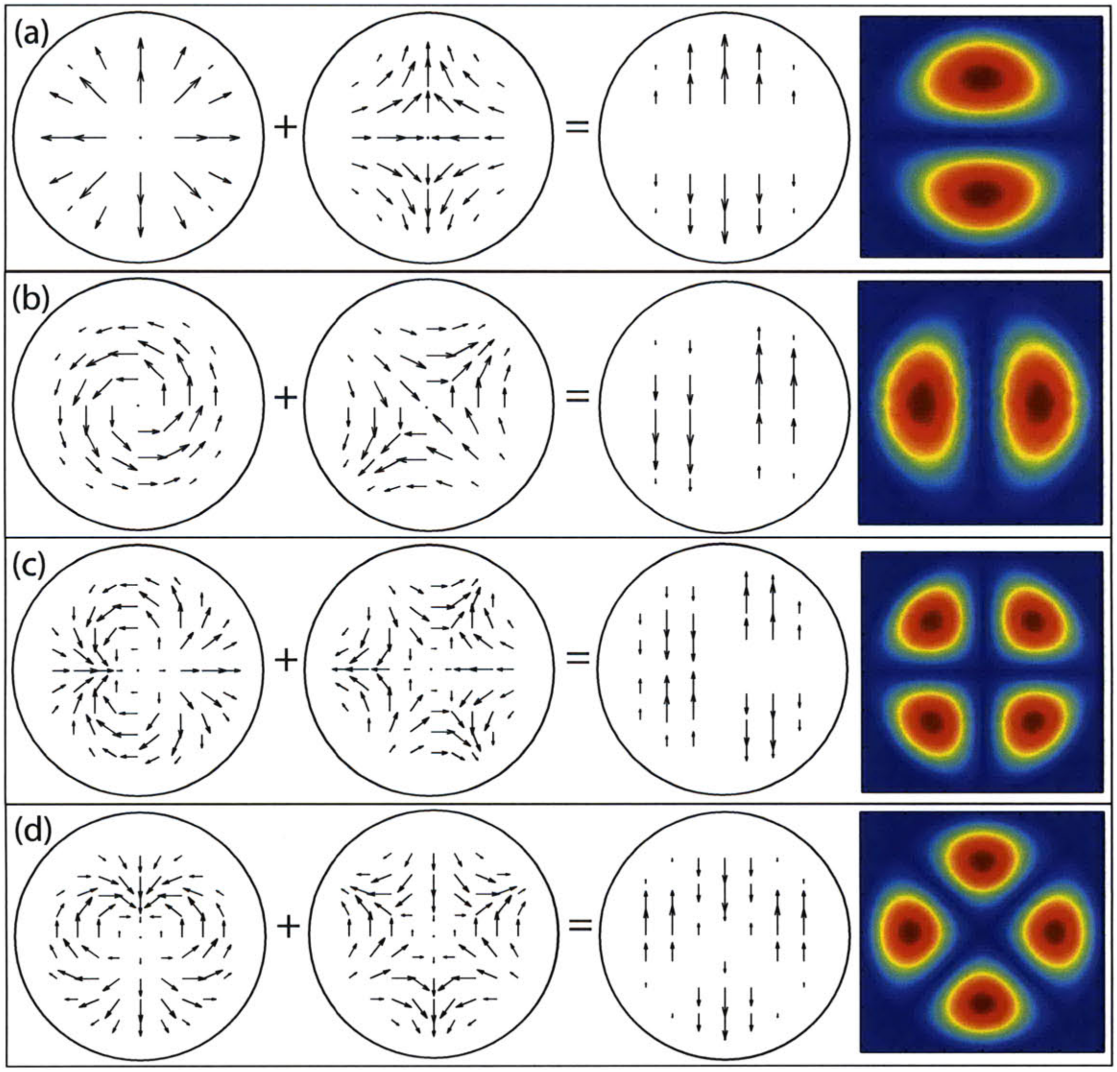

Figure 2-9: Field vector plots demonstrating the construction of LP modes from TE, TM, and HE modes. The added modes have identical propagation constants. (a) TM_{02} + HE_{21} rotated 45° = $\mathrm{LP}_{11}^{(e)}$; (b) $-\mathrm{TE}_{01}$ + HE_{21} = $\mathrm{LP}_{11}^{(o)}$; (c) EH_{12} rotated $-90°$ + HE_{31} rotated $-90°$ = $\mathrm{LP}_{21}^{(e)}$; (d) EH_{12} rotated 180° + HE_{31} = $\mathrm{LP}_{21}^{(o)}$.

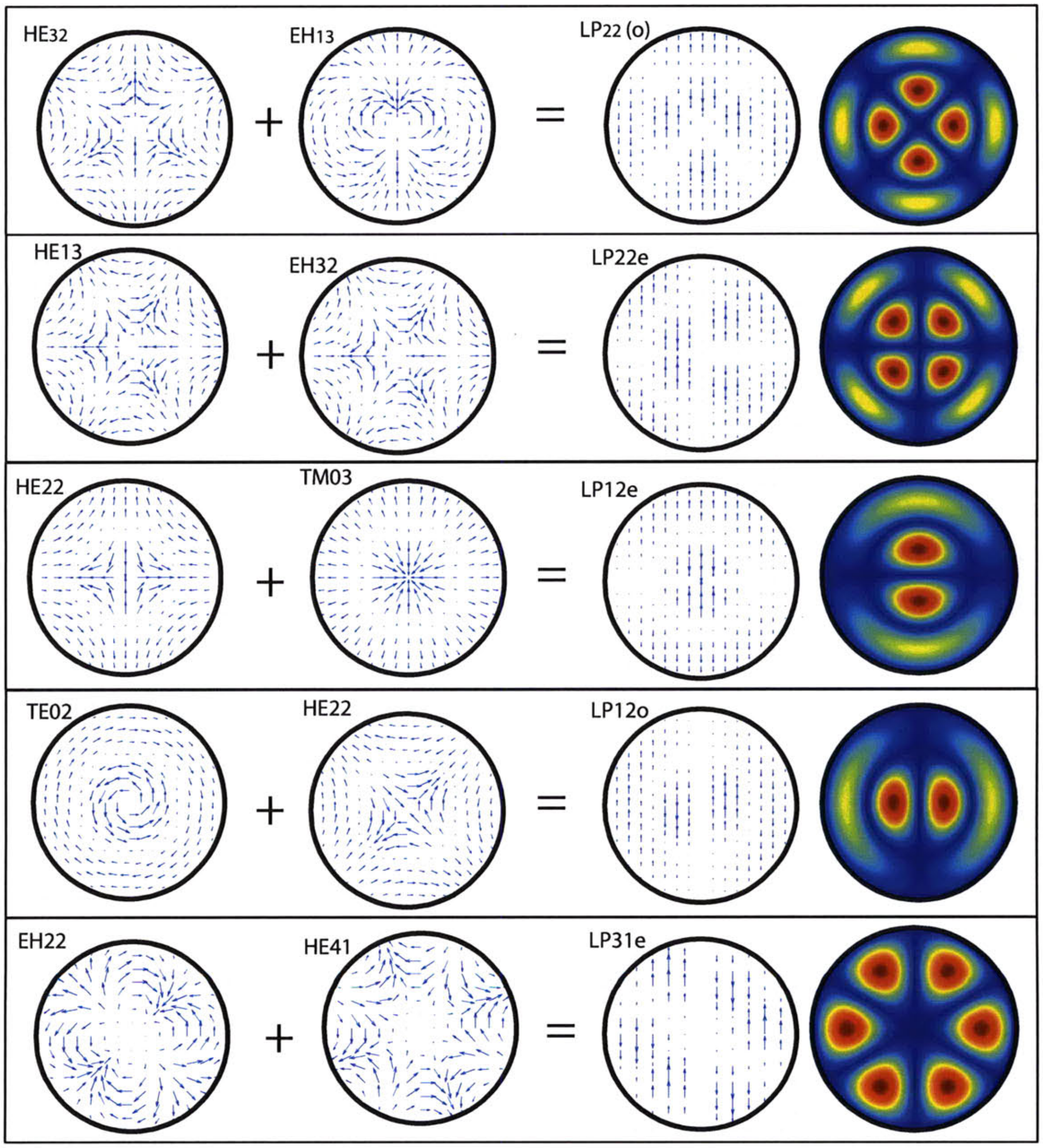

Figure 2-10: Field vector plots demonstrating the construction of LP modes from TE, TM, HE, and EH modes. The added modes have identical propagation constants.

electric field for the HE_{1n} modes was already polarized. Therefore, the HE_{1n} notation will be kept in order to agree with the existing literature; this assignment is useful for discussing the fundamental HE_{11} mode.

Other LP_{mn} modes can be constructed through the addition of HE_{mn}, EH_{mn}, TE_{0n}, or TM_{0n} modes with the same propagation constants (degenerate modes). Table 2.1 lists these degenerate modes. Figures 2-9 and 2-10 illustrate, for a few LP modes, how the addition of hybrid modes can form LP_{mn} modes. For all examples, the LP modes are constructed with a 1:1 power ratio of two hybrid modes and the hybrid modes are rotated along the $\hat{z}$-axis to cancel $\hat{x}$-components of the electric fields. Cancellation of the $\hat{y}$-components could be achieved in a similar manner to form the $\hat{x}$-directed LP modes. A 180° phase shift between the hybrid modes corresponds to subtraction, as seen in Figure 2-9(b). The first two examples, the LP_{11} modes, were previously described in [3]. Through the field vector plots, Figure 2-9 demonstrates this relationship between LP modes and HE, EH, TE, and TM modes. For example, the $\mathrm{LP}_{11}^{(e)}$ mode can be constructed by adding the TM_{02} mode and the HE_{21} mode, rotated by 45° as seen in Figure 2-9(a). When adding these modes, the $\hat{x}$-components of the field cancel while the $\hat{y}$-components add, resulting in a $\hat{y}$-directed linearly polarized field. All three of these modes are characterized by the Bessel function zero $X_m = 3.832$ and, therefore, have the same beat wavelength with the HE_{11} mode.

Conversely, the hybrid modes may be constructed from the LP modes since both sets form complete basis sets. The complete LP mode basis set consists of the even and odd forms as well as $\hat{x}$ and $\hat{y}$-directed modes for each form. That is, each LP_{mn} indexed mode consists of 4 degenerate modes: $\mathrm{LP}_{mn}^{(e)}[\hat{x}]$, $\mathrm{LP}_{mn}^{(o)}[\hat{x}]$, $\mathrm{LP}_{mn}^{(e)}[\hat{y}]$, $\mathrm{LP}_{mn}^{(o)}[\hat{y}]$. (Except for LP_{0n}, which has only two degenerate modes since the odd and even forms are identical.) For example, the TM_{02} mode is equivalent to $\mathrm{LP}_{11}^{(o)}[\hat{y}]-\mathrm{LP}_{11}^{(e)}[\hat{x}]$. For the TM_{02} mode, the electric field is

$$E = \hat{\phi} A J_m \left(\frac{X_{mn} r}{a} \right) \tag{2.65}$$

which is equivalent to

$$E = \hat{y} A J_m \left(\frac{X_{mn} r}{a} \right) \cos\phi - \hat{x} A J_m \left(\frac{X_{mn} r}{a} \right) \sin\phi \tag{2.66}$$

which are the equivalent fields for for the modes $\mathrm{LP}_{11}^{(o)}[\hat{y}]$ and $-\mathrm{LP}_{11}^{(e)}[\hat{x}]$, respectively. Using Table 2.1 as a refernce list for degenerate modes, all hybrid modes can be constructed from their degenerate LP modes.

Since both sets of modes are basis sets, it is possible to use either set to describe a linearly polarized beam in a waveguide. However, it is necessary to account for HE, EH, TE, and TM modes that result in combinations (like those listed above) to preserve linear polarization. Due to this restriction, it is more convenient to consider the LP mode basis set for analysis in corrugated cylindrical waveguides with linearly polarized experimental inputs.

Chapter 3

Theoretical Calculations of Power Loss in Corrugated Waveguide Components

The theoretical loss in overmoded waveguide components is well-established for the propagation of the fundamental HE_{11} mode. However, the theoretical loss due to a LP_{mn} multi-mode system is necessary for the discussion of gyrotron applications. This section discusses the theoretical loss present in straight sections of waveguide, a gap of waveguide, and a 90° miter bend. The theory is applicable to quarter-wavelength corrugated waveguide, and all calculations are performed for 170 GHz 63.5 mm diameter waveguide.

This chapter also shows that calculations of transmission through waveguide components for the fundamental HE_{11} mode is largely dependent on the higher order modes in the system. Previously, [13] calculated the loss in a gap for the HE_{11} mode, and [33] expanded the calculation to also include the effect of an HE_{12} mode; it was found that the loss in HE_{11} is dependent on the phase between the HE_{11} and HE_{12} modes. This chapter expands the calculation of loss in a gap to include the effects of other higher order modes in a multi-mode system on the transmission of the fundamental HE_{11} mode.

3.1 Straight Sections of Waveguide

The loss in straight sections of overmoded corrugated cylindrical waveguide is well established, as discussed in the review of the literature. The fundamental mode of the corrugated waveguide, the HE_{11} mode, has less attenuation than the fundamental modes for equivalent smooth-wall cylindrical and rectangular waveguides. This effect is reviewed for frequencies from 1–10 GHz in [4] and for the 100 GHz range in [1]. Overmoded corrugated waveguides have extremely low losses at high frequencies, even for higher order modes [22], [3]. The attenuation for a corrugated guide scales inversely with the cube of the radius to wavelength ratio, a/λ.

For most purposes, when quarter-wavelength corrugations are considered, the attenuation loss in straight sections is negligible. However, if the guide size (a/λ) is too large for the application at hand, power will be lost when the beam is injected into the system due to coupling into HOMs. For this reason, the ITER application limits the ratio to $a/\lambda = 18$. This ratio creates a reasonably sized waveguide into which a Gaussian beam from a gyrotron output with a waist size $w_0 = 0.64a$ can easily couple.

The Ohmic loss for ITER transmission lines is discussed at length in [12] and [14], and calculated as 0.18×10^{-4} Np/m (or 1.6×10^{-4} dB/m). As shown in [31], the ohmic loss in straight sections is negligible, particularly when compared to other methods of loss on the line.

Though the attenuation in straight sections is negligible, it is pertinent to note that a multi-mode system has the ability to produce mode-beating which can be observed over straight sections of the line. For example, consider a two-mode system which propagates as

$$\vec{E} = \vec{E}_{m_1n_1} + \vec{E}_{m_2n_2}, \tag{3.1}$$

where $\vec{E}_{mn} = \sqrt{A_{mn}}u_{mn}e^{-jk_{z,mn}z}$, u_{mn} is defined in (2.64), and A_{mn} is the power in a particular mode. Then, to calculate the power in the system

$$|E|^2 = \left|\sqrt{A_{m_1n_1}}u_{m_1n_1}e^{-jk_1z} + \sqrt{A_{m_2n_2}}u_{m_2n_2}e^{-jk_2z}\right|^2 \tag{3.2}$$

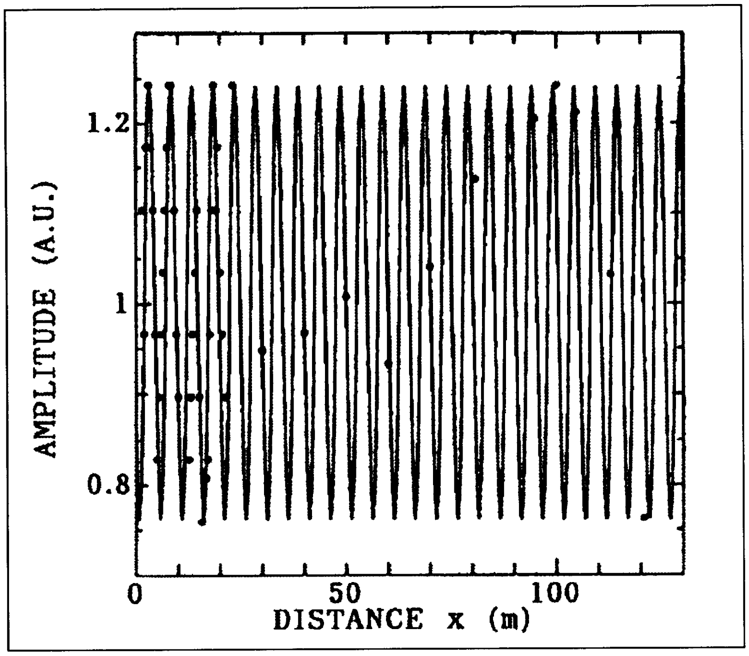

Figure 3-1: The measured amplitude of a 140 GHz wave as it travels through 88.9 mm diameter corrugated waveguide, as observed by [26].

which can be expanded to

$$\begin{aligned} |E|^2 = & \left[\sqrt{A_{m_1n_1}}u_{m_1n_1}\cos(k_{z,m_1n_1}z) + \sqrt{A_{m_2n_2}}u_{m_2n_2}\cos(k_{z,m_2n_2}z)\right]^2 \\ & + \left[\sqrt{A_{m_1n_1}}u_{m_1n_1}\sin(k_{z,m_1n_1}z) + \sqrt{A_{m_2n_2}}u_{m_2n_2}\sin(k_{z,m_2n_2}z)\right]^2 \end{aligned} \tag{3.3}$$

and reduced to

$$|E|^2 = A_{m_1n_1} + A_{m_2n_2} + 2\sqrt{A_{m_1n_1}A_{m_2n_2}}\cos(\Delta k z), \tag{3.4}$$

or

$$|E|^2 = 1 + 2\sqrt{A_{m_1n_1}A_{m_2n_2}}\cos(\Delta k z), \tag{3.5}$$

since all power must be accounted for in the system. We have defined $\Delta k = k_{z,m_1n_1} - k_{z,m_2n_2}$, the difference between the propagation vectors of the modes. This analysis indicates that the power in a two-mode system oscillates with a wavelength of $2\pi/\Delta k$.

This mode beating effect was previously observed by [26] and is reproduced in

Figure 3-1. In the study, a beating with a normalized linear amplitude of 0.24 was observed with $\Delta k = 1.1245/\text{m}$. The parameters observed correspond to beating between 98.5% HE_{11} and 1.5% LP_{11} modes. Just a small amount of higher order mode in the system caused a large fluctuation in the measured transmission through straight sections of waveguide.

For a multi-mode system, more complicated mode-beating is observed. The electric field in a generic multi-mode system is expressed as

$$\vec{E} = \sum_{p=1}^{N} \vec{E}_{m_p n_p} \tag{3.6}$$

where N is the number of modes in the system. This produces a power in the system related to

$$|E|^2 = 1 + \sum_{p=1}^{N} \sum_{\substack{q=1 \\ q \neq p}}^{N} \sqrt{A_{m_p n_p} A_{m_q n_q}} \cos\left[\left(k_{z,m_p n_p} - k_{z,m_q n_q}\right) z\right]. \tag{3.7}$$

Therefore, the power oscillates with many different frequencies dependent on the difference between wavenumbers of the propagating waves. For a system consisting of the five modes with the smallest $k_\perp$ (The "lowest order" modes), there would be ten distinct frequencies of oscillation all in the range from 1–5m. The oscillations may be significant depending on the mode content of the system, as shown in [26].

These oscillations can affect the measurements of loss in other components on the line. This effect is further complicated when several modes must be accounted for, as will be discussed when considering the baseline measurements in Chapter 5, where we characterize the transmission measured through straight sections of waveguide as a baseline measurement for data analysis.

3.2 Loss due to a Gap in Waveguide

Most waveguide transmission lines are dominated by long, straight sections of waveguide which have negligible loss when $a/\lambda \gg 1$ [11]. However, a practical waveguide

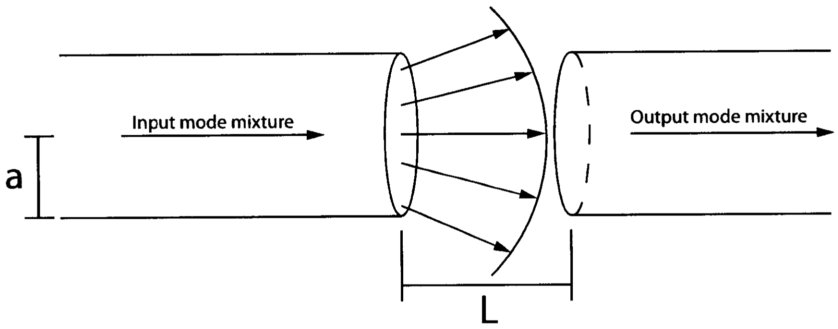

Figure 3-2: (a) A radially symmetric gap with length $L = 2a$. (b) A miter bend with a radius of a that can be modeled using equivalent gap theory, as described in the text.

system must have waveguide gaps, bends, and switches in which the wave propagates a distance without a confining wall. Losses in these components often dominate the total loss of the line. In this section, we calculate the power loss for combinations of LP$_{mn}$ modes due to a gap in straight waveguide, as depicted in Figure 3-2. This is a robust theory which will be used to approximate the loss in a miter bend in Section 3.3 and validate measurement techniques in Chapter 5.

3.2.1 Single Mode Input

For LP$_{mn}$ modes, the electric field in a gap is derived using the Fresnel Diffraction integral, an approach similar to [10]. The electric field in the gap can be calculated using the Fresnel integral [19],

$$E_g^{\perp}(x,y,z) = \frac{j}{\lambda z}\int_{-\infty}^{\infty}\int_{-\infty}^{\infty} E_i(x_0,y_0,z_0)e^{-j\frac{k}{2z}\left[(x-x_0)^2+(y-y_0)^2\right]}dx_0dy_0 \tag{3.8}$$

where $E_i(r,\phi)$ defines the transverse electric field present at the input into the gap, and z is defined as the distance into the gap after the end of the waveguide. It should be noted here that this method is a Kirchhoff approximation, in which there are negligible reflections at the truncated apertures since $a/\lambda >> 1$ [36].

Since the waveguide input may be viewed as a spherical aperture, we can transform the Fresnel integral to spherical geometry and limit the integration to the waveguide radius,

$$E_g^{\perp}(r,\phi,z) = \frac{jk}{z} e^{j\frac{kr^2}{2z}} \int_0^a \int_0^{2\pi} E_i(r_0,\phi_0,z_0) e^{j\frac{k}{2z}\left[r_0^2 - 2rr_0\cos(\phi-\phi_0)\right]} r_0 \, d\phi_0 dr_0 \tag{3.9}$$

The input into the Fresnel integral, $E_i(r,\phi)$, is the combination of modes present at the transmitting port, labeled as 'input' in Figure 3-2. In the single mode case,

$$E_i(r_0,\phi_0,z_0) = u_{mn}(r_0,\phi_0) e^{jk_z z_0}, \tag{3.10}$$

where $k_z z_0$ is the phase of the mode as it exits the waveguide, and z_0 is the location of the gap. In the single mode case, the phase of the mode is irrelevant and dropped for simplicity, such that

$$E_i(r_0,\phi_0,z_0) = u_{mn}(r_0,\phi_0). \tag{3.11}$$

Then, for an input consisting of a single normalized LP$_{mn}$ odd mode, the electric field in the gap is

$$\begin{aligned} E_g^{\perp}(r,\phi,z) = \ & \tfrac{jk}{z} \tfrac{A}{\sqrt{N_{mn}}} e^{j\frac{kr^2}{2z}} \\ & \textstyle\int_0^a \int_0^{2\pi} J_m\left(\frac{X_{mn} r_0}{a}\right) \cos(m\phi_0) e^{j\frac{k}{2z}\left[r_0^2 - 2rr_0\cos(\phi-\phi_0)\right]} r_0 \, d\phi_0 dr_0. \end{aligned} \tag{3.12}$$

The integral with respect to ϕ_0 is solved using methods discussed in [16], such that

$$\int_0^{2\pi} e^{jk\frac{rr_0}{z}\cos(phi_0 - phi) - jn\phi_0} d\phi_0 = 2\pi J_n\left(k\frac{rr_0}{z}\right) e^{jn[(\pi/2)-\phi]}. \tag{3.13}$$

Using Euler's equation to transform $\cos(m\phi_0)$, the above integral may be applied to (3.12). With some algebra, the electric field in a gap with a single mode input is

$$\vec{E}_{g,mn}^{\perp}(r,\phi,z) = \hat{y}\frac{j2\pi kA}{z\sqrt{N_{mn}}} e^{jm\frac{\pi}{2}} e^{j\frac{kr^2}{2z}} \cos(m\phi) \int_0^a J_m\left(\frac{X_n r_0}{a}\right) J_m\left(\frac{krr_0}{z}\right) e^{j\frac{kr_0^2}{2z}} r_0 dr_0. \tag{3.14}$$

where the integral with respect to r_0 must be solved numerically. Note that LP$_{mn}$ even modes result in the same $\vec{E}_{g,mn}^{\perp}(r,\phi,z)$ as (3.14) with $\cos(m\phi)$ replaced by $\sin(m\phi)$.

For a discussion on how fields propagate inside the gap, see Chapter 6. There, the discussion is expanded to consider the Fresnel diffraction of fields after leaving a waveguide (in a 'gap') when discussing launching a wave at the end of the transmission line system. In Chapter 6, the angle and offset of the beams is discussed as it radiates in free space.

To calculate the loss in a gap, the wave must enter the receiving waveguide after a length of gap, $z = L$. The received wave is labeled as 'output' in Figure 3-2. The loss is denoted as the power that does not couple back into the fundamental HE_{11} mode. If the system began with a pure mode, then the power loss in that mode is calculated as

$$\text{Loss in } \mathrm{LP}_{mn} = A_{mn} - \frac{\int_0^a \int_0^{2\pi} E_{g,mn} u_{mn} dr d\phi}{\int_0^a \int_0^{2\pi} |u_{mn}|^2 dr d\phi} \tag{3.15}$$

or, using the fact that the basis set is normalized and there is only a single mode input,

$$\text{Loss in } \mathrm{LP}_{mn} = 1 - \int_0^a \int_0^{2\pi} E_{g,mn} u_{mn} dr d\phi \tag{3.16}$$

Power loss for a specific input mode occurs in the gap for two reasons. First, as a result of diffraction, some of the power exiting the transmitting waveguide lies outside of the receiving waveguide at $r > a$ and is lost, this is called truncation loss. Second, there is power which enters the receiving waveguide but couples to secondary modes instead of the original input mode. For large a/λ, all of the modes produced in the receiving waveguide will propagate down the waveguide, the coupling to other modes results in additional power loss when considering the original mode. This is called mode conversion loss.

The power lost is largely dependent on the length of the gap. Figure 3-3 shows the loss in the fundamental mode due to a pure fundamental mode input for a gap of varying length. It is clear that as the length of the gap gets larger, more of the power is lost in the gap. Chapter 6 gives further explanation to the calculated field pattern in the gap.

For a/λ large, the power in the output port will consist primarily of power in the same mode (LP_{mn}) as was incident at the input port. Small amounts of power in other modes will also be present at the output port. These small amounts are

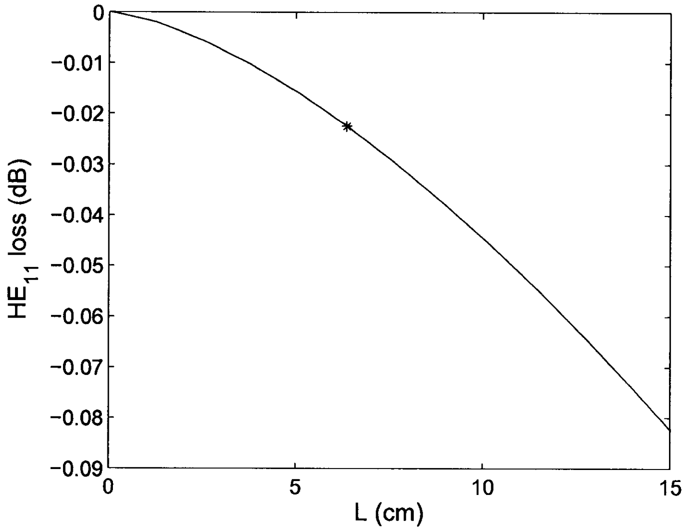

Figure 3-3: The loss in the fundamental HE_{11} mode due to a 100% HE_{11} mode input versus the length of the gap. Simulations are done at 170 GHz in 63.5 mm diameter waveguide. The red star indicates the length of gap which corresponds to $L = 2a = 63.5$ mm where the loss is 0.0227 dB.

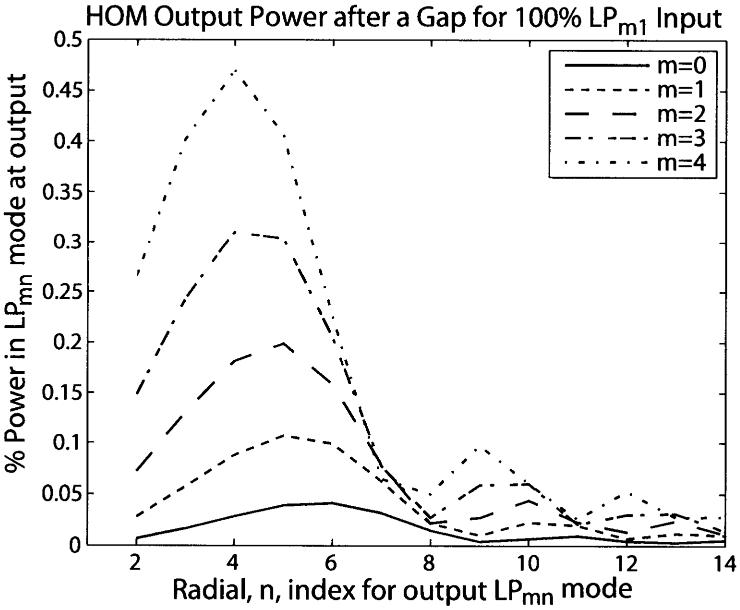

Figure 3-4: The percent output of the power present in the LP_{mn} modes after a gap that results from a 100% LP_{m1} mode input, for $m = 0$ through $m = 4$. LP_{m1} mode power outputs (which are over 94%) have been cropped to show higher order mode content.

illustrated for the case of LP_{m1} modes in Figure 3-4. Figure 3-4 shows the LP_{mn} mode content in the receiving guide due to a single LP_{m1} mode radiating from the transmitting guide through a gap of length $L = 2a$ and a system operating at 170 GHz with $a = 31.75$ mm. Results are shown for cases with $m = 0$ through 4. In these cases, over 94% of the power couples to the original input mode, less than 3% of the power is lost in the gap, and the rest of the power couples to higher order modes with the same azimuthal, m, index, as shown in the figure.

A particular input mode will only result in output modes of the same azimuthal symmetry. For example, the case of 100% HE_{11} (LP_{01} in Figure 3-4) input results in 99.48% HE_{11} after the gap and 0.26% power lost in the gap. The remaining power goes into the HE_{1n} higher order modes, with the largest percentages in HE_{16} (0.041%) and HE_{15} (0.039%), while HE_{12} is the seventh largest mode with 0.007% of the total power. Also, consider an input of 100% $\mathrm{LP}_{11}^{(o)}$, which has an output of 98.68% $\mathrm{LP}_{11}^{(o)}$, 0.67% of power lost to the gap, and the remaining power coupled into higher order $\mathrm{LP}_{1n}^{(o)}$ modes. Table 3.1 shows this single-mode input with the expected output. In each of these cases, the input power is either lost in the gap or couples into modes with the same azimuthal symmetry as the original input mode.

3.2.2 Multiple Mode Inputs

In the previous section, we considered a single mode at the input port of the gap. In this section, we consider a multiple mode input. In this case, we must consider both the amplitudes of the modes and their phases. A multiple mode input follows the same procedure as a single mode input. The gap loss is calculated using (3.9), where the input electric field is now defined as a summation of modes,

$$E_i(r,\phi) = \sum_m \sum_n \sqrt{A_{mn}} e^{j\theta_{mn}} u_{mn}(r,\phi), \tag{3.17}$$

where A_{mn} and θ_{mn} indicate the relative power and phase of the input LP_{mn} modes. The output can also be expressed as a summation of each individual mode applied to

Table 3.1: Mode content before and after a gap. (For HE_{1n} and LP_{1n}, $n > 1$)

Mode Input (%)	Modes After Gap (% content)					Gap	Other
$\mathrm{HE}_{11}/\mathrm{LP}_{11}^{(o)}$	HE_{11}	$\mathrm{LP}_{11}^{(o)}$	HE_{1n}	LP_{1n}	Other	Loss	Loss
100/0	99.48	0	0.22	0	0	0.26	0.04
0/100	0	98.68	0	0.58	0	0.67	0.07
90/10	89.53	9.87	0.20	0.06	0	0.30	0.04

equation (3.9) (as was done for equation (3.14) in the previous section),

$$\vec{E}_g^{\perp}(r, \phi, L) = \sum_m \sum_n \sqrt{A_{mn}} e^{j\theta_{mn}} \vec{E}_{g,mn}^{\perp}(r, \phi, L). \tag{3.18}$$

The electric field in a gap for a multiple mode input is simply the summation of the electric field in a gap due to each individual mode input.

After summing, the modal powers in the waveguide after the gap are calculated in the same way as the single mode case. The contribution into a specific mode must be calculated by considering the effects of all of the modes as they transverse the gap. For example, the loss in the fundamental mode due to an arbitrary multi-mode input is

$$\text{Loss in } \mathrm{LP}_{01} = A_{01} - \sum_n \sum_m \int_0^a \int_0^{2\pi} E_{g,mn} u_{01} dr d\phi \tag{3.19}$$

In this case, it's easy to note that only modes with the same azimuthal (m) index will be able to couple into each other after the gap. All other modes will result in a coupling integral of zero. Table 3.1 shows this concept. The losses for a pure HE_{11} mode input and a pure $\mathrm{LP}_{11}^{(o)}$ are shown next to the losses for a two-mode input. It's clear that the percentages of higher order mode content after the gap are only dependent on the modes with the same azimuthal symmetry. Considering a 90% HE_{11} mode, the expected output percentage is $(99.48 \times 0.9)\% = 89.53\%$. The same holds for a 10% $\mathrm{LP}_{11}^{(o)}$ mode, with an expected output percentage of $(98.68 \times 0.1)\% = 9.87\%$. However, the numbers that appear in Table 3.1 were calculated using the fresnel diffraction equations derived above; showing that the intuition for this problem is correct.

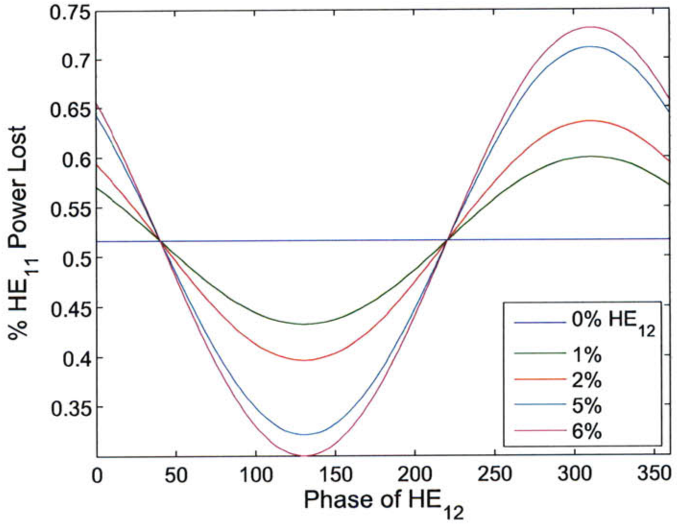

Figure 3-5: The power lost in the HE_{11} mode versus the phase difference between the two input modes. The system considers a two-mode input of HE_{11} and HE_{12}, L = 63.5 mm, and 170 Ghz. Maximum loss is at 310° and minimum loss occurs at 130°.

Alternatively, if two azimuthally symmetric modes are chosen as an input, the HE_{11} mode can see a variation in the loss seen after the gap. The phase difference between certain 2-mode input mode combinations causes variations in the power loss and mode content after the gap. The output HE_{11} power due to an input consisting of the HE_{11} and HE_{12} modes has a significant dependence on input phase, as shown in Figure 3-5. Figures 3-6, 3-7, and 3-8 show the same plot for a secondary mode of HE_{13}, HE_{14}, and HE_{15}, respectively. In these plots, it's easy to see the same effect to varying degrees.

Figure 3.2.2(a) shows the loss in the fundamental mode for gaps when $L = 2a$ and a two-mode input. The loss is shown versus the percentage of higher order mode present at the input. In this figure, the phase of the secondary input mode with respect to the fundamental mode is varied to show the wide range of loss that is possible. Considering an input mode content of 98% HE_{11} and 2% HE_{12}, the power lost in HE_{11} ranges from 0.28% to 0.75% , corresponding to respective phase differences of 310° and 130°. The average loss in HE_{11} is 0.52% (0.022 dB), the same value of loss as when HE_{11} is considered individually.

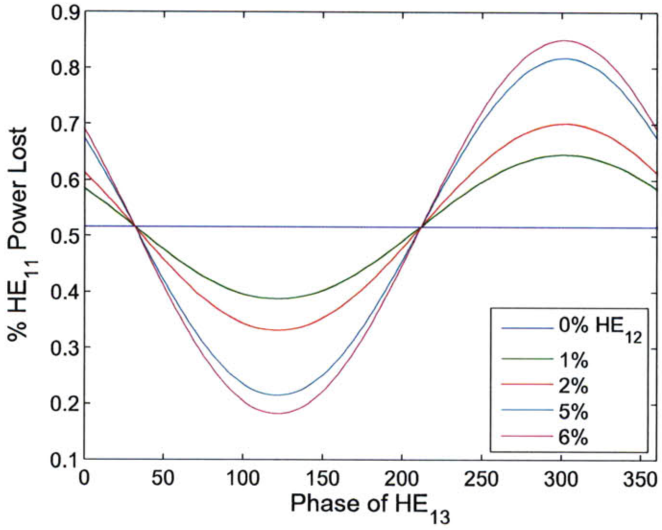

Figure 3-6: The power lost in the HE_{11} mode versus the phase difference between the two input modes. The system considers a two-mode input of HE_{11} and HE_{13}, L = 63.5 mm, and 170 Ghz. Maximum loss is at 300° and minimum loss occurs at 120°.

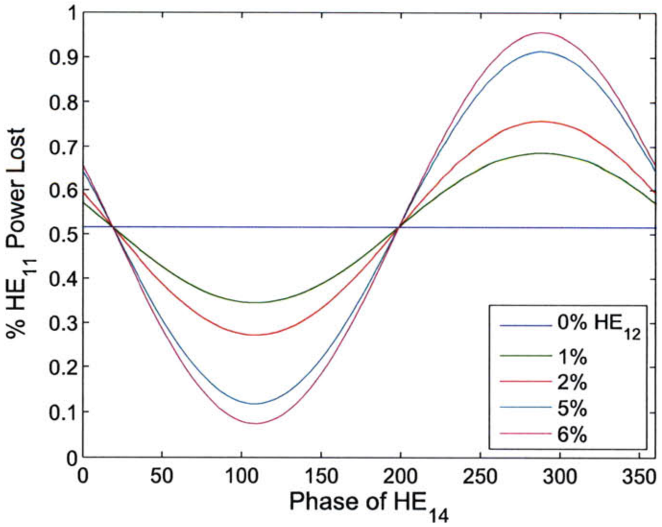

Figure 3-7: The power lost in the HE_{11} mode versus the phase difference between the two input modes. The system considers a two-mode input of HE_{11} and HE_{14}, L = 63.5 mm, and 170 Ghz. Maximum loss is at 288° and minimum loss occurs at 108°.

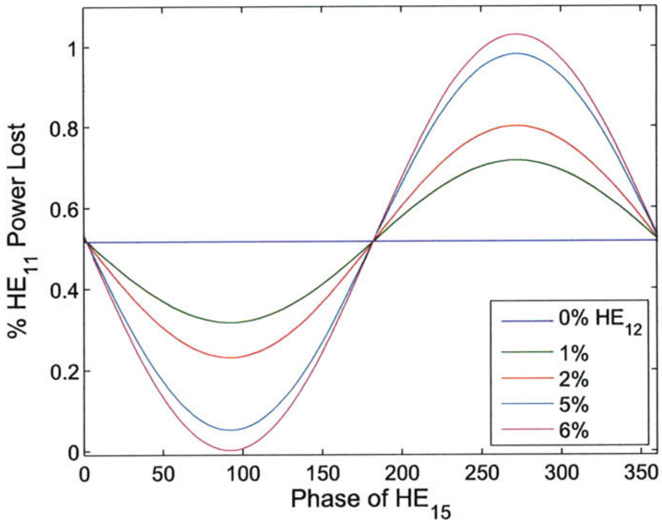

Figure 3-8: The power lost in the HE$_{11}$ mode versus the phase difference between the two input modes. The system considers a two-mode input of HE$_{11}$ and HE$_{15}$, L = 63.5 mm, and 170 Ghz. Maximum loss is at 272° and minimum loss occurs at 92°.

The dependence of power loss in a two mode system on the phase difference between the modes is seen in any combination of modes that has the same azimuthal (m) symmetry. For example, an input consisting of HE$_{11}$ and HE$_{13}$ will also have an output dependent on the phase between the two modes. This effect is seen in Figure 3.2.2(b). Though, the average loss in HE$_{11}$ is still 0.52%, with a 2% HE$_{13}$ content it may swing from 0.15% to 0.88%, depending on the input phase. This example treats modes of the same azimuthal symmetry (same m value). At the output port, a mode couples only to modes of the same azimuthal symmetry. Therefore, two modes of different azimuthal symmetry (different m values) will not interfere. For example, a two mode input consisting of an HE$_{11}$ (LP$_{01}$) mode ($m = 0$) and LP$_{11}^{(o)}$ mode ($m = 1$) produces an output that has no dependence on the relative phase of the modes and will always result in a 0.52% loss in the HE$_{11}$ mode power.

A three or more mode input of the same azimuthal (m) symmetry will also result in a phase dependence. For example, an input consisting of HE$_{11}$, HE$_{12}$, and HE$_{13}$, will result in an output dependent on the phase relations between the modes. Results for varying values of HOM percentage and phases are shown in Figure 3-10, where the $\hat{x}$-

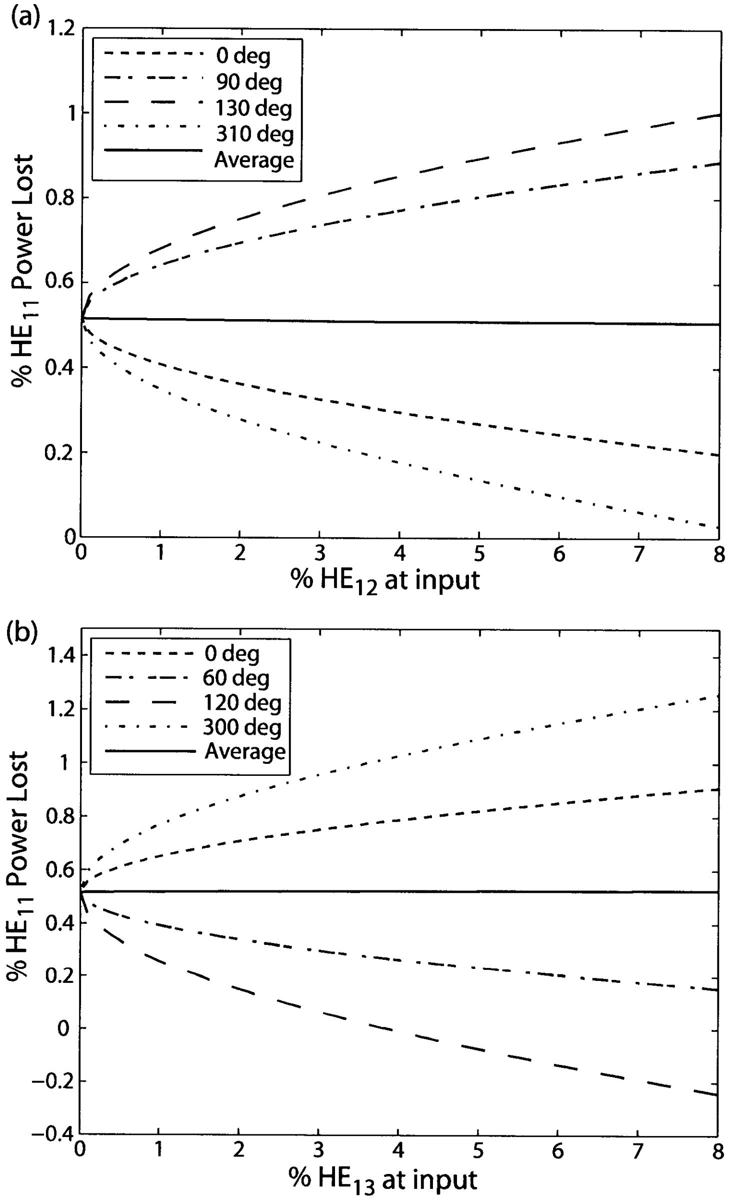

Figure 3-9: For a two mode input at 170 GHz with $a = 31.75$ mm and $L = 2a$, the percent of (a) HE_{12} or (b) HE_{13} present in the input mode mixture vs. the percent loss in HE_{11} after the gap is plotted. Different phases of HE_{12} or HE_{13} have been chosen to show the full range of swing in the HE_{11} power loss. The average HE_{11} power loss is 0.52% for both cases.

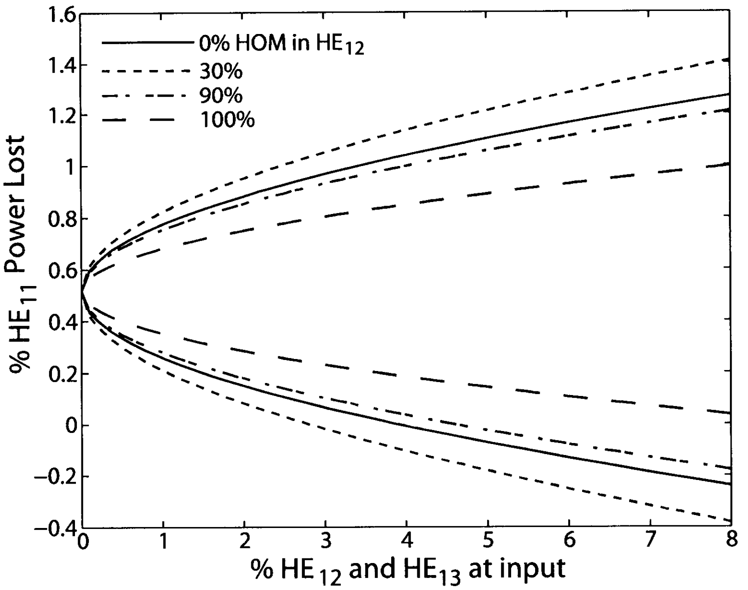

Figure 3-10: The power loss in a gap for HE_{11} vs. HOM content for a three mode input. The HOM content is split between HE_{12} and HE_{13}, and the largest and smallest HE_{11} power loss (due to HOM phase) is plotted for each mode split. The system is at 170 GHz with $a = 31.75$ mm.

axis represents the total power in the combination of the HE_{12} and HE_{13} modes. The HE_{11} power loss is dependent on the phases of both modes as well as the percentage of power in each mode. A phase difference between HE_{11} and HE_{12} of 310° and HE_{13} of 120° causes the lowest possible power loss in HE_{11}, while phases of 130° and 300° in HE_{12} and HE_{13}, respectively, cause the largest possible power loss. Figure 3-10 shows the curves corresponding to these two extreme phase combinations. Both the absolute highest and lowest loss in HE_{11} power occur when 30% of the HOM content is in HE_{12}, and 70% is in HE_{13}. In this case, a 2% HOM content may cause a swing in lost HE_{11} output power from 0.08% to 0.95% a swing that is larger than the result from 2% in HE_{12} or HE_{13} individually.

3.3 Loss due to a Miter Bend

The loss due to a miter bend is split into three components: Diffraction Loss, Ohmic Loss, and Misalignment Loss. Each of these losses will be discussed in this section.

In a perfect world with infinite conductivity and parts manufactured with zero tolerances, diffraction loss would be the only component of loss. However, the other two components must be considered when quantifying the loss of a practical miter bend.

The loss due to diffraction is calculated by decomposing the miter bend into a 2-dimensional system. Figure 3-11 shows this decomposition as described in [23] for the fundamental mode in smooth-wall circular waveguides. The theory presented here abstracts a miter bend into a theoretical four-port system, as shown in Figure 3-11(b). The system is mathematically equivalent to the miter bend and described in detail in [23] for a smooth-wall waveguide (though the same logic holds for a corrugated waveguide). For the four port system, the transmission through the bend, seen at Output 1 is due to two input powers. These two components are decomposed in Figure 3-11(c). The wave seen at Output 1 due to Input 2 is the amount of power able to transverse a gap-like structure, where half of the gap is still surrounded by waveguide. Output 1 due to Input 1 is shown as half of the radiated field as Input 1 travels through a gap of the same geometry. The component of Output 1 due to Input 1 is small and most of the power will couple to very high order modes that do not propagate, therefore this contribution can be ignored. The first component of Output 1 can be further abstracted. Since half of the gap-like structure is covered, it is sufficient to say that the power lost in a gap of equivalent geometry, shown in Figure 3-11(d), is equal to twice the power lost in the miter bend due to diffraction. This is the basis of Gap Theory, discussed at length in [13] for a pure fundamental mode in a corrugated waveguide. That is: the power lost in a 90° miter bend due to diffraction is equal to half of the power lost in a gap when the length of the gap is equal to the diameter of the waveguide, $L = 2a$. Therefore, the calculated diffraction loss in a miter bend has already been discussed in the previous section.

Since diffraction loss is defined as the loss associated with mode conversion due to the diffraction caused by an angular reflection, the diffraction loss can be estimated based on Gap Theory for any angular diffraction. For a pure fundamental HE_{11} mode,

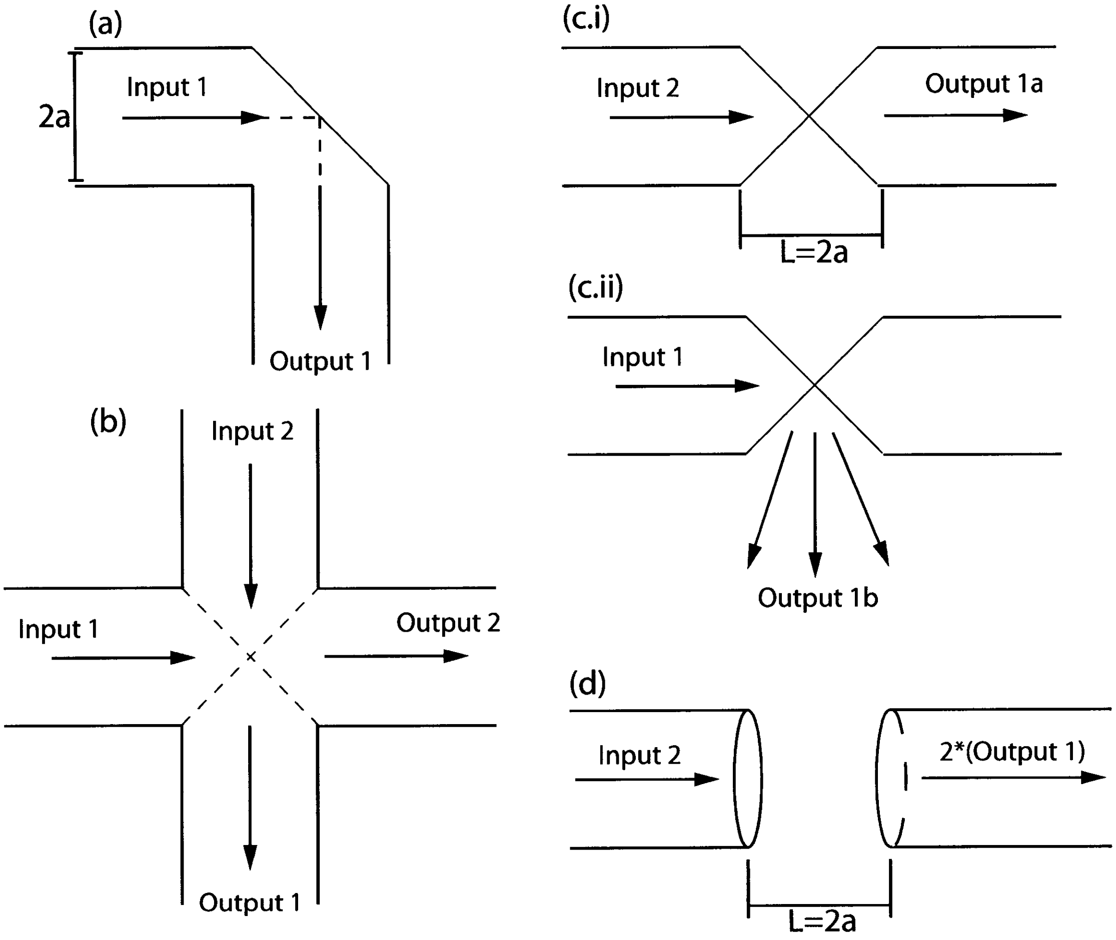

Figure 3-11: (a) A radially symmetric gap with length $L = 2a$. (b) A miter bend with a radius of a that can be modeled using equivalent gap theory, as described in the text.

diffraction loss is estimated as

$$\text{Diffraction Loss} = 0.195 \left(\frac{\lambda}{a \sin\theta}\right)^{3/2}, \tag{3.20}$$

where θ is the angle of the reflection [34]. For a 90° miter bend, $\theta = \pi/2$ and $\sin\theta = 1$. For 170 GHz and 63.5 mm diameter waveguide, Diffraction Loss in a miter bend for a pure HE_{11} mode is about 0.25%. In the previous section, the loss of the equivalent miter bend was found to be 0.022 dB for a pure HE_{11} mode, this translates via gap theory to 0.011 dB or 0.25% loss per bend.

Ohmic loss caused by reflection and seen in a miter bend is due to the heating of a material with a surface resistance, R_s, used as the optical mirror in the miter bend. This loss is estimated as

$$\text{Ohmic Loss} = 1.2\frac{4R_s}{Z_0}\cos\alpha \tag{3.21}$$

for an H-Plane bend, or

$$\text{Ohmic Loss} = 1.2\frac{4R_s}{Z_0}\frac{1}{\cos\alpha} \tag{3.22}$$

for an E-Plane bend [34]. For the Ohmic Loss considered in this application, $R_s = 2.6 \times 10^{-7}\sqrt{f(Hz)}\Omega = 0.107\ \Omega$ for pure copper at 170 GHz, the impedance of the transmission line is equivalent to the impedance of free space $Z_0 = 377\ \Omega$, and the angle of reflection off of the mirror in a miter bend is $\alpha = 45°$. Therefore, the estimated Ohmic loss in a miter bend is 0.10% and 0.19% for an H-Plane and an E-Plane bend respectively.

Misalignment loss is due to manufacturing errors in a miter bend. In general, a typical machining tolerance for an abrubt change in radius or axial offset in the waveguide will result in insignificant losses [34]. However, an angular misalignment of the mirror in a miter bend can lead to large quantities of mode conversion for overmoded waveguides. The loss due to mirror tilt is estimated as

$$\text{Misalignment Loss} = 4.26\left(\frac{a\theta}{\lambda}\right)^2 \tag{3.23}$$

where θ is the angle of tilt of the beam as it enters the output of the waveguide [34]. A 0.05° mirror misalignment corresponds to $\theta = 0.1°$ and a Misalignment Loss of 0.42%. Alternatively, $\theta = 0.05°$ gives a misalignment loss of 0.105%. A reasonable estimate for the average misalignment loss is 0.21% (for $\theta = 0.07°$), given the high precision of accuracy required in the manufactured parts with tolerances less than $\theta = 0.1°$.

Combining all three losses (diffraction, ohmic and misalignment), the theoretical loss in a miter bend for the fundamental mode is expected to be about 0.61% or 0.027 dB. Though, this estimate only considers pure mode inputs, it also considers a loss due to manufacturing errors and ohmic heating. Other modes present in the system will change the diffraction loss seen for the fundamental mode in individual bends, but in large systems (i.e. in ITER, with 7 miter bends in each of 20 transmission lines) the effects of the multimode interactions should average to zero. However, small systems (like a low-power experimental test) will be susceptible to the uncertainty in diffraction loss for the fundamental mode due to the phase dependence of the diffraction loss on HOM phase.

Chapter 4

Low-Power S-Parameter Analysis for Overmoded Components

In general, the loss of overmoded components is extremely small, on the order of 0.5%, and comparable to typical errors that result using simple measurement techniques. Even a small amount of higher order mode content in the system has the ability to skew the fundamental mode loss in overmoded components by a significant amount. Therefore, experimental measurements of loss in overmoded components should be equivalently skewed by higher order mode content in the system. However, we can account for the effect of higher order modes when appropriate baseline loss measurements and data analysis procedures are implemented, beginning with the S-Parameter Response (SPR) method presented in this Chapter and implemented in Chapter 5.

Previous low-power measurements have attempted to measure the loss in overmoded components. Other studies at MIT found the loss in an overmoded ITER-specified miter bend to be 0.05 ±0.02 dB [18]. Compared to the 0.027 dB theoretical loss for a miter bend, this measurement is acceptable, but not ideal. These loss measurements were preformed with a fundamental rectangular guide 2-port Vector Network Analyzer, VNA, by directly measuring the transmission through a 2 miter bend system with 3 meters of waveguide spaced between components and mode converters. The error in the measurement is due to the uncertainties in the calibration measurement, the sensitivity of the VNA's millimeter wave heads and connecting cables to movement, and the reproducibility of the measurement. The effects of higher order modes were not considered, but about 1–2% higher order modes were present in the experimental system.

The S-Parameter Response (SPR) technique presented in this chapter is general and will be shown to be robust and accurate for experimental measurements of the fundamental mode loss in individual components. The technique accounts for the sensitivity of the measuring equipment to movement, sensitivity of the calibration technique, reproducibility, and effect of the higher order mode content by implementing a series of S-parameter measurements to determine a baseline response of the system and the S-parameters for individual components.

4.1 S-Parameter Response (SPR)

S-Parameter Analysis is a well-established technique for measuring the transmission and reflection of passive microwave components, as described in [30]. The low-power analysis presented here, SPR, utilizes S-Parameter Analysis to consider the effect of the entire system under test in measuring the transmission loss of a particular component of the system. The SPR technique is split into 3 steps. The first step discusses the two experimental measurements that must be preformed to various Devices Under Test (DUTs). The second step discusses the analysis of those measurements to find the S matrix for the DUT, considering it as a 4-port system. The third step compares the S matrix of different DUTs to decompose the S matrix of individual components. Through these three steps, the transmission through a single component, like a miter bend, can be measured.

4.1.1 Step 1: Low-Power Measurements

The measurements described in this report use an Agilent PNA with a 140–220 GHz MMW head, transmission line components produced to ITER specs by General Atomics, and a mode converter/up-taper from WR-05 to the HE_{11} mode in 63.5 mm diameter circular waveguide. These components are depicted in Figure 4-1, where the DUT is a 3 m, 2 miter bend system. The system is also abstracted in Figure 4-2.

For the SPR technique, a one port calibration is performed on the head of the PNA, permitting a phase and amplitude measurement to be taken. The calibration plane is shown in Figure 4-2. The reflection, or S_{11}, measurement due to a matched load and a short is taken for various equipment configurations. With these two measurements, the S matrix of the up-taper and the DUT will be calculated.

For each series of measurements, a one port calibration was performed on the millimeter wave head of the PNA, which calibrates both phase and amplitude. After calibration, the cables and millimeter wave head were connected to the up-taper. The up-taper was secured to the optical table to prevent accidental movement while DUTs were connected. These components remained stationary for the duration of measurements taken with that calibration.

The millimeter wave head was connected to an up-taper, such that the miter bends will lie in the E-Plane. The 1.8 m long up-taper with a long filter attached converts a 170 GHz signal from the fundamental TE_{10} mode in rectangular WR-05 waveguide to HE_{11} in 63.5 mm diameter corrugated circular waveguide. It is rated from 169–171 GHz by the manufacturer, General Atomics. In previous analysis we have measured a 98.6±0.5% HE_{11} mode purity after the up-taper, or 1–2% higher order mode content.

The transmission line components meet ITER specifications for performance and were manufactured by General Atomics. The components available are three sections of 63.5 mm diameter corrugated circular waveguide, each 1 m long, and two miter bends. In addition, there are 1 section each of 80, 60, and 40 cm long 63.5 mm diameter corrugated circular waveguide. The waveguide sections are machined out of a single piece of aluminum with inner quarter-wavelength corrugations. The miter bends, shown in Figure 4-3 are machined out of a block of aluminum and have a copper mirror of optical quality at 45°±0.1°. Each miter bend has 42 cm of corrugated waveguide extending from each end to assist with attachment to waveguide components. General Atomics transmission line components are attached with 20 cm long

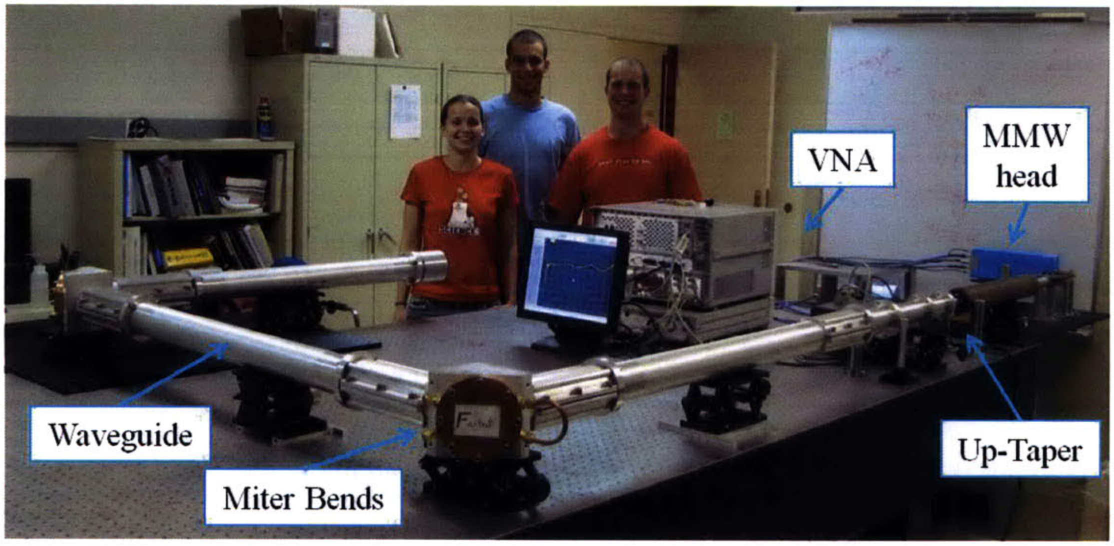

Figure 4-1: The system which was implemented during SPR analysis. The PNA was used to measure the S_{11} due to a short with a DUT consisting of 3 meters of waveguide and 2 miter bends.

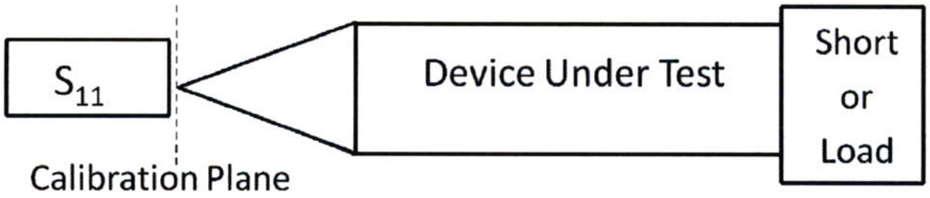

Figure 4-2: The General set-up for measurements taken. The Device Under Test (DUT) consisted of various 63.5 mm diameter components. The S_{11} system measurement accounts for the effects of the up-taper and the DUT.

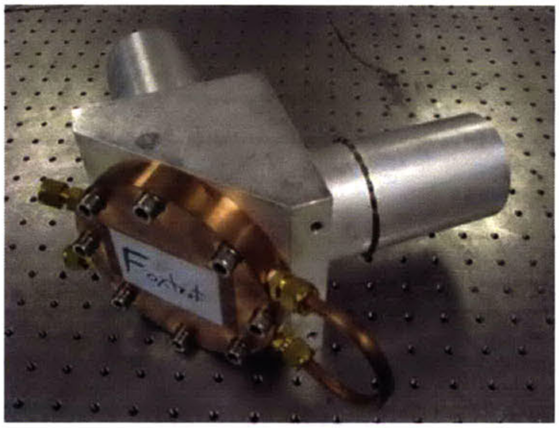

Figure 4-3: A miter bend manufactured to ITER specifications and used in low-power testing.

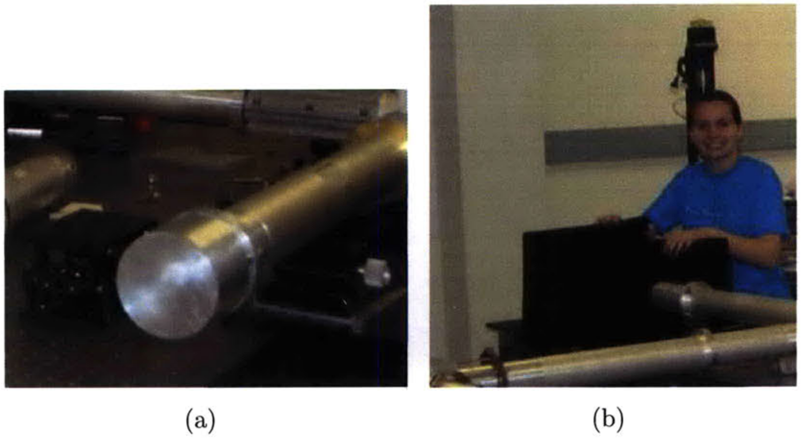
(a) (b)

Figure 4-4: Measurements were taken by applying (a) a matched load using Eccosorb and (b) a short to the end of the 63 mm diameter waveguide.

clamps that assure precision alignment with no angle and/or offset between components. Precision lab jacks are used to assure the appropriate height of all components and eliminate any issues that may result from the sagging of waveguide or undue stress between components. With these components, it is possible to achieve highly accurate alignment in a clean low-power laboratory setting, as will be evident in the reproducibility of our results in Chapter 5.

To begin, measurements were taken with the goal of calculating the transfer, or S, matrix of the entire system being measured (up-taper and 63 mm diameter waveguide components). In order to do this, two reflection, or S_{11}, measurements are taken. The first measurement is with a short at the end of the DUT, which reflects all power at the end back through the DUT and up-taper. The short is a machined piece of aluminum which fits on the end of the 63.5 mm diameter DUT, as shown in Figure 4-4(a). The S_{11} due to the short measurement can be estimated as the transmission through the DUT and up-taper with twice the loss in the system, such that $S_{12}[\text{system}] \approx \sqrt{S_{11}[\text{measured}]}$. However, in reality, reflections occur in the system. Therefore, a second measurement is taken with a matched load attached to account for the reflected power. The matched load is implemented by allowing the DUT to be unobstructed at the end of the line and placing Eccosorb to prevent extraneous reflections from the test area, as shown in Figure 4-4(b). The matched

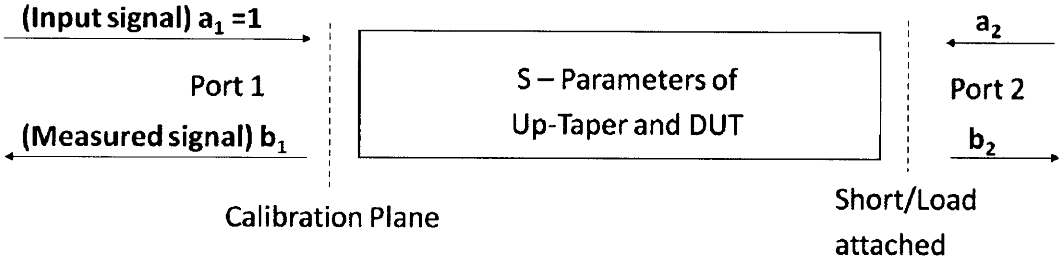

Figure 4-5: Diagram illustrating the 4 port system S-matrix and indicating the inputs and outputs of a system.

load absorbs the power in the system, therefore the S_{11} measurement due to a matched load is an indication of the reflections which occur in the system.

4.1.2 Step 2: S-Matrix Calculation

To analyze the data from an individual set-up, the intrinsic S_{11} and S_{12} of that set-up (including the up-taper and all 63.5 mm transmission line components) can be calculated. The 4-port system is illustrated in Figure 4-5. It estimates no conversion between modes of the system, however we will deal with that error when considering the baseline measurement in Step 3.

In general, for a 4-port system the ports are related through the S-matrix by

$$\bar{b} = \bar{\bar{S}}\bar{a}, \tag{4.1}$$

where

$$\bar{\bar{S}} = \begin{bmatrix} S_{11} & S_{12} \\ S_{21} & S_{22} \end{bmatrix}. \tag{4.2}$$

Since the components in this system are passive, we estimate this as a reciprocal system, such that

$$\bar{\bar{S}} = \begin{bmatrix} S_{11} & S_{12} \\ S_{12} & S_{11} \end{bmatrix} \tag{4.3}$$

and equation (4.1) decomposes into

$$b_1 = a_1 S_{11} + a_2 S_{12}, \tag{4.4}$$

and

$$b_2 = a_1 S_{12} + a_2 S_{11}. \tag{4.5}$$

For further details on S-parameters see [30].

In Figure 4-5, a_1, b_1 and a_2 can be defined for both the short and load measurement. In each measurement a_1 is calibrated to be 1, and b_1 is the S_{11} that has been measured due to the short or load attached, now referred to as b_{1S} and b_{1L}, respectively, in order to avoid confusion. For the short, $a_2 = b_2$. Whereas, for the load $a_2 = 0$ and b_2 remains unknown. Using these assigned values, S_{11} of the system is found via equation 4.4 considering a matched load input, such that

$$S_{11}[\text{system}] = b_{1L}. \tag{4.6}$$

Knowing S_{11} of the system, S_{12} of the system can be found via equation 4.5 and the short measurement,

$$S_{12}[\text{system}] = \sqrt{(b_{1S} - S_{11}[\text{system}])\,(1 - S_{11}[\text{system}])}. \tag{4.7}$$

Note that these calculations use a linear magnitude of the measurements, b_{1L} and b_{1S}. In the limit of $b_{1L} \approx 0$ (i.e. no reflections), $S_{11}[\text{system}] \approx 0$ and $S_{12}[\text{system}] \approx \sqrt{b_{1S}}$, as indicated previously. However, for completeness, the effect of the matched load will be kept.

4.1.3 Step 3: S-Matrix Decomposition

Using a similar method, the S-parameters of an individual component can be found. Consider a system under test consisting of two components, as illustrated in Figure 4-6. If the S-parameters of the first component are already known (through the

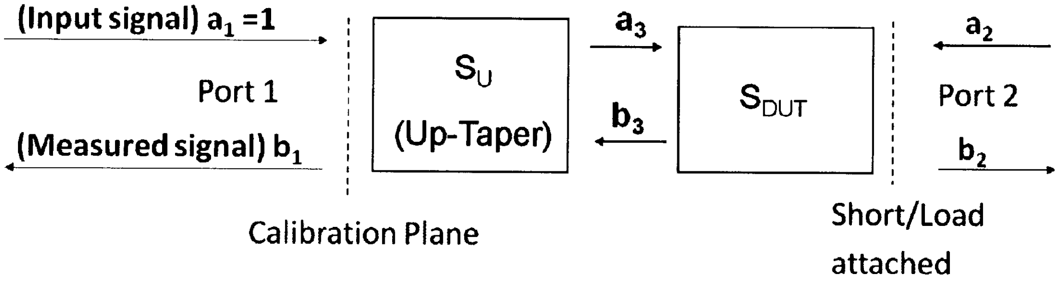

Figure 4-6: Diagram illustrating the cumulative S parameters of a two-segment system.

calculations of Step 2), the S-parameters of the second component can be calculated. For example, the S-parameters of just the up-taper, S_U, may easily be determined by the analysis presented in Step 2 when no components are attached to the up-taper (that is, the DUT is nothing).

In this system, the same short and matched load measurements have been taken as in Step 2; the same assignments can be made to a_1, b_1, and a_2 for these measurements. In the case that follows, only the matched load measurement has been considered, for simplicity. For a reciprocal system,

$$b_1 = a_1 S_{11U} + b_3 S_{12U} \tag{4.8}$$

$$a_3 = a_1 S_{12U} + b_3 S_{11U} \tag{4.9}$$

$$b_3 = a_3 S_{11DUT} + a_2 S_{12DUT} \tag{4.10}$$

$$b_2 = a_3 S_{12DUT} + a_2 S_{11DUT} \tag{4.11}$$

Knowing S_U, this series of equations can be solved for b_3 and a_3, such that

$$b_3 = \frac{b_{1L} - S_{11U}}{S_{12U}}, \tag{4.12}$$

and

$$a_3 = S_{12U} + \frac{b_{1L} - S_{11U}}{S_{12U}} S_{11U}. \tag{4.13}$$

In addition, b_2 can also be defined using the S parameters of the entire system,

$$b_2 = S_{12}[\text{system}]a_1. \tag{4.14}$$

where $S_{12}[\text{system}]$ is found via Step 2. With these values, S_{11DUT} and S_{12DUT} are easily found through equations (4.10) and (4.11), considering that $a_2 = 0$ for a matched load,

$$S_{11DUT} = b_3/a_3, \tag{4.15}$$

$$S_{12DUT} = b_2/a_3. \tag{4.16}$$

In the limit of small reflections, $S_{11DUT} \approx 0$ and

$$S_{12DUT} \approx \frac{S_{12}[\text{system}]}{S_{12U}}. \tag{4.17}$$

This is a logical approximation and will produce accurate results. However, since the problem at hand requires high accuracy, we will use the full calculation for our data analysis.

4.2 Experimental Configuration

The SPR technique was used to design our experiment. For example, consider a simple system consisting of an up-taper and a 1 m length section of 63.5 mm waveguide. With a previous system measurement for just the up-taper, the S-parameters for that device alone, S_{11UT} and S_{12UT}, can by found using equations (4.6) and (4.7) respectively. With those values, the S-parameters associated with the 1 m length section of waveguide can be found via equations (4.15) and (4.16). Ideally, the straight waveguide section will result in full transmission, i.e. $S_{11K} = 0$ and $S_{12K} = 1$. Any discrepancy in this measurement resulting from higher order modes will need to be accounted for in a baseline measurement, as discussed in the proceeding chapter. In general, Step 3 of SPR can be performed multiple times when dealing with large systems of components or the subtraction of a baseline measurement. This iterative process decomposes the measured values into S-parameters of the individual components in a complex system.

Chapter 5

Experimental Power Loss Measurements

Two low-power experiments were performed using the SPR method. The first experiment calculated the loss due to a miter bend with high precision. The second experiment calculated the loss due to a gap in waveguide which demonstrates the accuracy of the SPR method.

5.1 Loss Due to a Miter Bend

The loss due to a 63.5 mm diameter corrugated cylindrical miter bend was found via the SPR method discussed in Chapter 4. The measurements exhibited certain artifacts that are investigated in this section and accounted for during data analysis. There was a natural frequency dependence to the components (slow varying ripple), a strong resonant behavior due to reflections in the up-taper (rapidly varying ripple) and a DC shift with the addition of waveguide sections (mode-beating). We are interested in the average loss over the frequency of interest so measurements were taken over a 2 GHz range centered at 170 GHz and the final loss value is reported as the average of the band from 169.5–170.5 GHz in order to account for the effect of the slowly varying ripple. The rapidly varying ripple does not affect this loss, and was filtered out during FFT processing. However, the DC shift due to mode-beating with the addition of waveguide was accounted for in the SPR processing of data as it produced a noticeable shift in the signal that was not a result of loss in a miter bend.

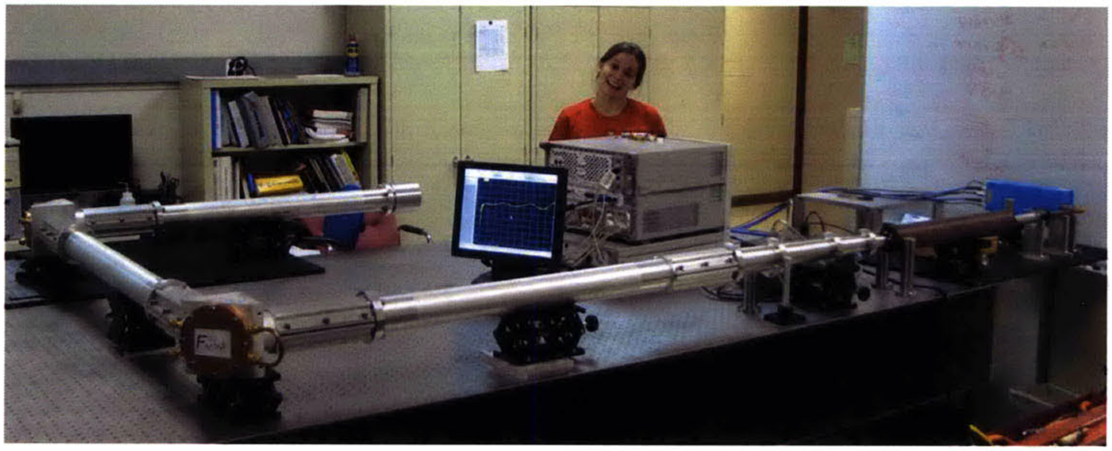

Figure 5-1: Photo of the experimental set-up for measuring the loss in a miter bend. The set-up uses three 1-m sections of straight waveguide and 2 miter bends.

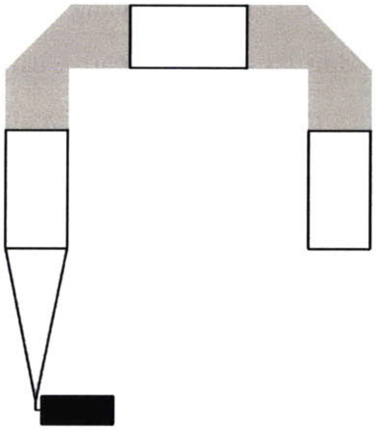

Figure 5-2: Diagram of 2 miter bends and 3 m of waveguide under test. The experimental set-up of this diagram is shown in Figure 5-1.

The uncertainty all corrections, particularly the mode-beating correction, is included in the error of our measurement. These processes are discussed in detail below.

5.1.1 Experimental Design

To measure the loss in a miter bend, the experimental system consisted of 3 1-m length sections of waveguide and 2 miter bends. The experimental set-up is shown in Figure 4-1 and a diagram depicting the DUT is shown in Figure 5-2.

The S matrix for the entire system can be calculated, S_{SYS}. With a previous measurement considering just the up-taper, the S matrix for an up-taper is also known,

S_{up}. In addition, the transmission through 3 m of waveguide can also be found using SPR, S_{3m}. For reference, an experimental set-up 4 m of straight waveguide is shown in Figure 5-3. The theoretical loss in a straight section of 63.5 mm diameter corrugated waveguide is 1.56×10^{-4} dB/m (or 0.18×10^{-4} Np/m) for the HE_{11} mode and less than 0.001 dB/m for all modes of interest [31]. This loss is too low to be accurately measured, even using the improved SPR technique. Therefore, if there is only a single mode in the system, there should be zero reflection and full transmission through the component (an identity S-matrix). However, if there are higher order modes in the system, the S matrix of the 3 m of waveguide is not measured as ideal due to the coupling of the higher order modes through the mode-converter for measurement. This effect of higher order modes on the detected transmission through straight sections of waveguide means that the S-matrix of the straight sections of waveguide is not the identity matrix and must be taken into account as the baseline measurement for the original system considered. Since the system can be approximated as reciprocal and contains only passive components, the S-matrices of individual components can be combined and rearranged, such that $S_{SYS} = S_{up} \times S_{3m} \times S_{2miter}$.

Therefore, the S matrix of 2 miter bends, S_{2miter}, may be calculated via the SPR method. First, the effect of the up-taper will be taken care of, such that in Step 3 $S_U = S_{up}$ and $S_{DUT} = S_{3m} \times S_{2miter}$. Next, the effect of the baseline will be taken care of, such that in Step 3 $S_U = S_{3m}$ and $S_{DUT} = S_{2miter}$. Since S_{2miter} accounts for the loss of two miter bends, to find the loss in an individual miter bend,

$$\text{Loss per Bend} = \frac{1 - S_{12,2miter}}{2} \tag{5.1}$$

In addition, the reproducibility error (in dB) for $S_{12,2miter}$ is also divided by 2 because there were two miter bends in the system. Therefore, it is beneficial to measure the loss due to two miter bends as opposed to just a single miter bend because the error bar reduces significantly for the measurements that used 2 miter bends in the experimental set-up.

With this process in mind, two series of measurements are taken for any loss

Figure 5-3: Photo showing 4 m of straight waveguide under test. The measurement of the loss due to straight sections of waveguide was used to calculate the baseline measurement and the uncertainty error of S_{3m}.

measurement. The first series considers the addition of different lengths of waveguide to the up-taper to determine the trend of the baseline measurement. This process is necessary to quantify the baseline measurement, S_{3m} as well as the error associated with that measurement. The second series utilizes the set-up in Figure 5-1 and is used to determine the S_{12} of 2 miter bends. With these measurements, the loss due to a single miter bend was determined.

5.1.2 FFT processing

The processing of measurements required limiting the range of frequencies used by applying a low pass filter to the data. S_{11} measurements for the short and matched load were taken over a range of frequencies from 169–171 GHz. After processing, only the range from 169.5–170.5 GHz was considered, as seen in Figure 5-4(a) which shows the short measurement for the up-taper. Figure 5-4(b) shows the FFT of the same measurement, as well as the filter that was applied to preserve the DC and slowly varying ripple (this effect is an inherent property of the system). There is a peak in the FFT that corresponds to a reflection distance of 1.8 m, which is also the length of the up-taper. Considering the sensitivity of the small rectangular fundamental WR-05 waveguide, it is reasonable to assume that a reflection occurs close to the millimeter-wave head. Knowing the cause of this reflection, the FFT filter may be applied without altering the results of the measurement.

Alternatively, averaging could be performed when taking the S_{11} measurements from the PNA. However, the FFT filter offers a higher level of accuracy for the high frequency filter and does not obscure the low frequency components of the signal.

Figure 5-5 displays the same FFT for measurements with the short connected to the up-taper, as well as the short connected to the up-taper with 1, 2, and 3 m of waveguide attached. In each FFT, it is seen that the peak which corresponds to the rapidly varying ripple occurs at a distance equivalent to the length of the system under test. For example, the peak in the FFT for the up-taper and 3 m of waveguide occurs at 4.8 m. Since the rapidly varying ripple was caused by the up-taper and was an intrinsic component to the set-up of the experiment, a low pass filter is applied

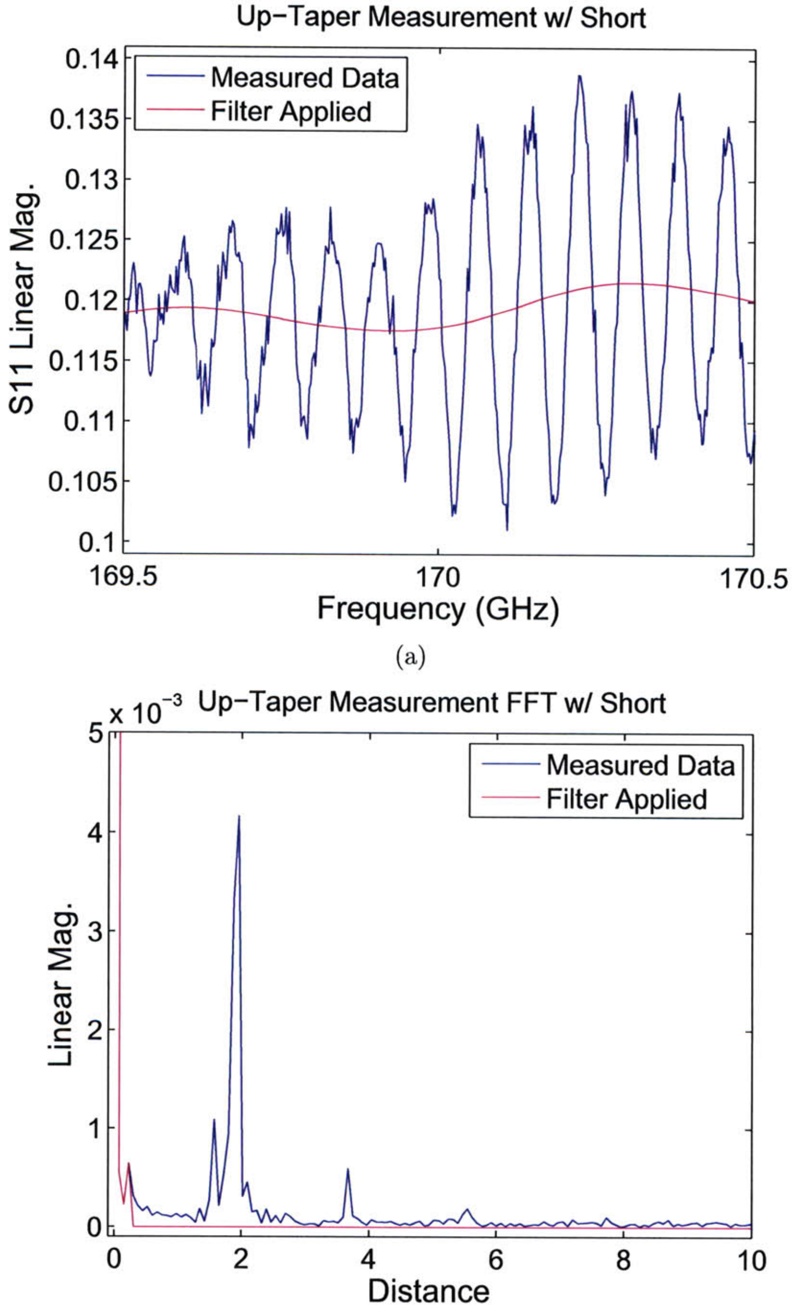

(a)

(b)

Figure 5-4: (a)The FFT for the measured data for just the up-taper (0 m of waveguide) with the short applied, indicating the filter (in pink) that has been applied, and (b) the corresponding magnitude vs. frequency plot of the same data before and after the filter.

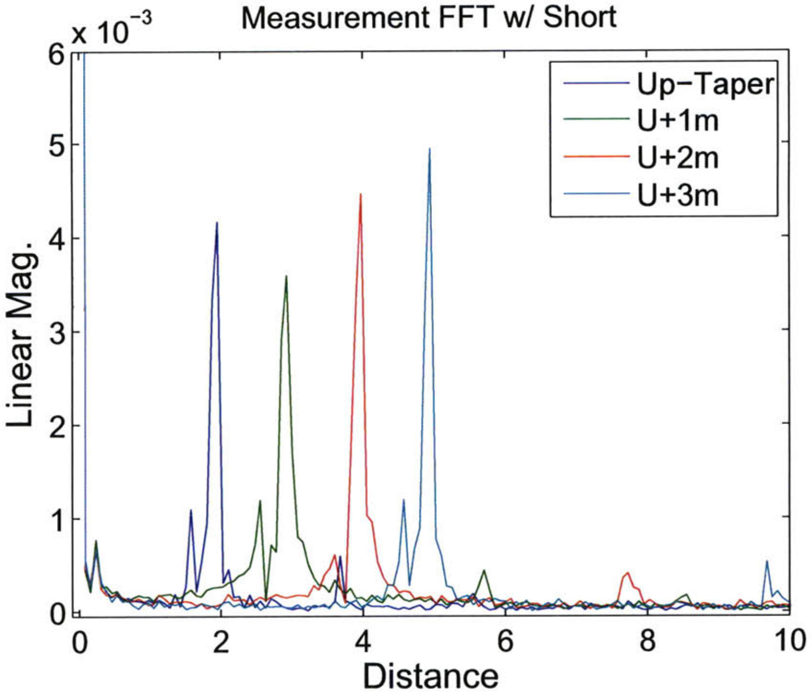

Figure 5-5: The FFT of the calculated S_{12} for 0-3 m sections of waveguide. The x-axis has been scaled to indicate the length between the reflecting components.

to all of the measurements. This filter preserves the DC signal as well as a slowly varying ripple.

For the next steps, the data was processed over the entire range of frequencies in order to preserve accuracy. However, for the singular values of S_{12} and S_{11} reported at 170 GHz, the final calculation was averaged from 169.5-170.5 GHz. (Data and FFT calculations were taken over 169–171 GHz to eliminate some data processing effects in the final 1 GHz bandwidth.) The standard deviation of the data over the 1 GHz bandwidth was taken into account in the error of the measurement, but was small when compared with other errors.

5.1.3 Baseline Measurement

In the first series, measurements were taken using 0–4 m of straight waveguide (in 20 cm increments) after the up-taper. Knowing the S-matrix of the up-taper, S_{up}, the S-parameters of just the straight sections of waveguide are calculated. Only the S-matrix

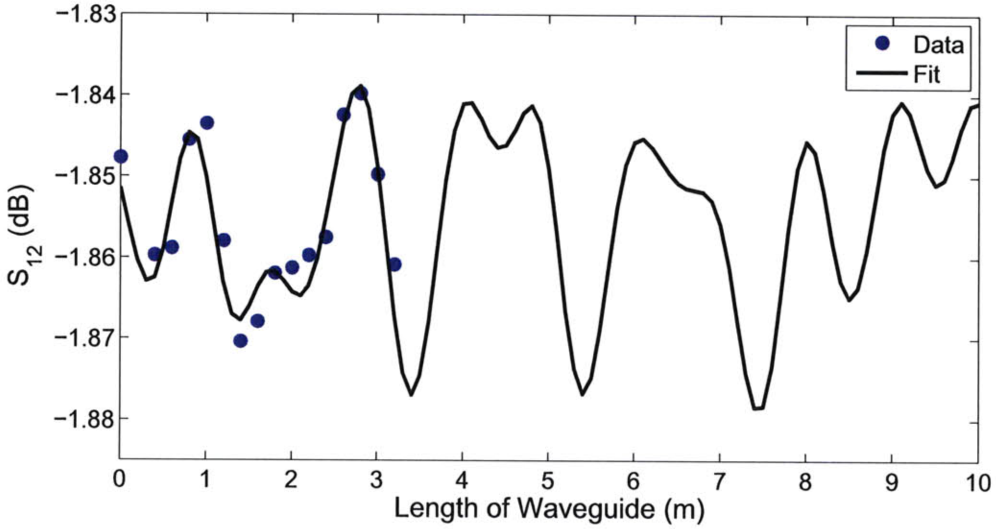

Figure 5-6: The transmission measured for the up-taper and straight sections of waveguide from 0–3m. The fit curve is a possible combinations of modes that has been extended beyond measurements to show the periodicity of the transmission with length of waveguide attached. The -1.86 dB offset is due to the efficiency of the mode converter/up-taper; the ripple around -1.86 dB is due to higher order modes in the system.

of the 3 m section, S_{3m}, is used to calculate the loss in a miter bend. However, the S-parameters of the other straight sections must be calculated in order to determine the level of uncertainty in the S_{3m} baseline measurement. The S-parameters of all straight sections are used to determine a component of the error due to the final calculation of the loss in a miter bend. Ideally, the transmission through straight sections of waveguide is close to $S_{12} = 0$ dB (or full transmission) [31]. However, due to our method of measurement, the transmission measured through straight sections of waveguide will be dependent on the mode content of the signal.

The measured S_{12} (including up-taper and straight sections) is averaged over 169.5–170.5 GHz and is reported in Figure 5-6 for two different days of experiments. A slight variation is seen in the S_{12} values that can be attributed to higher order modes in the overmoded waveguide. If the system were ideal and transmitting in pure HE_{11} through the overmoded waveguide sections, adding a meter length of waveguide would not change the S_{12} of the system. However, it is likely that the slight content of higher order modes cause this variation in our measurements.

Mode	X_{mn}	Δk (1/m)	λ_B (m)	% Content
LP_{01}	2.405	—	—	99.45%
LP_{11}	3.832	1.24	5.07	0.10%
LP_{21}	5.136	2.87	2.19	0.11%
LP_{02}	5.520	3.44	1.83	0.17%
LP_{31}	6.380	4.87	1.30	0.04%
LP_{12}	7.016	6.06	1.04	0.12%
LP_{22}	8.417	9.08	0.70	0.01%

Table 5.1: A possible mode content for the observed mode-beating in Figure 5-6.

Utilizing the theory discussed in Section 3.1, the curve was fit with a combination of the mode beating due to HE_{11} with the 5 lowest order modes of the system, as shown in equation (3.7). The curve seen in Figure 5-6 was generated by considering 0.55% higher order mode conent in the system alongside the HE_{11} mode, the breakdown of the particular mode content in the Figure is shown in Table 5.1. This table emphasises the Δk and beat wavelength, λ_B between the higher order modes and HE_{11}. In addition, there are oscillations between the higher order modes in smaller quantities.

By no means does Table 5.1 show the only possible combination of modes to fit the measured data well, but the periodicity of the transmission measurements corresponds well to the beat wavelengths with these combinations. In addition, the amplitude of the oscillation correlates well with any mode content considering about 0.25–1% higher order modes. Particularly, the LP_{02} (or HE_{12}) mode beating with HE_{11} corresponds to the frequency of one of the oscillations seen.

Clearly, the mode content associated with these higher order modes is small and the frequencies of oscillations are clustered from 0.5–5 m making resolution of the data difficult. More data points would be needed to generate enough data to accurately determine the mode content of the system. Unfortunately, our experimental set-up only allowed for about 3 m of straight waveguide to be under test at once. Therefore, no further conclusions can be drawn save for the fact that we have about 0.25–1% higher order modes in the system. The method is not robust enough to account for the small effects of the higher order modes after conversion to fundamental rectangular waveguide at the end of the up-taper.

Unfortunately, a calculation of the mode content based on mode beating can only

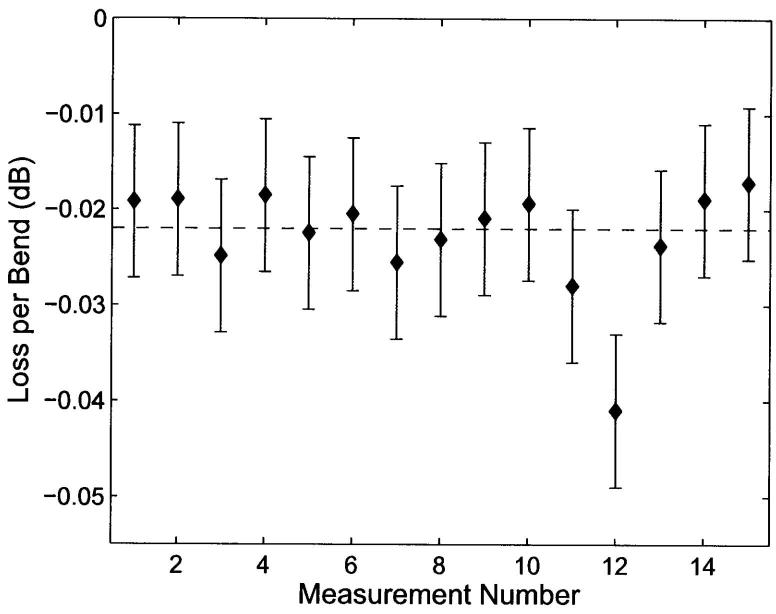

Figure 5-7: The loss in a single miter bend is found from the average S_{12} for several different measurements taken with two miter bends in the system. Different configurations were used, however there is no visible trend between types of measurements.

be considered a qualitative analysis, due to a lack of data points and the Nyquist sampling limit. Therefore, the standard deviation for the S-parameters for all straight waveguide sections was used to calculate the error due to the baseline adjustment with SPR.

5.1.4 Results

The S_{12} of a single miter bend was found from the second series of measurements. These measurements tested two miter bends with three 1-meter long sections of waveguide. In this process, the S_{12} was calculated for two miter bends using the method described previously. The averages for all measurements are shown in Figure 5-7. These results were adjusted for a single miter bend. The error bars are determined by the standard deviation of the determined values for $S_{12,2miter}$ (reproducibility error) and the standard deviation between the 0–3 m measurements, as discussed in the previous subsection. Due to the method of measurement using two miter bends, the error from the 0-3 m measurements is only half as much per bend as was calculated.

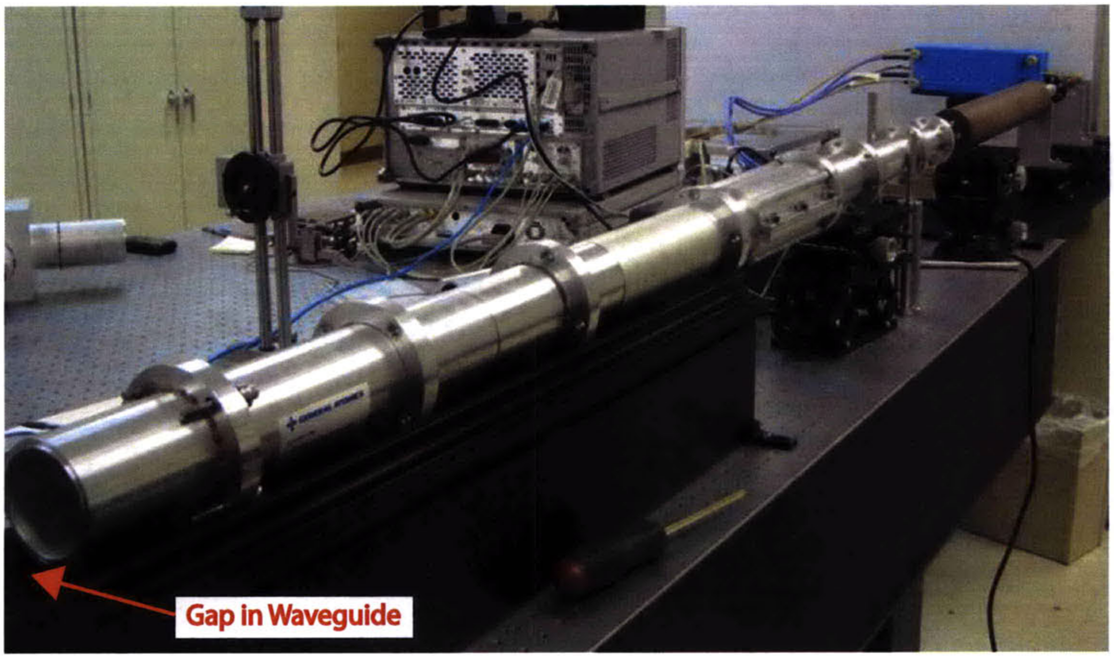

Figure 5-8: The experimental set-up to measure the loss due to a gap in waveguide. Alignment between the transmitting and receiving waveguides is achieved with a stationary optical rail which allows the waveguides to move in the $\hat{z}$-direction and the length of the gap to be easily variable.

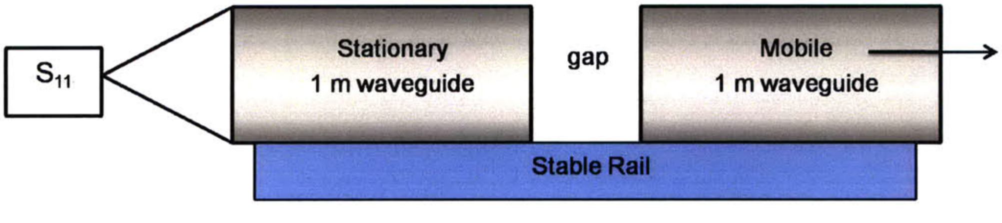

Figure 5-9: A diagram of the experimental set-up for a gap in waveguide as shown in Figure 5-8.

From these measurements and calculations, we have determined that the loss in a GA miter bend produced to ITER specifications is 0.022 ±0.008 dB, as shown in Figure 5-7. This value accounts for the error due to the reproducibility of measurements. It also accounts for the error due to the uncertainty in the transmission through straight sections of waveguide which arises with higher order modes. This value is consistent with theory, which predicts 0.027 dB loss per bend.

5.2 Loss Due to a Gap in a Waveguide

5.2.1 Experimental Set-Up

To determine the loss in a gap of waveguide, the same procedure was used. Except, the miter bends were replaced with a single gap. The experimental set-up is shown in Figure 5-8, with a diagram in Figure 5-9 for further explanation. The transmitting and receiving waveguide were kept 1 m long for simplicity of measurements, and the length of the gap was easily variable. reflections near the gap were negligible.

The S-parameter analysis was the same as for the miter bend loss measurement. For each series of gap measurements, a baseline S_{11} measurement was taken for both a short and a matched load with 2 meters of waveguide attached to the up-taper. Then, for each length of gap, an S_{11} measurement was taken for a short attached to the end of the mobile section of waveguide shown in Figure 5-9. The matched load measurement was indistinguishable from the baseline matched load measurement, so the baseline measurement for the matched load S_{11} was used for all gap lengths. This approximation was taken to eliminate errors due to misalignment when exchanging the short for a matched load at the end of the waveguide.

As was done for the miter bend loss measurement, an FFT was performed on all measured data to remove the high frequency ripple, and the data was averaged over a 1 GHz bandwidth around 170 Ghz to remove the low-frequency variations. The baseline measurement was taken for 2 meters of straight waveguide. Therefore, the measured S-matrix of the system seen in Figure 5-9 was $S_{SYS} = S_{up} \times S_{2m} \times S_{gap}$. A

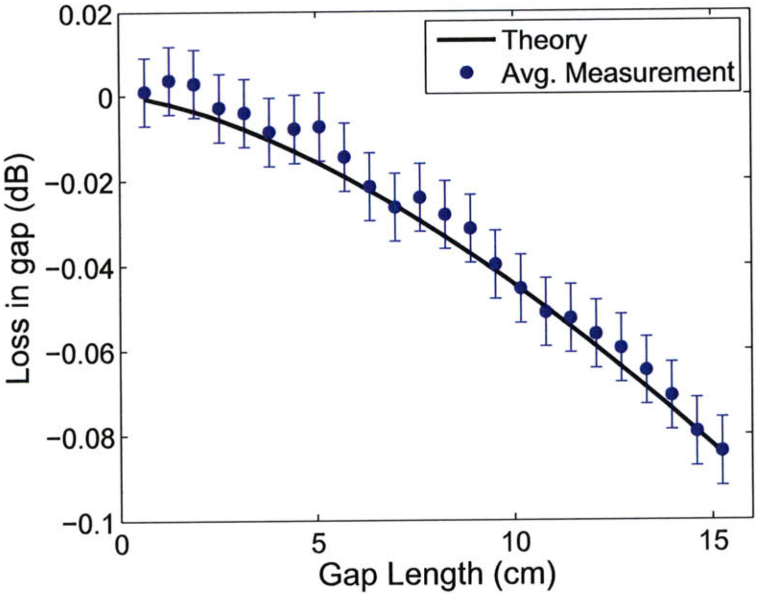

Figure 5-10: The average loss due to a gap in waveguide vs. the length of the gap under test. Error bars of 0.008 dB are shown. The theoretical loss in a gap for the fundamental mode is also shown (from Figure 3-3).

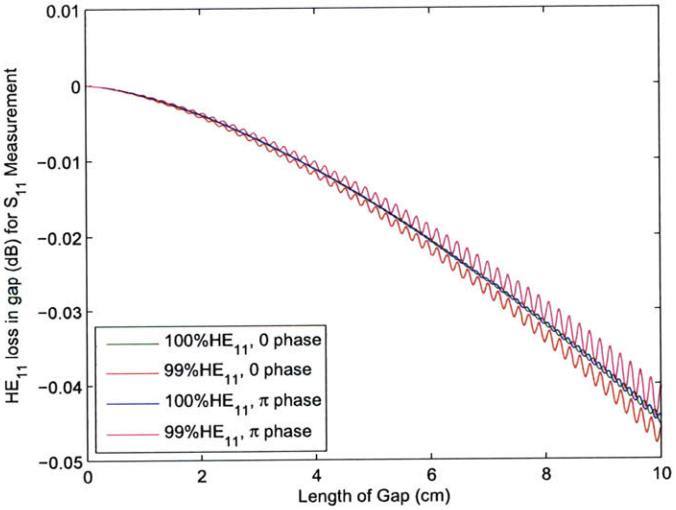

Figure 5-11: Theoretical loss in a gap for the HE_{11} mode versus length of the gap specifically calculated for the loss seen in the reflected measurement. Higher order mode content is considered in the HE_{12} mode only with a phase of 0 or π between the modes. Oscillations have a wavelength of 1.76 mm (170 Ghz).

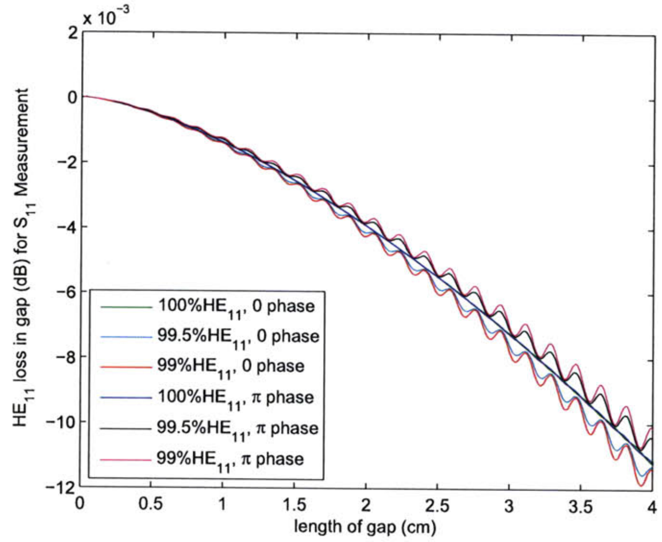

Figure 5-12: Theoretical loss in a gap for the HE_{11} mode versus length of the gap specifically calculated for the loss seen in the reflected measurement. Zoomed image of Figure 5-11 for 0–4 cm length of gap.

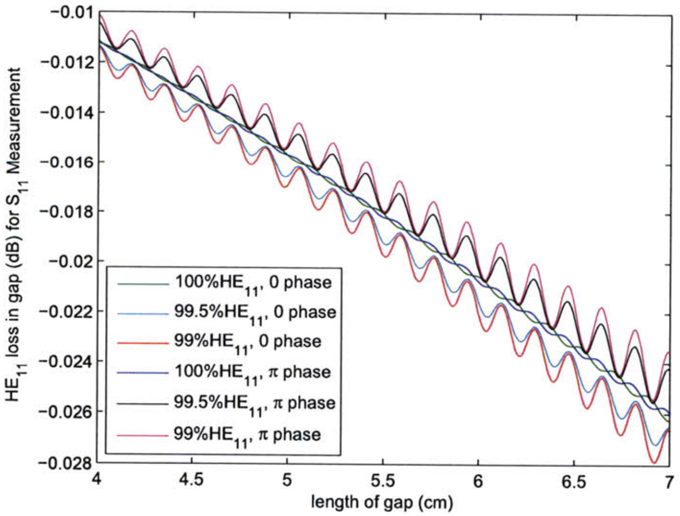

Figure 5-13: Theoretical loss in a gap for the HE_{11} mode versus length of the gap specifically calculated for the loss seen in the reflected measurement. Zoomed image of Figure 5-11 for 4–7 cm length of gap.

two-step decomposition was performed, as described in the previous section for the miter bend measurement, to determine the loss due to the gap.

5.2.2 Results

The loss due to a gap of waveguide is shown in Figure 5-10 alongside the theoretical loss for the pure HE_{11} mode. Theory and measurements are in good agreement. However, a pronounced ripple in the measured data is seen. It is suspected that higher order modes are responsible for the ripple, but the effects of higher order modes which were investigated occur with a much shorter wavelength.

Considering the theory from Chapter 3, higher order modes can alter the loss seen in a gap. In fact, just 0.5% higher order mode has the ability to significantly alter the loss seen in a gap. Since the loss is determined via a reflection, S_{11}, measurement, the phase between HE_{11} and higher order modes varies based on the length of the entire system. That is, the loss due to the gap changes between the transmitted, $+\hat{z}$, and reflected, $-\hat{z}$, traveling signals; the reflected signal phase depends on the length of the system. Therefore, a ripple occurs in the calculated loss in a gap. The amplitude of the ripple is determined by the percentage of higher order mode content and the frequency of the ripple is the frequency of the system, 170 GHz. This ripple is shown in Figures 5-11, 5-12, and 5-13 for different combinations of HE_{11} and HE_{12}.

The measured loss in a gap was determined to be accurate and in good agreement with theoretical calculations, as shown in Figure 5-14. Though the wavelength of the oscillations of the theoretical loss in a gap with higher order modes, $\lambda = 1.76$ mm, cannot be fit to the measured data, the maximum and minimum theoretical loss for 0.5% HE_{12} was determined and is shown in Figure 5-14 alongside the measured loss. The wavelength of the unaccounted for ripple is about 7 cm and the cause of the ripple is currently unknown. From the data and theoretical analysis, it's likely that some higher order modes are present in the system at a power level of less than 1%. A more accurate analysis cannot be made at the time. Regardless, an accurate measurement of the loss in a gap has been achieved, validating the accuracy of the SPR technique for measuring losses due to overmoded waveguide components.

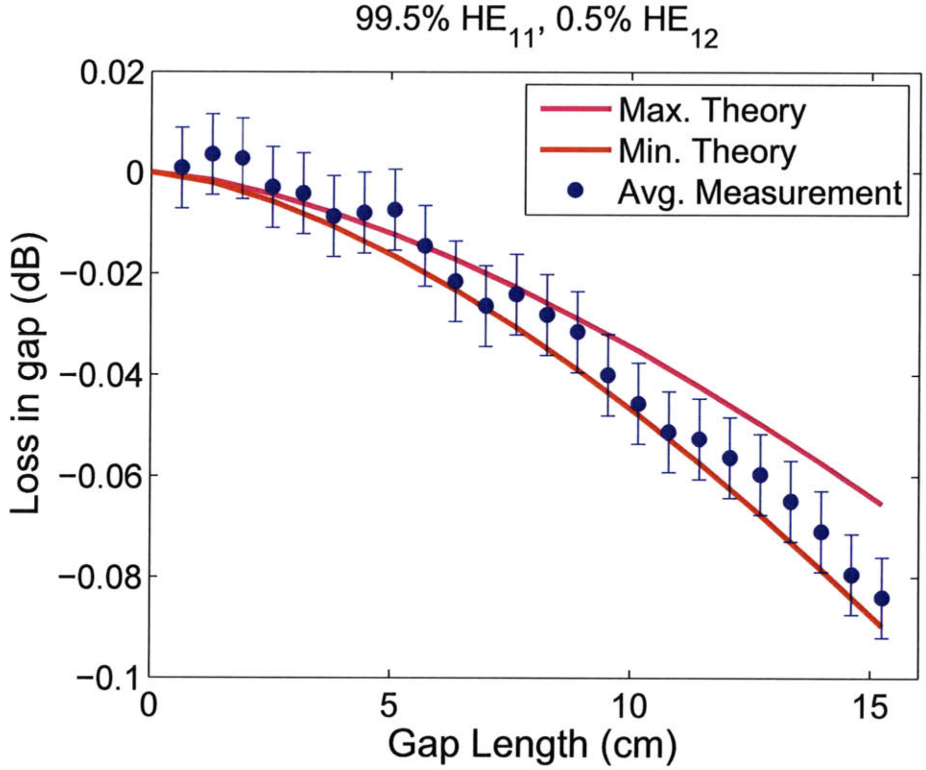

Figure 5-14: The measured loss in a gap versus length of gap (from Figure 5-10) with theoretical curves that consider 0.5% HE_{12} higher order mode content in the system.

Chapter 6

Radiation of a Wave at the End of a Waveguide

In discussion of the theoretical loss in a gap of waveguide (See Chapter 3), the electric field in the gap is analytically calculated through Fresnel diffraction integrals at the end of the gap. However, the form of the electric field as it propagates inside of the gap is not discussed. Consider a system like a gap, but with the receiving waveguide removed, such that the wave is free to radiate from the end of a waveguide. This configuration is useful when considering the launchers at the end of a transmission line system, like the launchers necessary for electron cyclotron resonance heating in ITER.

6.1 Radiation of Single Modes

The electric field for a single mode propagating in a gap was found in Chapter 3 to be

$$\vec{E}^{\perp}_{g,mn}(r,\phi,z) = \hat{y}\frac{j2\pi kA}{z\sqrt{N_{mn}}}e^{jm\frac{\pi}{2}}e^{j\frac{kr^2}{2z}}\cos(m\phi)\int_0^a J_m\left(\frac{X_n r_0}{a}\right)J_m\left(\frac{krr_0}{z}\right)e^{j\frac{kr_0^2}{2z}}r_0 dr_0 \tag{6.1}$$

(reproduced from equation (3.14)), where z is the distance from the end of the waveguide.

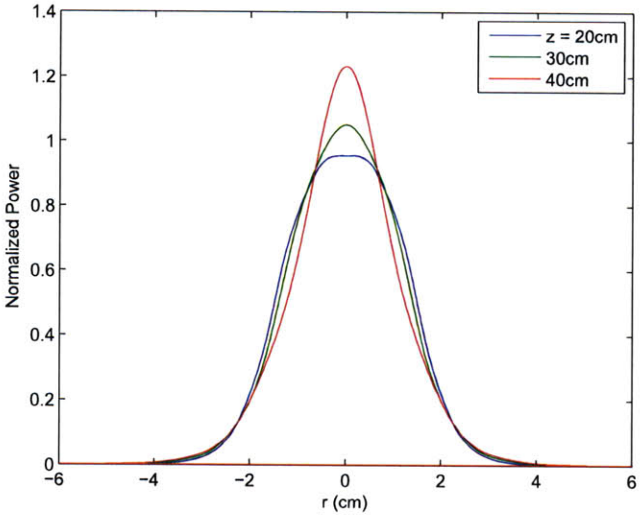

Figure 6-1: The HE_{11} mode for 170 GHz as it propagates outside of a 63.5 mm diameter waveguide. The field is shown at 20, 30, and 40 cm after the end of the waveguide.

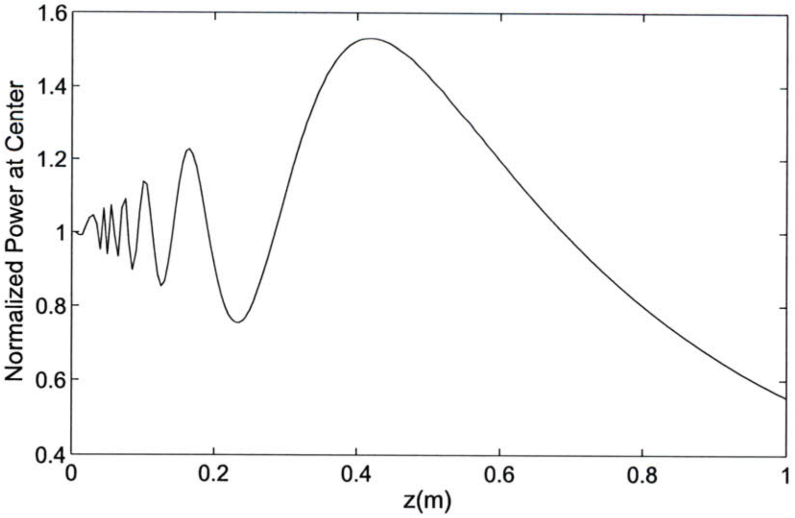

Figure 6-2: The on-axis normalized power of the HE_{11} mode as it propagates outside of a waveguide. A Fresnel Spot is seen in the peaking of the power.

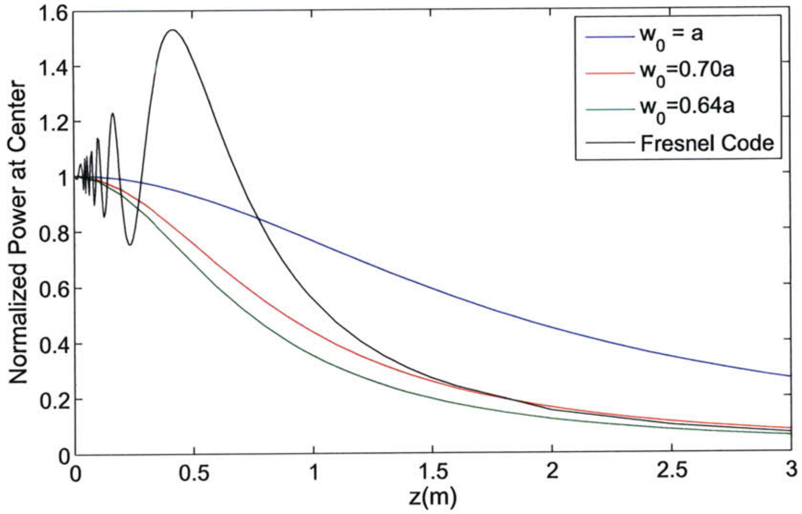

Figure 6-3: The on-axis power of the HE_{11} mode as it propagates outside of a waveguide compared to the propagation of a Gaussian beam with various waist sizes, w_0.

Equation (6.1) can be evaluated anywhere after the waveguide. Figure 6-1 shows the on-axis power for HE_{11} mode (at $r = 0$) as it radiates after the end of the waveguide. Note that a Fresnel spot (a peak in the power) is seen for the HE_{11} mode. That is, the power at the center of the beam increases before decreasing, seemingly against intuition, however the phenomenon is documented to occur for large a/λ ratios [20]. The Fresnel Spot is emphasized when the on-axis ($r = 0$) power is plotted, as seen in Figure 6-2. All HE_{1m} modes will also have the same Fresnel Spot behavior, however the integral could be calculated for any LP_{mn} mode radiating from the end of the waveguide and the same peaking (though not on-axis) will be observed. The radiation pattern is compared to the propagation of a Gaussian beam in Figure 6-3. In this figure, the numerical simulation approaches a Gaussian beam propagation pattern about 1.5 m after the end of the waveguide. The Fresnel diffraction of an HE_{11} mode approaches the distribution of a Gaussian beam with $w_0 \approx .70a$. Previous calculations have found that a Gaussian beam with a $w_0 = 0.64a$ couples from free space into the HE_{11} mode of a waveguide with radius a with minimal losses [29]. The slight discrepancy seen here is due to the numerical limitations of the calculation when considering large values of z.

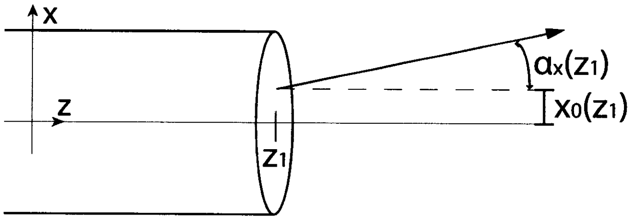

Figure 6-4: A wave radiating from the end of a waveguide at z_1 has a centroid of power with an offset, $x_0(z_1)$, and a tilt angle of propagation, $\alpha_x(z_1)$, as defined here.

6.2 Constant of the Motion for Tilt and Offset

The following section is adapted from Kowalski et al. 2010, in review [21].

Considering the launching of a wave at the end of a transmission line system, it is useful to consider any angle or offset that may occur in the beam as it leaves the waveguide. If a single mode is propagating on the line, the mode will reach the end of the line such that the fields are centered on the waveguide. The radiation pattern at the end of the guide can be calculated in the near and far fields. For a single mode, the direction of propagation will always be centered on and parallel to the waveguide axis. When two or more modes propagate down the transmission line, it is no longer true that the field pattern is, in general, centered on the waveguide axis. The fields will radiate from the end of the waveguide, but the propagation angle will no longer, in general, be parallel to the waveguide axis. In this section, we derive a simple new result for the propagation of two modes that shows a relationship between the tilt and offset at the terminus of a corrugated waveguide transmission line.

The problem is illustrated in Figure 6-4, where the waveguide ends at a particular location of the $\hat{z}$-axis, z_1. When a wave propagates outside of a waveguide, the centroid of power has a particular tilt angle, $\alpha_{x,y}(z)$, and offset, $x_0(z)$ and $y_0(z)$, from the center, as illustrated in Figure 6-4. These two propagation parameters (tilt angle and offset) define the wave after the waveguide and quantify the centroid of power.

The offset and tilt angle of propagation are controlled by the mode content of the wave in the waveguide. A two-mode content is characterized by two parameters, the relative amplitude and phase difference between the modes. For a pure mode leaving a waveguide, the centroid of the mode power is always on axis $(x_0, y_0 = 0)$

and the mode has a constant flat phase front ($\alpha_{x,y} = 0$). However, when two modes propagate, the power centroid will generally be off-center from the axis and the phase front will be tilted by an angle.

A conservation theorem expressing the relationship between tilt and offset for two propagating LP$_{mn}$ modes is derived. For two modes, the electric field is defined as

$$E(x, y, z) = C_1(z)u_{m_1n_1}(x, y) + C_2(z)u_{m_2n_2}(x, y). \tag{6.2}$$

Here, C_p (where $p = 1, 2$ indicates the first or second mode of the system) is a complex variable indicating the amplitude and phase of the modes as

$$C_p(z) = \sqrt{A_p}e^{j(k_{z,p}z_1+\theta_p)}. \tag{6.3}$$

For the p^{th} mode, A_p is the percentage of power in the mode, $k_{z,p}$ is the wavenumber in the $\hat{z}$-direction, and θ_p is the phase of the mode at $z_1 = 0$. Also, $u_{m_pn_p}(x, y)$ is the normalized field pattern of each mode as indicated in equation (2.64), with appropriate substitutions for r and ϕ to convert to the Cartesian coordinate system. The offset and propagation angle in the $\hat{x}$-direction are defined as

$$x_0(z_1) = \langle x(z_1)\rangle = \iint E^*(x, y, z_1)xE(z, y, z_1)dxdy, \tag{6.4}$$

$$\alpha_x(z_1) = \frac{\langle k_x(z_1)\rangle}{k} = \frac{-j}{k}\iint E^*(x, y, z_1)\frac{\partial E(x, y, z_1)}{\partial x}dxdy. \tag{6.5}$$

With the electric field defined for this problem, offset can be expressed as

$$x_0(z_1) = \iint xC_1C_2^*u_{m_1n_1}u_{m_2n_2}^*dxdy + \iint xC_1^*C_2u_{m_1n_1}^*u_{m_2n_2}dxdy, \tag{6.6}$$

and reduced to

$$x_0(z_1) = 2\text{Re}\left(C_1C_2^*\right)b_{12}. \tag{6.7}$$

The propagation angle can also be expressed as

$$\alpha_x(z_1) = \frac{j}{k}\left(\iint C_1 C_2^* u_{m_2 n_2} \frac{\partial u_{m_1 n_1}}{\partial x} dxdy - \iint C_1^* C_2 u_{m_1 n_1} \frac{\partial u_{m_2 n_2}}{\partial x} dxdy\right), \quad (6.8)$$

and reduced to

$$\alpha_x(z_1) = 2\mathrm{Im}\left(C_1 C_2^*\right) d_{12}. \quad (6.9)$$

The variables b_{12} and d_{12} are mode-specific integrals where

$$b_{12} = \iint x u_{m_1 n_1} u_{m_2 n_2} dxdy \quad (6.10)$$

and

$$d_{12} = \frac{-1}{k} \iint u_{m_2 n_2} \frac{\partial u_{m_1 n_1}}{\partial x} dxdy. \quad (6.11)$$

The offset and angle in the $\hat{y}$-direction is similarly found with $x \rightarrow y$ and $y \rightarrow x$. Note that an angle and offset only occur for modes where $m_2 = m_1 \pm 1$; in all other cases, b_{12} and d_{12} evaluate to zero.

Due to the dependence on real and imaginary parts of the complex magnitudes, it is seen that the offset and angle change with the beating, or phase difference, between modes as the fields propagate. It is useful to define the offset and tilt as sinusoidal functions dependent on z_1 by using Euler's identity such that,

$$x_0(z_1) = x_{max} \cos((\Delta k) z_1 + \theta_0) \quad (6.12)$$

$$\alpha_x(z_1) = -\alpha_{max} \sin((\Delta k) z_1 + \theta_0) \quad (6.13)$$

In this case, $(\Delta k) z_1$ indicates the phase difference between the modes and θ_0 is the phase difference at the arbitrary point $z = 0$ between the modes. The maximum possible offset and angle for a combination of two modes are defined as

$$x_{max} = 2b_{12} \left|C_1 C_2^*\right| \quad (6.14)$$

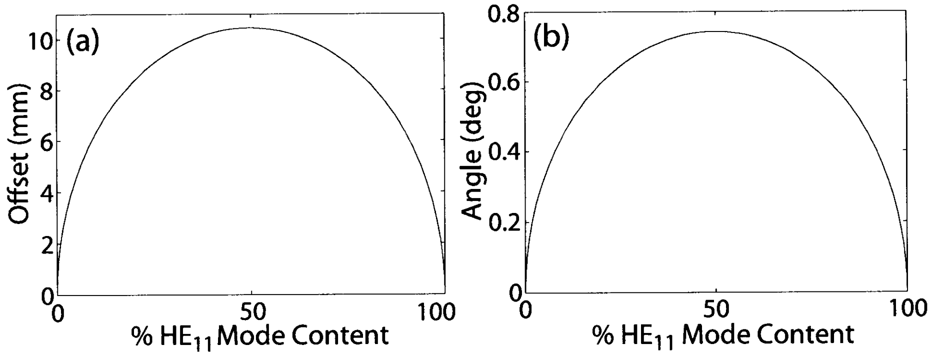

Figure 6-5: Maximum (a) offset and (b) tilt angle vs. HE$_{11}$ percent content (A_p in equation (6.3)) for a combination of HE$_{11}$ and LP$_{11}$ modes.

and

$$\alpha_{max} = 2d_{12}\left|C_1C_2^*\right|. \tag{6.15}$$

In addition, it can be inferred that x_{max} and α_{max} occur when $C_1C_2^*$ is either purely real or purely imaginary, respectively.

Equations (6.12) and (6.13), together with equations (6.14) and (6.15) can be combined to form an expression for tilt and offset that is independent of location (z_1) on the transmission line. That is, the expression for tilt and offset may be combined to form a constant of the motion:

$$\left(\frac{x_0(z_1)}{b_{12}}\right)^2 + \left(\frac{\alpha_x(z_1)}{d_{12}}\right)^2 = 4\left|C_1C_2^*\right|^2. \tag{6.16}$$

The two governing parameters of the system are the percent split and phase difference between the two modes.

To illustrate this constant of the motion, we consider the common two mode combination of HE$_{11}$ and LP$_{11}^{(e)}$ modes. In this case, b_{12} and d_{12} are evaluated as

$$b_{12} = \frac{\sqrt{2}}{a^2 J_1(X_0) J_0(X_1)} \int_0^a J_0\left(\frac{X_0 r}{a}\right) J_1\left(\frac{X_1 r}{a}\right) r^2 dr, \tag{6.17}$$

$$d_{12} = \frac{\lambda X_0 X_1}{\sqrt{2}\pi a\left(X_1^2 - X_0^2\right)}, \tag{6.18}$$

where $X_0 = 2.405$ and $X_1 = 3.832$. This equation reduces to $b_{12} = 0.329a$ and

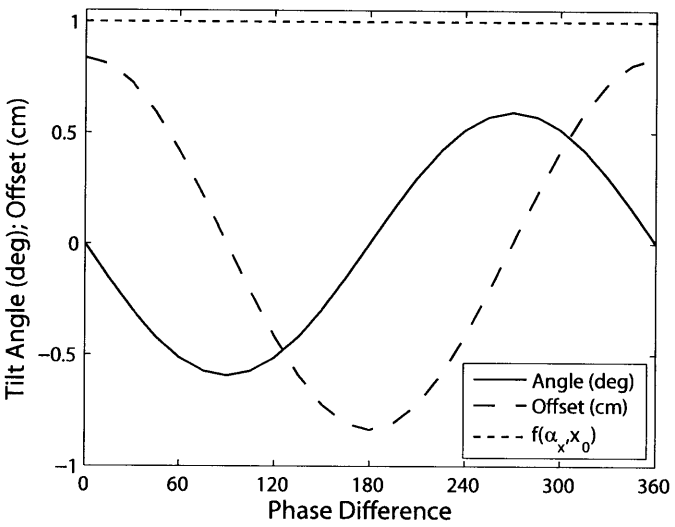

Figure 6-6: The centroid offset and tilt angle for an input of 80% HE_{11} and 20% $\mathrm{LP}_{11}^{(e)}$ in a waveguide of radius $a = 31.75$ mm at 170 GHz. $f(\alpha_x, x_0)$ plots equation (6.19). A 2π phase difference corresponds to $z_1 = 5.07$ m.

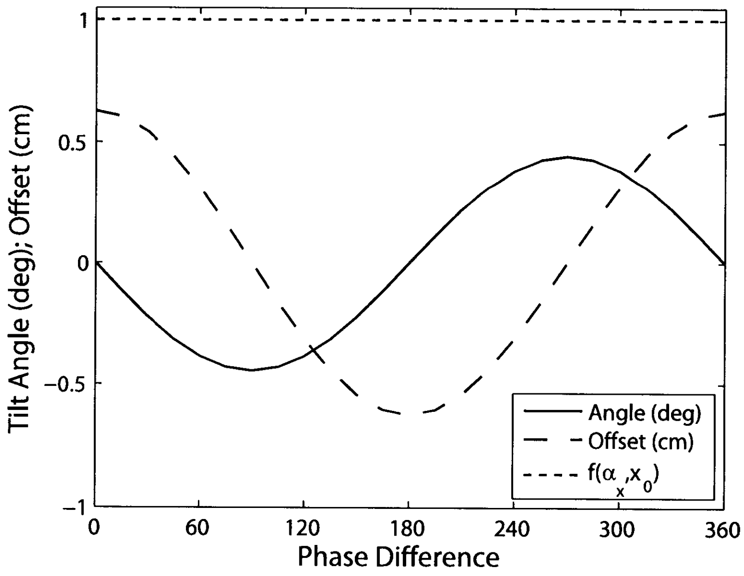

Figure 6-7: The centroid offset and tilt angle for an input of 90% HE_{11} and 10% $\mathrm{LP}_{11}^{(e)}$ in a waveguide of radius $a = 31.75$ mm at 170 GHz. $f(\alpha_x, x_0)$ plots equation (6.19). A 2π phase difference corresponds to $z_1 = 5.07$ m.

$d_{12} = 0.233\lambda/a$. For $a = 31.75$ mm and $\lambda = 1.76$ mm (170 GHz), the parameters evaluate to $d_{12} = 0.74°$ and $b_{12} = 10.45$ mm. Figure 6-5 shows the maximum angle and offset for an input of these two modes as defined in equations (6.14) and (6.15) versus the percent split between the two modes, the only variable parameter which will change the maximum angle and offset. Figures 6-6 and 6-7 show the angle and offset due to an input with 80% HE_{11} and 20% LP_{11} or 90% HE_{11} and 10% LP_{11}, respectively, versus the phase difference between the modes, the second variable parameter. For these two modes, a phase difference of 2π corresponds to $z_1 = 5.07\ m$. Due to interference effects, the power in the two modes propagates in the waveguide with sinusoidal oscillations in both tilt and offset, dependent on phase. By relation to the beat frequency between the two modes, the phase dependence can be quantified as the location in the waveguide where it is terminated and the wave is allowed to radiate into free space, $\theta = (\Delta k)z_1 + \theta_0$. Figure 6-6 has a larger split between the mode contents than Figure 6-7, causing a larger amplitude of offset and angle oscillations. In both figures, the oscillations are out of phase by 90° and combine (using (6.16)) to form a constant of the motion. In both figures we calculate $f(\alpha_x, x_0)$, where

$$f(\alpha_x, x_0) = \frac{1}{4\left|C_1 C_2^*\right|^2}\left[\left(\frac{x_0(z_1)}{b_{12}}\right)^2 + \left(\frac{\alpha_x(z_1)}{d_{12}}\right)^2\right]. \tag{6.19}$$

and show that it is unity for all phases. Other percent splits between HE_{11} and LP_{11} will behave in the same pattern. In addition, other two-mode combinations that result in a centroid offset will behave similarly, i.e. modes that vary by one azimuthal index will follow the same pattern as the HE_{11} and LP_{11} combination illustrated here.

This theoretical evaluation shows that higher order modes in a transmission line system will be a problem for launching electromagnetic waves with high accuracy at the end of the system. Fortunately, the uncertainties in the launching will be a semi-predictable phenomenon due to the constant of the motion discussed in equation (6.16). This conservation theorem limits the maximum phase and offset that known percentage of higher order modes can cause in the launched wave.

Chapter 7

Conclusions

This thesis has presented a complete theory and low-power experimental measurements for the loss in a miter bend and a gap in overmoded corrugated cylindrical waveguide. The experimental measurements agreed well with theory. The low-power experimental SPR technique employed in this thesis is general and has proved to be robust for reliably measuring ultra-low loss in overmoded waveguide components.

7.1 Discussion

The theory presented in this thesis deals with higher order modes in these components and suggests an alternative formulation of the modes in corrugated cylindrical waveguide—linearly polarized, LP_{mn} modes—which form an orthonormal basis set. The LP modes ensure that the polarization of the fields when theoretically considered is consistent with experimental polarization of the electric field when a linearly polarized gyrotron input is used (as is the case with high power microwave experiments).

Using the LP modes formulated in this thesis, the loss due to a gap in waveguide and a miter bend was considered. It was found that the loss for the fundamental mode in these components was dependent on the presence of higher order modes of the same azimuthal symmetry. For these higher order modes, the loss was dependent on the phase difference between the higher order mode and the fundamental mode; on average, the diffraction loss in the fundamental mode in a miter bend was 0.11 dB, or 0.25%. The average loss is independent of higher order mode content. The total theoretical loss in a miter bend was calculated to be 0.027 dB, or 0.61%, taking into account ohmic heating and misalignment errors.

The S-Parameter Response (SPR) technique was used in low-power experiments to measure the loss in two different components. For a miter bend manufactured to ITER specifications, 63.5 mm diameter waveguide with quarter-wavelength corrugations operating at 170 GHz, the loss was measured to be 0.022 ± 0.008 dB. This is in good agreement with theory. In addition, the loss measured due to a gap in waveguide was shown to agree well with theoretical loss in a gap, especially when a small amount (0.5%) of higher order modes are considered in the theoretical calculation. These experimental measurements show that the SPR technique is robust.

7.2 Future Work

The application of this work, the ITER transmission line system, has many components in the system, such as polarizers and switches. It would be useful to measure the loss in these components using the SPR technique, so that a better understanding of the losses in the transmission line system may be determined. In addition, the error associated with the miter bend loss measurement could be reduced by considering different configurations of the experimental set-up and by enhancing our understanding of the higher order mode content on the line via the baseline measurement.

It would also be useful to generate a simple way to employ the SPR technique for on-site measurements. In many high-power, high-frequency experiments, large losses on transmission line components are a significant problem. An easy on-site measurement and trouble-shooting technique would allow for these high losses to be reduced.

Bibliography

[1] A. Cavallo, J. Doane, and R. Cutler. Low-loss broadband multimode corrugated waveguide performance. *Rev. Sci. Instr.*, 81(9):2396–2400, 1990.

[2] P. J. Clarricoats. *Low loss waveguide transmission.* U.S. Patent 3 772 619, Nov. 13, 1973.

[3] P. J. Clarricoats and R. D. Elliot. Multimode corrugated waveguide feed for monopulse radar. *IEEE Proc.*, 128(2):102–110, 1981.

[4] P. J. Clarricoats and A. D. Olver. Low attenuation in corrugated circular waveguides. *Electronics Lett.*, 9(16):376–377, 1973.

[5] P. J. Clarricoats and A. D. Olver. *Corrugated horns for microwave antennas*, volume 18 of *IEEE electromagnetic wave series.* Peter Peregrinus, Ltd., London, UK, 1984.

[6] P. J. Clarricoats, A. D. Olver, and S. L. Chong. Attenuation in corrugated circular waveguides, Part 1: Theory. *Proc. IEEE*, 122(11):1173–1179, 1975.

[7] P. J. Clarricoats, A. D. Olver, and S. L. Chong. Attenuation in corrugated circular waveguides, Part 2: Experiment. *Proc. IEEE*, 122(11):1180–1186, 1975.

[8] P. J. Clarricoats and P. K. Saha. Attenuation in Corrugated Circular Waveguides. *Electronics Lett.*, 6(12):370–372, 1970.

[9] J. P. Crenn and C. Charollais. Propagation and Radiation Characteristics of the Circular Electric, Circular Magnetic, and Hybrid Waveguide Modes. *Int. J. Infrared and Millimeter Waves*, 17(9):1475–1506, 1996.

[10] J. L. Degnan. Waveguide laser mode patterns in the near and far field. *Appl. Optics*, 12(5):1026–1030, 1973.

[11] J. L. Doane. Propagation and Mode Coupling in Corrugated and Smooth-Wall Circular Waveguides. In K. J. Button, editor, *Infrared and Millimeter Waves, Vol. 13, Millimeter Components and Techniques Part IV*, pages 123–170. Academic Press, 1985.

[12] J. L. Doane. Design of circular corrugated waveguides to transmit millimeter waves at ITER. *Fusion Sci. Technol.*, 53(159), 2008.

[13] J. L. Doane and C. P. Moeller. HE_{11} mitre bends and gaps in a circular corrugated waveguide. *Int. J. Electronics*, 77:489–509, 1994.

[14] J. L. Doane and R. A. Olstad. Transmission line technology for electron cyclotron heating. *Fusion Sci. Technol.*, 53(39), 2008.

[15] C. Dragone. Attenuation and radiation characteristics of the HE_{11}-mode. *IEEE Trans. Microwave Theory and Techniques*, 28(7):704–710, 1980.

[16] A. G. Fox and T. Li. Resonant Modes in a Maser Interferometer. *Bell System Tech. J.*, 40(2):453–488, 1961.

[17] S. Han, E. Comfoltey, M. Shapiro, J Sirigiri, D. Tax, R. Temkin, P. Wosksov, and D. Rasmussen. Low power testing of losses in components for the ITER ECH transmission lines. *32nd Int. Conf. on IR MMW and Thz Elec.*, 1:915–917, 2007.

[18] S. Han, E. Comfoltey, M. Shapiro, J Sirigiri, D. Tax, R. Temkin, P. Wosksov, and D. Rasmussen. Low-Power Testing of Losses in Millimter-Wave Transmission Lines for High-Power Applications. *Intl. J. Infrared and Millimeter Waves*, 29(11):1011–1018, 2008.

[19] H. A. Haus. *Waves and fields in optoelectronics.* CBLS, Marietta, OH, 2004.

[20] J. A. Kong. *Electromagnetic Wave Theory.* EMW Publishing, Cambridge, MA, 2008.

[21] E. Kowalski, D. Tax, M. Shapiro, J. Sirigiri, R. Temkin, T. Bigelow, and D. Rasmussen. Linearly Polarized Modes in a Corrugated Metallic Waveguide. *IEEE Trans. Microwave Theory and Techniques*, Submitted Apr. 2010. In Review.

[22] E. Marcatili. Hollow metallic and dielectric waveguides for long distance optical transmission and lasers. *Bell System Tech. J.*, 43:1783–1809, 1964.

[23] E. Marcatili. Miter elbow for circular electric modes. In *Proc. Symp. on Quasi-Optics*, pages 535–542, Brooklyn, NY, June 8–10, 1964. Polytech Press.

[24] S. E. Miller. Waveguide as a Communication Medium. *Bell System Tech. J.*, 33(6):1209–1267, 1954.

[25] K. Ohkubo, S. Kubo, H. Idei, M. Sato, T. Shimozuma, and Y. Takita. Coupling of tilting Gaussian beam with hybrid mode in the corrugated waveguide. *Int. J. Infrared and Millimeter Waves*, 18(1):23–41, 1997.

[26] K. Ohkubo, S. Kubo, M. Iswase, H. Idei, M. Sato, T. Shimozuma, Y. Takita, and T. Kuroda. Hybrid Mode Transmission in 62-m Corrugated Waveguide. *Int. J. Infrared and Millimeter Waves*, 15(9):1507–1519, 1994.

[27] K. Okamoto. *Fundamentals of Optical Waveguides.* Academic Press, Burlington, MA, 2nd edition, 2006.

[28] A. D. Olver, P. J. Clarricoats, and S. L. Chong. Experimental determination of attenuation in corrugated circular waveguides. *Electronics Lett.*, 9(18):424–426, 1973.

[29] M. Perkins and R. Vernon. Coupling of a Gaussian beam from a gyrotron into a corrugated cicular waveguide for plasma heating. *IEEE Antennas and Propagation Soc. Intl. Symp.*, 4:2024–2027, 2000.

[30] D. Pozar. *Microwave Engineering.* John Wiley and Sons, Inc., Hoboken, NJ, 3 edition, 2005.

[31] M. A. Shapiro, E. J. Kowalski, J. R. Sirigiri, D. S. Tax, R. J. Temkin, T. S. Bigelow, J. B. Caughman, and D. A. Rasmussen. Loss estimate for ITER ECH transmission line including multimode propagation. *Fusion Sci. Technol.*, 57, Apr. 2010.

[32] D. I. Sobolev, A. V. Chirkov, G. G. Denisov, D. A. Lukovnikov, and V. I. Malygin. Minimization of diffraction losses in big gaps of multi-mode waveguides. *Int. J. Infrared and Millimeter Waves*, 26(7):953–966, 2005.

[33] D. S. Tax, E. N. Comfoltey, S. T. Han, M. A. Shapiro, J. R. Sirigiri, R.J. Temkin, and P. P. Woskov. Mode conversion losses in ITER transmission lines. *Proc. of 33rd Int. Conf. IR, MM, and THz Waves*, Sept. 2008.

[34] M. K. Thumm and W. Kasparek. Passive high-power microwave components. *IEEE Trans. Plasma Sci.*, 30(3):755–786, June 2002.

[35] D. Wagner, M. Thumm, K. Kasparek, G. A. Muller, and O Braz. Prediction of TE-, TM-, and hybrid-mode transmission losses in gaps of oversized waveguides using a scattering matrix code. *Int. J. Infrared and Millimeter Waves*, 17(6):1071–1081, 1996.

[36] L. A. Weinstein. *The Theory of Diffraction and the Factorization method (generalized Weiner-Hopf technique)*, volume 3 of *Golem series in electromagnetics.* Golem Press, Boulder, CO, 1969.

[37] A. Yariv. *Optical Electronics.* Saunders College Pub., Philadelphia, PA, 1991.